Surveillance Video Analysis with External Knowledge and Internal Constraints

Shoou-I Yu

CMU-LTI-16-009

Language Technologies Institute
School of Computer Science
Carnegie Mellon University
5000 Forbes Ave., Pittsburgh, PA, 15213
www.lti.cs.cmu.edu

Thesis Committee:

Dr. Alexander G. Hauptmann, Carnegie Mellon University
Dr. Abhinav Gupta, Carnegie Mellon University
Dr. Yaser Sheikh, Carnegie Mellon University
Dr. Rahul Sukthankar, Google Research

Submitted in partial fulfillment of the requirements
for the degree of Doctor of Philosophy
In Language and Information Technologies

Abstract

The automated analysis of video data becomes ever more important as we are inundated with the ocean of videos generated every day, thus leading to much research in tasks such as content-based video retrieval, pose estimation and surveillance video analysis. Current state-of-the-art algorithms in these tasks are mainly supervised, i.e. the algorithms learn models based on manually labeled training data. However, it is difficult to manually collect large quantities of high quality labeled data. Therefore, in this thesis, we propose to circumvent this problem by automatically harvesting and exploiting useful information from unlabeled video based on 1) out-of-domain external knowledge sources and 2) internal constraints in video. Two tasks in the surveillance domain were targeted: multi-object tracking and pose estimation.

Being able to localize and identify each individual at each time instant would be extremely useful in surveillance video analysis. We tackled this challenge by formulating the problem as an identity-aware multi-object tracking problem. An existing out-of-domain knowledge source: face recognition, and an internal constraint: the spatial-temporal smoothness constraint were used in a joint optimization framework to localize each person. The spatial-temporal smoothness constraint was further utilized to automatically collect large amounts of multi-view person re-identification training data. This data was utilized to train deep person re-identification networks which further enhanced tracking performance on our 23-day 15-camera data set which consists of 4,935 hours of video. Results show that our tracker has the ability to locate a person 57% of the time with 73% precision.

Reliable pose estimation in video enables us to understand the actions of a person, which would be very useful in surveillance video analysis. However, domain differences between surveillance videos and the pose detector's training set often cause degradation in pose estimation performance. Therefore, an unsupervised domain adaptation method based on constrained self-training was proposed. By utilizing an out-of-domain image-based pose detector (external knowledge) and spatial-temporal smoothness constraints (internal constraints), our method can automatically collect in-domain pose estimation training data from video for domain adaptation. Results show that the pose detector trained on in-domain data collected with our unsupervised approach is significantly more effective than models trained on more out-of-domain data.

Finally, based on our improved multi-object tracker and pose detector, long-term analyses of nursing home resident behavior were performed. Results show that the output of our tracker was accurate enough to generate for each nursing home resident a reasonable "visual diary", which not only shows the activities performed throughout the

day, but also accumulated long-term statistics which are simply too tedious to compute manually. Furthermore, pose detectors were utilized to detect eating behavior of nursing home residents, which would also have the potential to aid the assessment of health status of nursing home residents.

In conclusion, our results demonstrate the effectiveness of utilizing external knowledge and internal constraints to enhance multi-object tracking and pose estimation. The methods proposed all attempt to automatically harvest useful information directly from unlabeled videos. Based on the promising experimental results, we believe that the lessons learned could be generalized to other video analysis problems, which could also benefit from utilizing external knowledge or internal constraints in an unsupervised manner, thus reducing the need to manually label data. Furthermore, our proposed methods potentially open the door to automated analysis on the ocean of surveillance video generated every day.

Acknowledgements [1]

Alex Hauptmann, for also being a Harry Potter fan and giving me, a muggle, the courage and freedom to work on my passion and create a real-world Marauder's Map, which ultimately turned out to be the highlight of my thesis.

My committee: Abhinav Gupta, Yaser Sheikh and Rahul Sukthankar for pinpointing weaknesses in my work and providing very helpful suggestions.

Yi Yang, for teaching me how to write research papers.

Deyu Meng, for the fruitful discussions on the solution path algorithm.

My TRECVID MED and ALADDIN comrades: Xiaojun Chang, Lu Jiang, Zhen-Zhong Lan, Xuanchong Li, Shicheng Xu, Zhongwen Xu and many many others for the blood and tears shed to ensure our project a success.

My current office mates: Xinlei Chen, Prasanna Kumar and Chenyan Xiong for providing real-time free-food updates.

My "eating" mates: Kenneth Ting-Hao Huang, Chih-Yi Lin, Shih-Yun Lo, Vivian Yun-Nung Chen, Yi Luan and Zuxuan Wu for heated discussions over what to eat for dinner.

My volleyball and softball mates, for balancing my crazy graduate school life.

Wan-Yu Lin, for the countless Skype "meetings".

My family, Chi-Zen Yu, Bih-Yueh Hwang and Shoou-Jong Yu for always welcoming me home, be it Mountain View, Tokyo or Taipei.

[1] This work was partially supported by the U.S. Army Research Office (W911NF-13-1-0277) and partially supported by the National Science Foundation under Grant Number IIS-1251187. Any opinions, findings, and conclusions or recommendations expressed in this material are those of the author(s) and do not necessarily reflect the views of the ARO and NSF. We gratefully acknowledge the support of NVIDIA Corporation with the donation of the Titan X GPU used for this research.

Contents

Chapter 1

Introduction

Automatic understanding of video content has a wide variety of applications including, video retrieval [1], surveillance [2] and health care [3]. Furthermore, automated analysis becomes ever more important as we are inundated by the ocean of user-generated and surveillance videos created every day. Therefore, much research has focused on designing effective algorithms to analyze the content of videos.

In general, supervised methods have achieved promising results in image and video analysis tasks [4–8]. Supervised methods heavily rely on labeled training data to create models which can better generalize to unseen data. To achieve effective generalization, the training data set needs to 1) be large enough in quantity and 2) match the distribution of the testing data. Large enough training data is the key to the success of many algorithms [9], such as the success of deep neural networks in object recognition [5], and according to statistical machine learning theory [10], more data can decrease the difference between testing error and training error. Also, it is required that the training data has the same distribution as the testing data. If the distributions do not match, performance will significantly degrade [11]. The two aforementioned points motivate us to collect more training data from diverse sources such that the training distribution can better approximate the true testing distribution.

Training data can be collected and labeled manually, which is how many existing image and video data sets were collected [12–14]. However, manual labeling is a difficult and very labor intensive process. To alleviate the tediousness of labeling, some researchers have created data sets such as ImageNet [12] with crowdsourcing based on Amazon Mechanical Turk. Much research has also gone into how to maximize the utility of crowdsourcing [15, 16]. Another direction of data collection is through "gamification" [17, 18], where the data annotation task is transformed into a game so that as humans play the game, more annotations are collected. Though these methods have shown to

be effective, crowdsourcing requires actual money, and gamification requires designing an interesting game, which is challenging. Also, the manual annotation process needs to be repeated whenever one acquires data from a new domain. Furthermore, for privacy sensitive data, it may not be convenient for the public to annotate the data. Finally, data evolve over time, thus forming new labels of interest. So what was labeled in the past may no longer be of interest now, and to stay up-to-date, the labeling process needs to be run continuously. Therefore, based on the aforementioned shortcomings, one interesting question becomes whether one could alleviate the process of data annotation by trying to directly collect useful information from unlabeled data.

In this thesis, we are interested in exploring the idea of automatically extracting useful information directly from unlabeled data to enhance the task at hand. We believe that the key to unlocking the useful information hidden in the large amounts of unlabeled data available is to rely on two main sources of information: 1) existing out-of-domain knowledge sources and 2) internal constraints in video.

Exploiting External Knowledge

Instead of collecting manual annotations for each specific task, one can try utilizing the already existing highly related external resources to tackle the task. For example, if one would like to train a person detector for a specific traffic scene, instead of directly annotating people in the scene, one can start with an external generic object detector and adapt it to the scene with the aid of some internal constraints [19, 20]. Another example is tackling the semantic segmentation task with existing external but related knowledge. Collecting semantic segmentation training data is very expensive because it requires delineating the boundaries of each object. Therefore, [21, 22] utilized existing cheap image/video-level labels and other constraints to learn a classifier to perform semantic segmentation. [23] utilized detection proposals from an external object detector as a starting point for their semantic segmentation algorithm. In sum, there are already many existing resources available to aid us in tackling a new task on a new data set, thus potentially alleviating the need for manual labeling.

Utilizing Internal Constraints

Internal constraints refer to specific patterns which the data set of interest follows in most cases. For example, objects in a video should move smoothly is an internal constraint heavily used in tracking. A very exciting scenario to exploit internal constraints is the automatic collection of training data from unlabeled data. Many automated systems have been proposed to acquire knowledge from the vast amount of unstructured and

unlabeled information readily available on the Internet. These systems heavily rely on internal constraints of the data to harvest useful information. For text, the Never Ending Language Learner (NELL) [24] automatically learned facts of different entities from unstructured web documents. An example constraint which was used in web documents is: entities enclosed in the same HTML list structure are highly likely to be entities of similar types [25]. In images, the Never Ending Image Learner (NEIL) [26] learned facts of different entities from unlabeled images. Constraints utilized were common sense relationships between categories such as "wheel has round shape" or "pyramid is found in Egypt". Learn EVerthing about ANything (LEVAN) [27] is another image based system which utilized image search engines and text language models to automatically learn object detectors. Other work has proposed to utilize unlabeled video data to enhance image analysis tasks. [28] utilized unlabeled videos to collect training examples to learn improved static image action detectors. [29–31] improved object detection by harvesting positive examples from unlabeled videos in an unsupervised fashion. Overall, the aforementioned systems share two core concepts:

- They can operate on unlabeled data in a (nearly)[1] automatic way.
- They utilized assumptions or constraints to enable them to extract useful information from unlabeled data.

These two points combined together enabled these methods to exploit very large amounts of unlabeled data readily available on the Internet. A very attractive property of these systems is that even if the assumptions or constraints utilized are very strict, i.e. a high precision low recall scenario, the system is still able to collect a lot of useful information because there is a near infinite amount of unlabeled data. Colloquially speaking, even if 99.99% of the data was thrown away, the remaining 0.01% will still give us very large amounts of useful information if the system had access to a very big collection of unlabeled data. This spirit is what makes these methods very attractive and useful. The key advantages of these systems are three-fold:

1. Unsupervised methods which can exploit very large amounts of unlabeled data have the potential to collect large amounts of useful information such as training data.
2. Training data can be directly extracted from unlabeled test sets, thus decreasing domain difference between training and testing sets.
3. Training data can be automatically updated as the unlabeled data evolve over time.

[1] These systems may face the problem of semantic drift, and in the case of NELL, humans manually clean the database periodically.

Motivated by the success of previous systems which utilized external knowledge or internal constraints, we explored applying these principles to surveillance video analysis, specifically on multi-object tracking and pose estimation.

Thesis Overview

In this thesis, we tackled two surveillance video analysis tasks: multi-object tracking and pose estimation, with two information sources: external knowledge and internal constraints, in an unsupervised manner. In this thesis, the term "unsupervised" is interpreted in a slightly relaxed manner. Our proposed methods are unsupervised in that *no video-level annotations are required*. Our methods still utilize pre-existing out-of-domain static image resources, which are viewed as external knowledge.

It would be very useful in surveillance video analysis if one was able to locate and identify each person at each time instant. We tackled this challenge by formulating the problem as an identity-aware multi-object tracking task. Our multi-object tracker was augmented with an external resource: face recognition, which provides identity information to person detections with a recognizable face. This can be viewed as label information directly extracted from unlabeled surveillance video. However, most person detections do not have a visible or recognizable face. Therefore, face recognition is only sparse label information and additional cues including appearance features and motion constraints were utilized to perform multi-person tracking. The motion constraints correspond to an internal constraint in video: spatial-temporal smoothness, which assumes that a person should move smoothly in the video and cannot be at two places at the same time. The tracking problem was formulated as a constrained quadratic optimization problem, which we solved by two proposed algorithms: nonnegative matrix optimization and the solution path algorithm. The final tracking output will provide access to the location of each individual at each time instant. Multi-person tracking experiments were run on up to 4,935 hours of surveillance video data, which is to the best of our knowledge the biggest multi-object tracking experiment to date. More details are in Chapter 3.

Another direction to enhance multi-object tracking is by replacing handcrafted appearance features with discriminatively learned deep features which can be used for person re-identification. Person re-identification is the task of distinguishing whether two person detections belong to the same individual or not. However, learning such deep features requires a lot of labeled training data. Therefore, to collect data, we also utilized the spatial-temporal smoothness constraint. In multi-camera surveillance scenarios, if two cameras both independently detect there is a person at a specific location, then it is highly likely that they are viewing the same individual from two different views.

The same individual viewed from two different angles is exactly the training data used for person re-identification. Thus, a standard person re-identification network can be trained to learn a discriminative representation for appearance. Experiments show that the deep representation learned further improved tracking performance. More details are in Chapter 4.

Reliable pose estimation enables us to understand the actions of a person, which would be very useful in surveillance video analysis. One issue is that the domain of the pose detector's training data, which is often static images, does not match the surveillance video domain, thus motivating us to perform unsupervised domain adaptation. We propose to utilize constrained self-training to directly collect in-domain samples from the testing set. Self-training [32, 33] is the process of adding testing instances which have high confidence predictions into the training set to enhance the current model. However, instances with high confidence predictions may not always be correct. Therefore, the main idea is to utilize the spatial-temporal smoothness constraints to perform checks on whether a pose estimation result on the testing set is correct. The assumption is that pose estimation results in neighboring frames should vary smoothly. If a drastic change is observed, then at least one of the pose estimation results is incorrect. Based on this assumption, pose estimations instances which not only have high prediction scores but also pass the smoothness check are even more likely to be correct. These instances from the testing set are eligible to be added to the training set to automatically adapt the pose estimation model to the testing set. Results show that the pose detector trained on in-domain data collected with our unsupervised approach was significantly more effective than models trained on more out-of-domain data. More details are in Chapter 5.

Based on the multi-object tracker and pose detector developed, we performed long-term surveillance video analysis on nursing home surveillance data. Based on the output of multi-object tracking, our system was able to detect events-of-interest such as room changes, sit down and stand up (with an aid of a sitting detector), and human-human interactions. With tracking of each person over 23 days, long-term statistics such as the distance walked per day and total time spent in interactions were accumulated. With our pose detector, a "take a bite" detector was created. This detector could facilitate the analysis of eating behavior of nursing home residents. More details are in Chapter 6.

In summary, the thesis statement is as follows.

Thesis Statement:

Through utilizing 1) existing out-of-domain knowledge sources and 2) internal constraints in video, we can design algorithms which enhance the performance of surveillance video analysis tasks in an unsupervised fashion.

Thesis Contributions

In this thesis, we present our proposed approaches for unsupervised surveillance video analysis in multi-person tracking and pose estimation.

1. Multi-person tracking with face recognition: we designed a method which utilizes an external knowledge source: face recognition to not only identify each person in the scene, but also enhance tracking performance. The tracking problem was solved with two different optimization techniques (CVPR '13 [2], CVPR '16 [34]).
2. Unsupervised collection of person re-identification training data for tracking: we present an unsupervised method based on the spatial-temporal smoothness constraint to collect person re-identification training data, which enabled us to learn deep appearance features to further enhance multi-person tracking.
3. Unsupervised domain adaptation for pose estimation with constrained self-training: we propose to automatically develop effective video pose detectors by adapting existing image pose detectors to video in a constrained self-training framework (ECCV '14 [35]). Spatial-temporal constraints were utilized for effective self-training. Experiments were performed on a newly annotated Caremedia nursing home pose data set with 3.2K poses.
4. Long-term surveillance video analysis: we utilized our multi-object tracker and pose detector to analyze 23 days of nursing home surveillance data. Experiments on surveillance video summarization, eating detection, and long-term statistics analysis were performed.

The thesis is organized as follows. Chapter 2 surveys related work which has a similar unsupervised spirit as our proposed approaches. Chapter 3 presents work on multi-person tracking with face recognition. Chapter 4 details how we collected person re-identification training data from multi-camera surveillance environments. Chapter 5 reports work on unsupervised adaptation of image-based pose estimators to video. Chapter 6 presents long-term surveillance video analysis based on our multi-object tracker and pose detector. Finally, Chapter 7 concludes the thesis.

Chapter 2

Related Work - From Weak Supervision to No Supervision

This thesis focuses on analyzing surveillance video by utilizing external knowledge and internal constraints, which have also been widely used in other domains. In this chapter, we present an overview of existing computer vision work which has a similar spirit as this thesis. The existing work is categorized into methods which used either weak supervision or no supervision.

Weakly supervised learning, in contrast to fully supervised learning, means that the learner is somehow handicapped in terms of the training data. There are many different ways to be handicapped in terms of training data, thus the terms "weakly supervised", "weak supervision" or "distance supervision" have been interpreted in various ways in the literature. Possible interpretations are as follows:

1. Training data is scarce [36, 37].
2. Training data is noisy [38, 39].
3. Training data is only provided for another related task, which usually have labels with less granularity than the task of interest [40–43].

Overall, in-domain training data is still provided, but the labeled data is not as comprehensive and perfect as the labeled data used during full supervision.

Taking weak supervision one step further are methods that require no supervision. For these methods, in-domain training data is not provided at all. Note that this does not necessarily mean that the method did not use any manually labeled training data. A pre-trained model trained on existing out-of-domain instances can still be used. A popular example of this class is unsupervised object detector adaptation [29, 30, 44, 45]. Given an object detector trained on labeled training data in the source domain, the goal

is to automatically adapt the detector to the target domain. As the adaptation process requires no human intervention, these methods require no supervision.

In order to deal with the lack of complete labeled data, methods utilizing either weak supervision or no supervision often require additional assumptions or constraints. The assumptions or constraints include real-world physical constraints (i.e. an object cannot move too quickly in video), assumptions on the structure of the image/video (i.e. the size of objects), or assumptions on classifier confidence being correlated with accuracy. These assumptions play a very important role in methods which are weakly supervised or unsupervised, and often the main novelty of a paper is the formulation and exploitation of these assumptions. In the following sections, we will review existing computer vision work which utilized weak supervision or no supervision.

2.1 From Object Recognition to Object Detection or Semantic Segmentation with Weak Supervision

There can be 3 different granularities of object labels when labeling an image/video. An object label can be on an image/video-level, which indicates the existence of the label but not the spatial locations. These labels are suitable for the object recognition task, which only tries to recognize what objects are visible. A more fine-grained labeling is by adding a bounding box which indicates the location of the object. These labels are suitable for the object detection task, which further tries to localize each object. The most fine-grained labeling is by further delineating the pixel-level boundaries of the object. This is suitable for the semantic segmentation task, which requires not only localizing the object but also finding the boundaries of each object. Clearly, having the boundaries of the object provides the richest information, but it is also the most time consuming to annotate. Therefore, an interesting question becomes whether it is possible to use less fine-grained but cheaper labels and output results with higher granularity, i.e. utilize object recognition labels to learn a model which outputs a semantic segmentation. The main intuition and assumption behind why this may work are that an object recognition system which works well implies that the system has some idea of the location of the object. This task is weakly supervised because though labels are provided for in-domain data, the labels utilized are from a related task which has labels with less granularity than the target task.

In the following few paragraphs, we will briefly describe the related work in this direction. For clarity, related work is categorized into methods which operate on either static images or video. They are discussed separately as video has an extra temporal aspect and

different methods were used. Also, methods which have different output granularities are also separated.

Image-level labels to bounding boxes: The main goal is to utilize image-level labels and localize the objects in the image. One popular method is to treat the bounding box of the object as a hidden variable, which can then be found with variants of SVMs [43, 46], probabilistic latent semantic analysis [47], or deep learning [48]. A more thorough survey is presented in [49].

Image-level labels or bounding boxes to segmentation: Previous work has proposed to utilize image-level labels [21, 50, 51] or object bounding boxes [52] combined with constraints such as the size of the foreground and background [53] to perform semantic segmentation. Common learning methods utilized include Multiple Instance Learning [21] combined with multi-task learning [50] or deep learning [51]. Other methods took this one step further by jointly learning over weak image-level labels and strong pixel-level labels in a semi-supervised framework [54, 55].

Video-level labels to bounding boxes: According to [56], there is a clear domain difference between videos and images, which causes degradation in object detection performance when an object detector trained on still images are predicted on video frames. Therefore, [57] proposed to automatically find bounding boxes of objects in videos based on video-level labels. Assuming that the video only contains objects of a target class, the algorithm first computed spatio-temporal tubes based on motion segmentation for each video. Then a joint one-tube-per-video selection was performed to find the most coherent set of tubes across all videos. These tubes were then used to train an object detector.

Video-level labels to segmentation: Another popular topic is to perform spatio-temporal segmentation of objects in video with either very few frame-level labels [58] or video-level labels [22, 59]. [23] on the other hand utilized a generic object detector as weak supervision. Regardless of the source of supervision, all these methods utilize some sort of motion consistency, spatial-temporal smoothness or tracking constraint to guide their learning process to find the relevant semantic segments in the video.

Some methods took weakly-supervised object detection one step further by utilizing no training data at all and relying only on large amounts of unlabeled data. The intuition is that if enough data is provided, then commonly appearing objects can still be grouped together and "discovered". There are two tasks under this definition: co-localization and object discovery. For image and video co-localization, the input is a set of unlabeled images or video, and the output is bounding boxes which localize objects of the same class. It is unknown to the algorithm which object is in the data, but it is assumed that the

object of interest is visible in most of the unlabeled images/video. [60] proposed to solve image co-localization by jointly utilizing an image similarity/discriminability model and a bounding box similarity/discriminability model in a constrained quadratic optimization framework. [61] further extended this to video by adding the temporal consistency constraint. Object discovery takes co-localization one step further by operating on large amounts of videos which include different classes of objects. [62] utilized inter-video matching and intra-video tracking to find spatio-temporal tubes which localize different objects.

2.2 Noisy Internet-Retrieved Labels as Weak Supervision

Another weakly supervised learning approach to learn object detectors or even segmentation masks of each object is through utilizing noisy training data crawled from search engines or photo-sharing sites, thus less or even no manual annotation is required. [26, 27, 38, 63, 64] can utilize noisy training data crawled from Flickr or top results of an image search engine to learn multiple object classifiers. [39, 65, 66] takes this one step further by performing simultaneous object discovery and segmentation. In the advent of deep learning, [67] demonstrated how to train a CNN-based object detector on search engine results. [67] first trained an initial CNN on the easy images downloaded from Google image search. Then, the network was fine-tuned on the more realistic images from Flickr plus some modifications based on the confusion matrix of the initial CNN.

Similar work has also been done on training video-level event detectors and semantic concept detectors. [68] augmented manually labeled event video with top-ranked videos from YouTube search to enhance event recognition. [69] utilized video metadata from YouTube to collect 1 million sports related videos which belong to 487 classes. [70] utilized tags provided in the YFCC data set [71], which includes 0.8 million weakly-annotated videos from Flickr to train semantic concept detectors. These detectors have shown to be very effective in low-resource event detection [1, 7].

2.3 Domain Adaptation with No Supervision

The goal of domain adaptation with no supervision, which is more commonly known as unsupervised domain adaptation, is to adapt a model trained on the source domain to an unlabeled target domain without any supervision. There are many high-level directions to perform unsupervised domain adaptation. One direction is to somehow "connect" or "re-align" the source and target domains in an unsupervised fashion. Another direction

tries to collect training samples from the testing set and perform self-training. In this section, we will detail existing work in these two directions, especially with a focus on self-training because it is also utilized in this thesis. For a more comprehensive survey on domain adaptation, we refer the readers to the following survey papers, which survey unsupervised domain adaptation for person detection [72], visual domains in general [73] and natural language processing [33].

Given the source and target distributions, one can design algorithms to try to align or minimize the difference between the two domains. [74] modeled sampling bias between the source and target domain with covariate shift. [75, 76] found subspaces in the geodesic path which connected the source and target domains on a Grassmannian manifold. [77] found latent domains which have the maximum distinctiveness and learnability. [78] directly learned max-margin non-orthogonal hyperplanes in the target domain. [79] tried to find a single deep feature representation for both the source and target domain. The deep feature representation was designed so that it is difficult to distinguish from the representation alone whether the current instance came from the source or target domain. [80] learned a transformation such that the source domain samples can be reconstructed by nearest neighbor samples found in the target domain. Unlike self-training, none of these methods tried to collect "training data" from the testing set.

A large portion of unsupervised domain adaptation approaches fall into the self-training (i.e. bootstrapping) paradigm. The first step of self-training is to perform prediction on the testing set to acquire pseudo-labels for the testing instances. Then, self-training assumes that high confidence pseudo-labels in the testing data are highly likely to be correct, and one could add these labels back in the training set and reap additional gains [81, 82]. However, high confidence pseudo-labels may not necessarily be correct, thus "checks" which are *independent* of the classifier itself are utilized to ensure that the pseudo-labels of the instances added are even more likely to be correct. Taking [32] as an example, the main idea is to collect potential training data for eye detection from unlabeled images based on different selection metrics. A classifier confidence based metric and a classifier independent metric were proposed. The classifier confidence based metric selected testing instances with high confidence pseudo-labels. The classifier independent metric computed a classifier independent distance between the testing instances and all the current training data. Testing instances with smaller distance than other training data were selected. Experiments showed that the classifier independent metric was more reliable than the classifier confidence metric, which demonstrates the importance of independent checks.

A myriad of self-training approaches has been proposed to tackle unsupervised domain adaptation in multiple vision tasks, especially in the task of adapting object detectors

to video. As this is highly related to our constrained self-training for pose estimation, we will describe this in more detail in the following sections.

Self-training for Adapting Object Detectors to Video

Object detectors have achieved impressive results on static images [4], but due to domain differences between images and video [56], the object detectors only trained on static images may not work well on video. Therefore, much work has proposed to utilize self-training to adapt an image-based object detector to video. [83] utilized an Adaboost [84] framework combined with Co-training [85] to progressively improve object detectors. As the base classifiers learned from Adaboost are uncorrelated by design, they can be used as independent checks for the output of other base classifiers. [86] proposed that a detected body part is only confident when all other parts also have confident detections. This criterion was used when adding new training data to enhance a part-based person detector. [87] utilized objects detected with high confidence combined with Multiple Kernel Learning to adapt detectors to different lighting condition in video. [88] proposed to utilize dense patch sampling and sparse binary vector encoding to more accurately identify low-confidence but correct person detections. [89] improved an object detector by utilizing superpixels instead of the common Haar-like features. To create an object detector for video, a bag-of-superpixel-based SVM was trained, and instances with confidence in the top one-third were added into the positive set. Instances in the bottom one-third were added into the negative set, and the SVM was retrained and this process repeated.

Adaptation with the Tracking or Spatial-Temporal Smoothness Check

A crucial independent check in video is the tracking or spatial-temporal smoothness check, i.e. an object should not move too far in adjacent frames, which is conveniently available in nearly all unedited videos. This check or variants of it have been heavily utilized in unsupervised adaptation of object detectors to video.

For person detector adaptation, [19, 20] adapted a generic pedestrian detector to a specific traffic scene by collecting training data which passed through multiples checks, including checking the aspect ratio of the detected bounding box, checking whether the detection belongs to a big cluster (if yes, that means it is static background and not a person), comparing with the usual walking paths of the pedestrians in the scene, and making sure the pedestrian does not overlap with a tracked moving vehicle. [90] utilized boosting combined with network-flow tracking to find confident training data which is fed back into the boosting classifier. [30, 91] filtered noisy pseudo-labels by only

selecting person detections which are coherent with tracking results. A multiple instance learning boosting classifier or a random fern classifier was employed to perform learning on top of noisy labels. [92] proposed to combine two independent sources: person detector and background subtraction tracking to collect in-domain person detection training data. [44] proposed to transform the noisy pseudo-label selection problem to a classifier selection problem, where multiple classifiers were trained on subsets of pseudo-labels, and only the classifiers which perform well on the source domain were selected. These classifiers then become an ensemble of weak detectors for the testing domain. [45] proposed to utilize online multi-task learning to adapt an object detector. Each tracked instance had its own set of detector weights, which were updated online yet regularized by the weights of the other detectors which detect the same class of objects. The weights for these instances were averaged to form a generic object detector for that class. Note that most of the aforementioned methods are not limited to person detection and potentially can be applied to other classes of objects.

For generic object detector adaptation, [29, 93, 94] proposed to utilize self-paced learning, adaptive SVMs and large-margin embedding classifiers respectively to adapt a static image detector to video. This is based on the training samples collected by confident detections and tracking in the video. Tracking is advantageous in that new views of the object can potentially be harvested. [31] proposed an effective way to bootstrap new object detectors through a combination of pre-trained CNNs, exemplar learning and region-based tracking.

2.4 Visual Representation Learning with No Supervision

In the advent of very large image and video collections, much research has been done to learn discriminative representations on unlabeled data. The main advantage of these methods is that since no supervision is required, the method can be applied to any data set, and the representations learned will be in-domain for that data set. [95] utilized sparse coding on large numbers of unlabeled images to learn a robust set of bases, which were used to effectively encode other images for image classification. [96] learned discriminative image patches for object detection by selecting patches which are both representative and discriminative. The intuition is that a cluster of patches is discriminative if a reasonably performing SVM could not only be trained based on it but also find a reasonable number of similar looking patches in the validation set. [97] utilized an autoencoder learned on auxiliary natural images to learn a representation which is more robust to variations in single-object tracking. [98] utilized patch tracking to automatically learn a representation for video. The intuition is that the similarity

between two tracked patches should be larger than two randomly selected patches. [99] utilized context to learn an image representation. The intuition is that given a small image patch, a good set of features should have the ability to predict the content in the near vicinity of the image. [100] learned a representation based on sequential verification for video. The intuition is that given three not necessarily consecutive but ordered frames a, b, and c, a good representation should be able to verify whether frame b follows a and precedes frame c. Though the aforementioned methods tackle their respective tasks very differently when compared with weakly supervised learning methods, they all still utilized some sort of assumption (i.e. sparsity, compactness, tracking, context) to constrain the learner to learn something useful.

2.5 Other Tasks Utilizing Weak or No Supervision

In this section, we report on other works which also utilized weak or no supervision.

In order to collect person detection training data in a cheaper way, [101] utilized background subtraction in unlabeled videos to automatically find training samples for person detection. [42] proposed to decrease annotation cost of person detection by only marking the approximate center of mass of a person instead of an entire bounding box. Since the annotations were weaker, background subtraction and an automatically learned person prior were utilized to train the person detector.

For action recognition related tasks, [40] utilized video-level labels and Multiple Instance Learning (MIL) to learn a model which localized actions in both spatial and temporal space in videos. [102] proposed to utilize matrix completion instead of MIL for weakly supervised action localization. [28] proposed to augment its image-based action recognition training data by looking for samples which were very similar to the training set in unlabeled videos. [41] utilized image-level action recognition labels to locate which objects were important for this action. [103] utilized ordering constraints of actions acquired from a movie script as weak label information to learn action detectors.

To collect more action recognition training examples in a cheaper way, our work [104] proposed to utilize the inherent speech-action correlation in instructional videos. An example is shown in Figure 2.1a, where a "cut onion" action is shown. By looking for action signifiers such as "we will" and utilizing a dependency parser to find verb-noun pairs, action examples were collected with the pipeline shown in Figure 2.1b. With this pipeline, we were able to collect a large variety of action training examples as shown in Figure 2.2. For example, instead of just learning the action "cut", our method provided training data which included the objects associated with the action, such as "cut onion",

"cut paper" and "cut hair" as shown in Figure 2.2b. Also, in Figure 2.2a, our system was able to collect diverse positive examples for "drill hole". Holes could either be drilled in wood, in a wall or even in ice. In sum, our unsupervised method is advantageous in that as more instructional videos are uploaded, our system can acquire more diverse action training examples without manual effort. Related work [105, 106] also utilized visual and speech cues to better understand cooking or other instructional videos.

2.6 Summary

This chapter presents an overview of methods which utilized weak supervision or no supervision. As these methods were handicapped in terms of training data, external knowledge combined with task-specific assumptions or constraints were placed to guide the learning process to converge to a reasonable result. In many cases, how the external knowledge or constraints were utilized are the main novelties of the paper. For example, the same spatial-temporal smoothness constraint can be utilized in object discovery, adapting object detectors to video, and learning unsupervised representations. In this thesis, we further extend the same high-level idea of utilizing external knowledge or internal constraints to multi-object tracking and pose estimation.

(A) A collected "cut onion" action example based on the speech-action correlation in instructional videos.

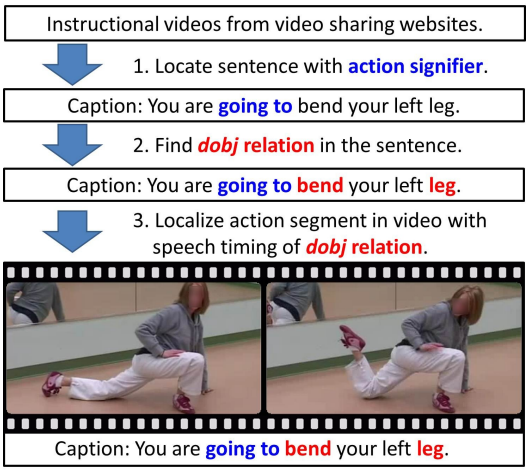

(B) Figure of our pipeline for unsupervised harvesting of action examples from instructional videos.

FIGURE 2.1: Figures depicting the intuition and more detailed pipeline of our method which utilized instructional videos to collect action examples.

(A) Positive "drill hole" examples harvested from instructional videos in an unsupervised fashion. Drilling holes in diverse contexts such as on wood, in walls and on ice were automatically collected.

(B) Positive examples for verb "cut" collected from instructional videos. Our method collected the verb "cut" in many different contexts; from cutting with scissors, knives to paper cutters.

FIGURE 2.2: Figures showing the action examples found within instructional video in an unsupervised manner.

Chapter 3

Multi-Person Tracking with Face Recognition

Surveillance cameras have been widely deployed to enhance safety in our everyday life. In addition, surveillance camera video footage can be used to analyze long term trends in the environment. One first step to analyzing surveillance video is to locate and identify each person in the video. This could be achieved if one had pre-trained identity-specific person detectors which uses gait [107] or appearance [108] to recognize a person. To train these detectors, one needs labeled training data. However, as there will be many unique individuals in a surveillance scene, it will be very difficult and tedious to collect training data for each person and train an identity-specific person detector or gait classifier. Therefore, in order to obtain identity information in an automated way from unlabeled videos and utilize this information to locate each individual at each time instant, we propose to combine face recognition with multi-person tracking.

Face recognition, which is an external knowledge source, enables us to extract identity information from unlabeled videos. However, face recognition is not available for most frames. Therefore, a multi-person tracking algorithm which can utilize face recognition information is proposed to perform identity-aware tracking. Face recognition not only assigns identities to each tracked individual, but also enhances tracking performance by pinpointing the location of a specific individual at a given time. This additional information can lower the chance of identity confusions during the tracking process. The final output is trajectories of different people with identities assigned to each trajectory. This effectively provides the location of each individual at each time instant. The only downside to our approach is that a gallery is required to perform face recognition, which can be created either manually or through face clustering. More details on this issue are in Section 3.9.7.

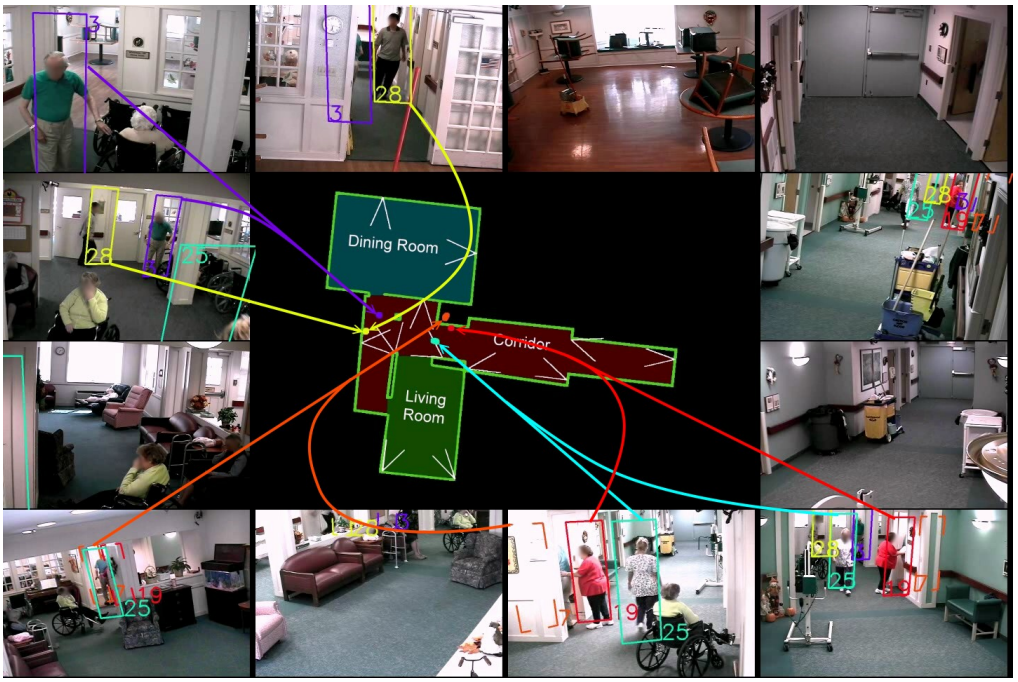

FIGURE 3.1: The Marauder's Map for a nursing home with the map in the middle. Dots on the map show the locations of different people. The surrounding images are the views from each surveillance camera. White lines correspond to the field-of-view of each camera. Due to space limitations, only 12 out of 15 cameras are shown. For clarity, not all arrows are drawn.

Our proposed identity-aware tracking algorithm is as follows. Under the tracking-by-detection framework [109], the tracking task can be viewed as assigning each person detection result to a specific individual. Label information for each specific person is acquired from face recognition. However, as face recognition is not available in most frames, face recognition information is propagated to other frames using a manifold learning approach, which captures the manifold structure of the appearance and spatial layout of the detected people. The manifold learning approach is formulated as a constrained quadratic optimization problem. The constraints included are the mutual exclusion and spatial locality constraints to constrain the final solution to be a reasonable multi-person tracking output, i.e. a person detection can only belong to one individual and an individual cannot be at multiple places at the same time. These constraints make the optimization problem very difficult to solve, so we proposed two optimization methods to solve this problem: nonnegative matrix optimization and the solution path algorithm.

Tracking experiments were performed on challenging data sets including an 116.25 hour and a 4,325 hour complex indoor tracking data set. Our experiments show that our method is effective in localizing and tracking each individual in long-term surveillance video. An example output of our algorithm is shown in Figure 3.1, which shows the

location of each identifed person on a map in the middle of the image. This is analogous to the *Marauder's Map* described in the Harry Potter book series [110].

In sum, the main contributions of this chapter are as follows:

1. We propose an identity-aware multi-object tracking formulation which leverages identity information as label information in a manifold learning framework. The algorithm is formulated as a constrained quadratic optimization problem.
2. We propose two methods to optimize a constrained quadratic optimization problem: nonnegative matrix optimization and the solution path algorithm.
3. Multi-camera multi-object tracking experiments on 4,325 hours of surveillance video in a complex indoor 15-camera environment were performed. To the best of our knowledge, this is the longest multi-camera multi-object tracking experiment to date.

In the following sections, Section 3.1 gives an overview of existing multi-object tracking methods. Section 3.2 gives a high-level overview of the two trackers developed. Details of the two trackers are described from Section 3.3 to Section 3.7. Then experimental results are presented in Section 3.9 and Section 3.10 concludes this chapter.

3.1 Related Work - Multi-Object Tracking

A main line of multi-object tracking work follows the tracking-by-detection paradigm [109], which has four main components: object localization, appearance modeling, motion modeling and data association. The object localization component generates a set of object location hypotheses for each frame. The localization hypotheses are usually noisy and contain false alarms and misdetections, so the task of the data association component is to robustly group the location hypotheses which belong to the same physical object to form many different object trajectories. The suitability of the grouping can be scored according to the coherence of the object's appearance and the smoothness of the object's motion, which correspond to appearance modeling and motion modeling respectively. We now describe the four components in more detail.

3.1.1 Object Localization

There are mainly three methods to find location hypotheses: using background subtraction, using object detectors, and connecting single-frame detection results into tracklets.

The Probabilistic Occupancy Map (POM, [111]) combined background subtraction information from multiple cameras to jointly locate multiple objects in a single frame. It

has been shown to be very effective in multi-camera environments [111–114]. However, POM requires the discretization of the tracking space, and some precision may be lost. Also, when the placement of cameras is non-ideal, such as on long corridors where cameras only view the principal direction of the corridor [2], the POM localization results are not as accurate. Lastly, when there are different kinds of moving objects in the scene, POM cannot distinguish between the different kinds of tracked objects.

Utilizing object detector output is one of the most common ways to localize tracking targets [2, 109, 115–122]. The main advantages of using object detectors are 1) enables the automatic initialization and termination of trajectories, and 2) alleviates template drift as the same detector is used for all frames. The main disadvantage is that a reliable general-purpose detector is required for the object to be tracked.

Localized objects in each frame could be connected to create *tracklets* [113, 123–128], which are short tracks belonging to the same physical object. Tracklets are formed in a very conservative way to avoid connecting two physically different objects. As tracklets merge multiple location hypotheses, they can be used to enhance the efficiency of the tracking process [113].

3.1.2 Appearance Models

Appearance models discriminate between detections belonging to the same physical object and other objects. Color histograms [2, 113, 115, 117, 123, 127, 129–131] have been widely used to represent the appearance of objects and the similarity of the histograms was often computed with the Bhattacharyya distance [117, 131]. Other features such as Histogram of Oriented Gradients [132] have also been used [124, 125].

Appearance models can also be learned from tracklets. The main assumption of tracklets is that all detections in a tracklet belong to the same object, and [124–126, 128, 133, 134] exploited this assumption to learn more discriminative appearance models. Note that the "identity" in our work is different from [125], which utilized person re-identification techniques to improve the appearance model. We, however, focus on the "real-world identity" of the person, which is acquired from face-recognition.

In this work, we utilized color histograms combined with manifold learning to perform tracking. Manifold learning has also been utilized in previous work such as [135, 136] to learn subspaces for appearance features that can better differentiate the tracked target from other targets or background. However, the multi-object tracking performed in [136] utilized multiple *independent* particle filters, which may have the issue of one particle filter "hijacking" the tracking target of another particle filter [137, 138]. Therefore, to fix

this issue, our method has the mutual exclusion and spatial locality constraint encoded in the optimization framework, which *jointly* optimizes for all trajectories to acquire a potentially more reasonable set of trajectories.

3.1.3 Motion Models

Objects usually move in a smooth manner, and effective motion models can capture this assumption to better model the likely movement of objects. [2, 112, 113, 116, 117] used the bounded velocity model to model motion: given the current location of the object, the location in the next frame is constrained by the maximum velocity of the object. [115, 122, 130] improved upon this by modeling motion with the constant velocity model, which is able to model the smoothness of the object's velocity change. Higher order methods such as spline-based methods [119, 121] and the Hankel matrix [139] can model even more sophisticated motions. [128] assumed that different objects in the same scene move in similar but potentially non-linear ways, and the motion of highly confident tracklets can be used to infer the motion of non-confident tracklets.

3.1.4 Data Association

A data association algorithm takes the object location hypotheses, appearance model and motion model as input to find a disjoint grouping of the object location hypotheses which best describes the motion of objects in the scene. Intuitively, the data association algorithm will decide whether to place two object location hypotheses in the same group based on their *affinity*, which is computed from the appearance and motion models.

For the association between multiple frames, there are two popular formulations: the Hungarian algorithm and the network flow, which are both Integer Linear Programs (ILP) with a special form. Given the pair-wise affinities, the Hungarian algorithm can find the optimal bipartite matching between two sets of object location hypotheses in polynomial time [121, 123–125, 127]. In the network flow formulation [112, 114, 116, 117], each path from source to sink corresponds to the trajectory of an object. The network flow problem can also be solved optimally in polynomial time, but this formulation and the Hungarian algorithm formulation makes a number of assumptions. The first assumption is that each physical object can only be associated with one location hypothesis at each time instant. This is to enforce the constraint that an object cannot be at multiple places at the same time. However, in multi-camera environments, at a single time instant, location hypotheses from different cameras can all correspond to the same physical individual. Therefore, location hypotheses from different cameras need to be consolidated first with methods such as POM [111] before these methods can be used.

The second assumption is that the cost function of each trajectory can be decomposed into a series of products (or additions) of pair-wise terms [121]. Therefore, most network flow-based methods are limited to the bounded velocity model, i.e. velocity from the previous time instant is not taken into account. [122, 131, 140] improved on this by taking into account three location hypotheses at once, so the constant velocity model can be utilized. However, this comes at the cost of using more complex algorithms such as Lagrangian Relaxation [122] or using a Linear Program solver to approximately solve an ILP [131], where finding the global optimum is no longer guaranteed. Another method to incorporate velocity in such a framework is to utilize tracklets as the basic unit of location hypotheses [123].

Many trackers have been formulated as a general Integer Linear Programming (ILP) problem. [113, 129, 131] solved the ILP by relaxing the integral constraints to continuous constraints and optimizing a Linear Program, where the solution can be computed efficiently. A subsequent branch-and-cut method to find the global optimal to the ILP [131] or a simple rounding step [113] was used to acquire a final discrete solution. [141, 142] formulated tracking as clique partitioning, which can also be formulated as an ILP problem and solved by a heuristic clique merging method. [139] formulated tracking as a General Linear Assignment ILP problem, which was approximately solved with a deterministic annealing "softassign" algorithm [143].

More complex data association methods have also been used, including continuous energy minimization [118], discrete-continuous optimization [119], Block-ICM [121], conditional random fields [120, 126], generalized minimum clique [115] and quadratic programming [130, 144].

Even though each data association method has different merits, many of the aforementioned methods do not utilize actual person identity information such as face recognition. Unfortunately, in many cases it is non-trivial to incorporate identity information into the previously proposed data association frameworks. One quick way to incorporate identity information may be to assign identities to trajectories after the trajectories have been computed. However, problems occur if two different identities are assigned to the same trajectory, and the true identity of the trajectory is no longer clear. Another approach may be to follow [111] and utilize the Viterbi algorithm to find a trajectory which passes through all the identity observations of each person. However, Viterbi search cannot be performed simultaneously over all individuals, and [111] proposed to perform Viterbi search sequentially, i.e. one individual after another. This greedy approach can lead to "hijacking" of another person's trajectory [111], which is not ideal. Therefore, to achieve effective identity-aware tracking, it is more ideal to specially design a data association

framework which can directly incorporate identity information into the optimization process.

Identity-Aware Data Association

Previously proposed data association methods [113, 145], [146] and [2] utilize identity information for tracking. There have been other work which utilizes transcripts from TV shows to perform face recognition and identity-aware face tracking [147, 148], but this is not the main focus of our work.

[113, 145] formulated identity-aware tracking as an ILP and utilized person identification information from numbers written on an athlete's jersey or from face recognition. Results show that the method was very effective in tracking basketball and soccer players, even when there are many occlusions. [113, 145] depended on the global appearance term for assigning identities to detections. However, the global term assumed a fixed appearance template for an object, which may not be applicable in surveillance scenes recorded over many hours as the appearance of the same person may change drastically.

[146] utilized online structured learning to learn a target-specific model, which was used to compute the edge weights in a network flow framework. Though [146] had a stronger appearance model to compensate for drawbacks of network flow methods, it utilized densely-sampled windows instead of person bounding boxes as input, which may be too time-consuming to compute in hundreds of hours long video sequences.

The work in [2] shows that a semi-supervised tracker which utilized face-recognition as sparse label information for each class/individual achieves good tracking performance in a complex indoor environment. However, [2] did not incorporate the spatial locality constraint during the optimization step. Without the constraint, the solution acquired from the optimization step might show a person being in multiple places at the same time, thus this method does not work well for crowded scenes. Also, the method needs a Viterbi search to compute the final trajectories. The Viterbi search requires the start and end locations of all trajectories, which is an unrealistically restrictive assumption for long-term tracking scenarios. We enhance this tracker by adding the spatial-locality constraint term, which enables tracking in crowded scenes and also removes the need for the start and end locations of a trajectory.

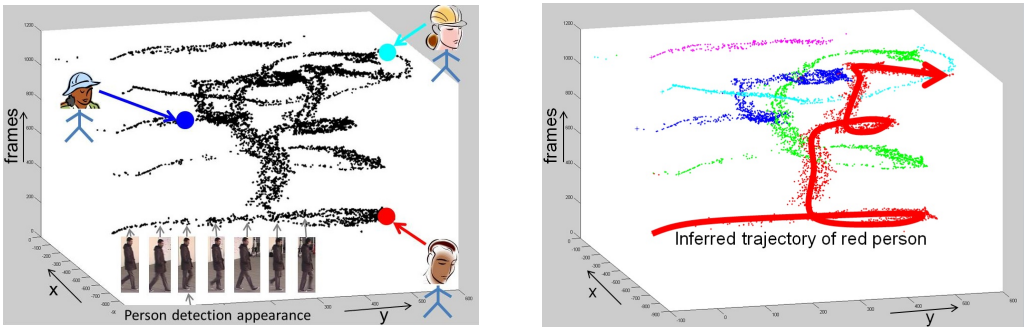

(A) Input to tracking algorithm: location and appearance of person detection and face recognition.

(B) Output of tracking algorithm: partitioning of the person detections into different trajectories.

FIGURE 3.2: Illustration of the input and output of our tracking algorithm. Each person detection is a point in the (x, y, t) space. We assume that people walk on the ground plane, so the z axis is irrelevant. The figures are drawn based on the person detections from the *terrace1* data set [111].

3.2 Tracker Overview

Tracking-by-detection-based multi-object tracking can be viewed as a constrained clustering problem as shown in Figure 3.2. Each location hypothesis, which is a person detection result, can be viewed as a point in the spatial-temporal space, and our goal is to group the points so that the points in the same cluster belong to a single trajectory. A trajectory should follow the mutual exclusion constraint and spatial-locality constraint, which are defined as follows.

- **Mutual Exclusion Constraint**: a person detection result can only belong to at most one trajectory.
- **Spatial-Locality Constraint**: two person detection results belonging to a single trajectory should be reachable with reasonable velocity, i.e. a person cannot be in two places at the same time. This is an instantiation of the spatial-temporal smoothness constraint.

Sparse label information acquired from sources such as face recognition are used to assign real-world identities and also enhance tracking performance.

To compute the trajectories, our tracking algorithm has three main steps.

1. Manifold construction based on appearance and spatial affinity: The appearance and spatial affinity respectively assumes that 1) similar looking person detections are likely to be the same individual and 2) person detections which are spatially and temporally very close to each other are also likely to be the same individual.
2. Spatial locality constraint: This constraint encodes the fact that a person cannot be at multiple places at the same time. In contrast to the manifold created in the

previous step which encodes the *similarity* of two person detections, this constraint encodes the *dissimilarity* of two person detections.

3. Data association: Two different optimization approaches: the nonnegative matrix optimization (NMO) and solution path algorithm (SPA) were proposed to acquire a solution which simultaneously satisfies the manifold assumption, the mutual exclusion constraint and the spatial-locality constraint.

In the following sections, we first define our notations, and then the 3 aforementioned steps are detailed.

3.3 Notations

Given a matrix $\mathbf{A}$, let $\mathbf{A}_{ij}$ denote the element on the i-th row and j-th column of $\mathbf{A}$. Let $\mathbf{A}_i$ denote the i-th row of $\mathbf{A}$. Let $\mathbf{a}_i$ denote the i-th element of vector $\mathbf{a}$. $Tr(\cdot)$ denotes the trace operator. $|\cdot|_F$ is the Frobenius norm of a matrix. Given an integer m, $\mathbf{1}_m \in \mathbb{R}^m$ is a column vector with all ones.

Hereafter, we call a person detection result as an *observation*. Suppose the person detector detects n observations. Let c be the number of tracked individuals, which can be determined by either a pre-defined gallery of faces or the number of unique individuals identified by the face recognition algorithm. Let $\mathbf{F} \in \mathbb{R}^{n \times c}$ be the label assignment matrix of all the observations. Without loss of generality, it is assumed that the observations are reorganized such that the observations from the same class are put together. The j-th column of $\mathbf{F}$ is given by:

$$\mathbf{F}_{*j} = [\underbrace{0, \ldots, 0}_{\sum_{i=1}^{j-1} m_{(i)}}, \underbrace{1, \ldots, 1}_{m_{(j)}}, \underbrace{0, \ldots, 0}_{\sum_{i=j+1}^{c} m_{(i)}}]^T, \tag{3.1}$$

where $m_{(j)}$ is the number of observations in the j-th class. If the p-th element in $\mathbf{F}_{*j}$, i.e. $\mathbf{F}_{pj}$ is 1, it indicates that the p-th observation corresponds to the j-th person. According to Equation 3.1, it can be verified that

$$\mathbf{F}^T\mathbf{F} = \begin{bmatrix} \mathbf{F}_{*1}^T \\ \vdots \\ \mathbf{F}_{*c}^T \end{bmatrix} \begin{bmatrix} \mathbf{F}_{*1} & \ldots & \mathbf{F}_{*c} \end{bmatrix} = \text{diag}\left(\begin{bmatrix} m_{(1)} \\ \vdots \\ m_{(c)} \end{bmatrix} \right) = \mathbf{J}, \tag{3.2}$$

where $\mathbf{J} \in \mathbb{R}^{c \times c}$. The i-th observation is described by a d dimensional color histogram $\mathbf{x}_{(i)} \in \mathbb{R}^d$, frame number $t_{(i)}$, and 3D location $\mathbf{p}_{(i)} \in \mathbb{R}^3$ which corresponds to the 3D location of the bottom center of the bounding box. In most cases, people walk on the

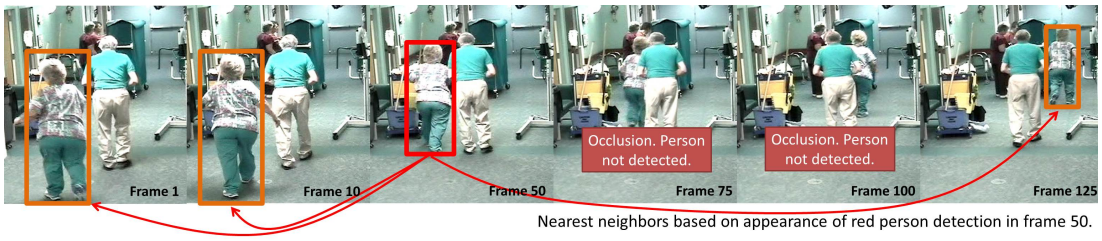

FIGURE 3.3: Intuition of appearance-based nearest neighbor selection. The nearest neighbors for the red person detection in frame 50 are shown. No nearest neighbors are found in frames 75 and 100 as the person is occluded. Nevertheless, once the person is no longer occluded, the nearest neighbor connections can be made again, thus overcoming this occlusion.

ground plane, and the z component becomes irrelevant. However, our method is not constrained to only tracking people on the ground plane.

3.4 Manifold Construction based on Appearance and Spatial Affinity

There are two aspects we would like to capture with manifold learning: 1) appearance affinity and 2) spatial affinity, which will be detailed in the following sections.

3.4.1 Modeling Appearance Affinity

Appearance affinity assumes that if two observations are similar in appearance, then it is very likely that they correspond to the same person. This assumption can be captured with manifold learning, which is usually done in a two-step process. First, suitable nearest neighbors for each observation are found based on similar appearance. Second, the nearest neighbor information of each observation is used to encode the manifold structure with the Laplacian matrix.

Given an observation, suitable nearest neighbors are other similar-looking observations which are spatially and temporally "nearby". More specifically, for the i-th observation, let the set of spatio-temporal neighbors be $\mathcal{M}_{(i)}$. $\mathcal{M}_{(i)}$ contains observations which are not only less than T frames away, but also reachable from location $\mathbf{p}_{(i)}$ with reasonable velocity. This is another instantiation of the spatial-temporal smoothness constraint. To avoid edge cases in computing velocity, we define velocity between observations i and l as follows:

$$v_{(il)} = \frac{\max\left(||\mathbf{p}_{(i)} - \mathbf{p}_{(l)}||_2 - \delta, 0\right)}{|t_{(i)} - t_{(l)}| + \epsilon}. \tag{3.3}$$

ϵ is a small number to avoid division by zero. δ models the maximum localization error of the same person between different cameras due to calibration and person detection errors. So when $t_{(i)} = t_{(l)}$, if the two observations are less than δ apart, these two observations are still spatio-temporal neighbors. Therefore, $\mathcal{M}_{(i)}$ is defined as follows:

$$\mathcal{M}_{(i)} = \left\{ l \mid v_{(il)} \leq V, \left| t_{(i)} - t_{(l)} \right| \leq T, 1 \leq l \leq n \right\}, \tag{3.4}$$

where V is the maximum possible velocity of a moving person. If the velocity required to move between two observations is too large, then the two observations cannot be the same individual. Given $\mathcal{M}_{(i)}$, we look for observations in the set which have color histograms similar to observation i, as it is likely these observations will belong to the same physical individual. To compute the similarity between two color histograms $\mathbf{H}_i$ and $\mathbf{H}_j$, the exponential-χ^2 metric is used:

$$\chi^2(\mathbf{H}_i, \mathbf{H}_j) = exp\left(-\frac{1}{2} \sum_{l=1}^{d} \frac{(\mathbf{H}_{il} - \mathbf{H}_{jl})^2}{\mathbf{H}_{il} + \mathbf{H}_{jl}} \right), \tag{3.5}$$

Based on Equation 3.5, two color histograms are similar only if their similarity is above a certain threshold γ. Finally, the set of nearest neighbors for observation i is found by selecting the top k nearest neighbors in $\mathcal{M}_{(i)}$ which have a similarity score larger than γ. We denote this set as $\mathcal{N}_{(i)} \subseteq \mathcal{M}_{(i)}$.

This method of finding neighbors makes our tracker more robust to occlusions. Occlusions may cause the tracking target to be partially or completely occluded. However, the tracking target usually reappears after a few frames. Therefore, instead of trying to explicitly model occlusions, our system tries to connect the observations of the tracking target before and after the occlusion. As shown in Figure 3.3, despite heavy occlusions, the algorithm can still link the correct detections after the occlusion. The window size T affects the tracker's ability to recover from occlusions. If T is too small, the method will have difficulty recovering from occlusions that last longer than T. However, a large T may increase chances of linking two different objects.

Once the nearest neighbors for each observation have been computed, the manifold structure can be encoded with a Laplacian matrix as follows. We first compute the affinity matrix $\mathbf{W}$, where $\mathbf{W}_{ij} = \chi^2(\mathbf{H}_i, \mathbf{H}_j)$ if $j \in \mathcal{N}_{(i)}$ and 0 otherwise. Then, the diagonal degree matrix $\mathbf{D}$ of $\mathbf{W}$ is computed, i.e. $\mathbf{D}_{ii} = \sum_{l=1}^{n} \mathbf{W}_{il}$. Finally, the Laplacian matrix $\mathbf{L}$ which captures the manifold structure in the appearance space is $\mathbf{L} = \mathbf{D} - \mathbf{W}$.

3.4.2 Modeling Spatial Affinity

Other than modeling person detections of similar appearance, person detections which are "very close" (e.g. a few centimeters apart) in the same or neighboring frames are also very likely to belong to the same person. This assumption is reasonable in a multi-camera scenario because multiple detections will correspond to the same person, and due to calibration and person detection errors, not all detections will be projected to the exact same location. In this case, regardless of the appearance difference which may be resulting from non-color-calibrated cameras, these detections should belong to the same person. We therefore encode this information with another Laplacian matrix $\mathbf{K} \in \mathbb{R}^{n \times n}$ defined as follows. Let $\mathcal{K}_{(i)}$ be the set of observations which are less than distance $\tilde{D}$ away and less than $\tilde{T}$ frames away, i.e.,

$$\mathcal{K}_{(i)} = \left\{ l \mid ||\mathbf{p}_{(i)} - \mathbf{p}_{(l)}||_2 \leq \tilde{D}, \left|t_{(i)} - t_{(l)}\right| \leq \tilde{T}, 1 \leq l \leq n \right\}. \tag{3.6}$$

We compute the affinity matrix $\mathbf{A} \in \mathbb{R}^{n \times n}$ from $\mathcal{K}_{(i)}$ by setting $\mathbf{A}_{ij} = 1$ if $j \in \mathcal{K}_{(i)}$ and $\mathbf{A}_{ij} = 0$ otherwise. Define $\hat{\mathbf{D}} \in \mathbb{R}^{n \times n}$ as a diagonal matrix where $\hat{\mathbf{D}}_{ii}$ is the sum of $\mathbf{A}$'s i-th row. Following [149], the normalized Laplacian matrix is computed: $\mathbf{K} = \mathbf{I} - \hat{\mathbf{D}}^{-\frac{1}{2}}\mathbf{A}\hat{\mathbf{D}}^{-\frac{1}{2}}$. In contrast to computing the appearance affinity, the spatial affinity does not take into account appearance at all, thus the parameters $\tilde{D}$ and $\tilde{T}$ are both set very conservatively to avoid connecting to person detections from different individuals. For example, in our experiments $\tilde{D} = 20$ centimeters and $\tilde{T} = 6$ frames, while $T = 8$ seconds.

Then the loss function which combines the appearance and spatial affinity is as follows:

$$\begin{gathered} \min_{\mathbf{F}} Tr\left(\mathbf{F}^T(\mathbf{L} + \mathbf{K})\mathbf{F}\right) \\ s.t. \text{ columns of } \mathbf{F} \text{ satisfy Equation 3.1}, \ \forall i \in \mathcal{Y}, \ \mathbf{F}_i = \mathbf{Y}_i. \end{gathered} \tag{3.7}$$

Minimizing the loss term will result in a labeling which follows the manifold structure specified by appearance and spatial affinity. The first term in the constraint specifies that the label assignment matrix $\mathbf{F}$ should be binary and have a single 1 per row. The second term in the constraints is the face recognition constraint. Face recognition information is recorded in $\mathbf{Y} \in \mathbb{R}^{n \times c}$, where $\mathbf{Y}_{ij} = 1$ if the i-th observation belongs to class j, i.e. the face of observation i is recognized as person j. $\mathbf{Y}_{ij} = 0$ if we do not have any label information. There should only be at most a single 1 in each row of $\mathbf{Y}$. $\mathcal{Y} = \{i \mid \exists j \ s.t. \ \mathbf{Y}_{ij} = 1\}$ are all rows of $\mathbf{Y}$ which have a non-zero element (i.e. a recognized face). As face verification is approaching human-level performance [150], it is in most cases reasonable to treat it as a hard constraint. Experiments analyzing the effect of face recognition errors on tracking performance are detailed in Section 3.9.7.

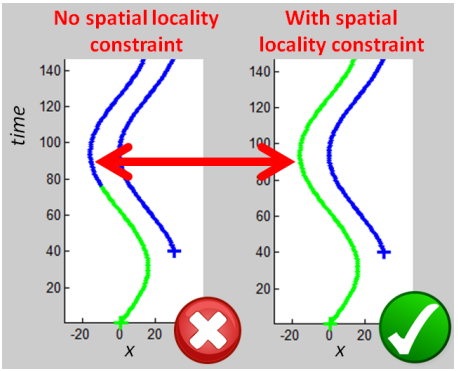

FIGURE 3.4: Example of synthetic tracking output with and without the spatial locality constraint. Without the spatial locality constraint (e.g., [2]), the blue trajectory takes over the green trajectory at around time 80. The blue trajectory is at two places at the same time, which is wrong. With the spatial locality constraint, the results are correct.

3.5 Spatial Locality Constraint

A person cannot be in multiple places at the same time. A tracker which cannot model this constraint, such as [2], might unreasonably state that a person is in multiple places at the same time. Figure 3.4 shows an example of results acquired with and without the constraint. The results computed with the spatial locality constraint are much more realistic. We incorporate the spatial locality constraint into our tracker by modeling pairwise person detection constraints. Given a pair of person detections (i, j), if the speed $v_{(ij)}$, which is defined in Equation 3.3, required to move from one person detection to the other is too large, then it is highly unlikely that the pair of person detections will belong to the same person. We denote $\mathcal{T} = \{(i,j) \mid v_{(ij)} > V, 1 \leq i, j \leq n\}$ as all the person detection pairs which are unlikely to be the same individual. Then the updated loss function is as follows.

$$\begin{gathered} \min_{\mathbf{F}} Tr\left(\mathbf{F}^T(\mathbf{L}+\mathbf{K})\mathbf{F}\right) \\ s.t.\ \forall (i,j) \in \mathcal{T}, \mathbf{F}_{il}\mathbf{F}_{jl} = 0, 1 \leq l \leq c \\ \text{\& columns of } \mathbf{F} \text{ satisfy Equation 3.1, } \forall i \in \mathcal{Y}, \mathbf{F}_i = \mathbf{Y}_i, \end{gathered} \tag{3.8}$$

where the term $\mathbf{F}_{il}\mathbf{F}_{jl} = 0$ models the spatial locality constraint.

Note that our spatial-locality constraint is a generalization to what is used in many single-camera multi-object network flow-based trackers [116, 117], where a person not being at two places at the same time is enforced by assuming that a trajectory can only be assigned to a single person detection at one time instant. However, in a multi-camera scenario, it is often the case that multiple detections from different cameras will correspond to the same individual, and the assumption used by network flow-based

trackers may not be applicable here. Therefore, we propose a more general spatial-locality constraint, which can handle the case where multiple detections from a single time instant all correspond to the same individual. In the current formulation, we did not explicitly model the fact that two detections from the same frame cannot belong to the same person, which could be easily added to our method. Also, experiments show that our method already achieves competitive results without this additional constraint, demonstrating the effectiveness of our spatial locality constraint.

The loss function shown in Equation 3.8 strives to find a suitable labeling of observations along the manifold while not violating both constraints: the mutual exclusion constraint and the spatial locality constraint. However, Equation 3.8 is a combinatorial problem as the values of $\mathbf{F}$ are limited to zeroes and ones. This is very difficult to solve and certain relaxation is necessary to efficiently solve the objective function. Therefore, two different optimization strategies are presented to solve Equation 3.8: nonnegative matrix optimization (NMO) and the solution path algorithm (SPA).

3.6 Nonnegative Matrix Optimization

The first optimization methodology utilizing nonnegative matrix optimization techniques is detailed. We relax the form of $\mathbf{F}$ such that the values are continuous, but to enforce the mutual exclusion constraint, certain constraints still need to be enforced. We first observe that according to Equation 3.2, the columns of $\mathbf{F}$ are orthogonal to each other, i.e. $\mathbf{F}^T\mathbf{F} = \mathbf{J}$ is a diagonal matrix. Also, according to the definition of $\mathbf{F}$, $\mathbf{F}$ is nonnegative. Furthermore, according to [151], if both the orthogonal and nonnegative constraints are satisfied for a matrix, then there will only be at most one non-zero entry in each row of the matrix, which is still sufficient in discretizing $\mathbf{F}$ and identifying the class membership of each observation, i.e. the mutual exclusion constraint still holds. Therefore, we relax the form of $\mathbf{F}$, which originally is a binary label-assignment matrix, by only keeping the column orthogonal and nonnegative constraint. This leads to solving Equation 3.9.

$$\begin{aligned} &\min_{\mathbf{F}} Tr\left(\mathbf{F}^T(\mathbf{L}+\mathbf{K})\mathbf{F}\right) \\ &s.t.\ \forall(i,j)\in\mathcal{T}, \mathbf{F}_{il}\mathbf{F}_{jl} = 0, 1 \le l \le c, \\ &\mathbf{F}^T\mathbf{F} = \mathbf{J}, \mathbf{F} \ge 0, \forall i \in \mathcal{Y}, \mathbf{F}_i = \mathbf{Y}_i, \end{aligned} \tag{3.9}$$

where the mutual exclusion constraint is enforced by $\mathbf{F}^T\mathbf{F} = \mathbf{J}$ and $\mathbf{F} \ge 0$. Under these constraints, the values in $\mathbf{F}$ are continuous and no longer binary, but there will still only be *at most* one non-zero entry per row. One big advantage of this relaxation is that now our method can naturally handle false positive detections because $\mathbf{F}$ is now also allowed

to have a row where all elements are zeroes, which corresponds to a person detection not being assigned to any class.

For convenience, we organize the spatial locality constraint in a more concise form. We aggregate all the person detection pairs in $\mathcal{T}$ and encode it in the matrix $\tilde{\mathbf{S}}$, as shown in Equation 3.10.

$$\tilde{\mathbf{S}}_{ij} = \begin{cases} 0 & \text{if } v_{(ij)} \leq V \\ 1 & \text{otherwise} \end{cases}, \ 1 \leq i, j \leq n, \tag{3.10}$$

where V is the maximum possible velocity of a moving person. $\tilde{\mathbf{S}}$ is defined so that if none of the person detection velocity constraints were violated, then $\mathbf{F}_{*j}^T \tilde{\mathbf{S}} \mathbf{F}_{*j} = 0$, where $\mathbf{F}_{*j}$ is the label assignment vector (column vector of $\mathbf{F}$) for the j-th person. We gather this constraint for all individuals and obtain $Tr(\mathbf{F}^T \tilde{\mathbf{S}} \mathbf{F}) = 0$ if none of the constraints were violated. The scale of $\tilde{\mathbf{S}}$ is normalized to facilitate the subsequent optimization step. Let $\mathbf{D}'$ be a diagonal matrix where $\mathbf{D}'_{ii}$ is the sum of row i of $\tilde{\mathbf{S}}$, then the normalized $\mathbf{S} = \mathbf{D}'^{-\frac{1}{2}} \tilde{\mathbf{S}} \mathbf{D}'^{-\frac{1}{2}}$. Finally, we update Equation 3.9 and arrive at Equation 3.11.

$$\begin{gathered} \min_{\mathbf{F}} Tr\left(\mathbf{F}^T (\mathbf{L} + \mathbf{K}) \mathbf{F}\right) \\ s.t.\ Tr(\mathbf{F}^T \mathbf{S} \mathbf{F}) = 0,\ \mathbf{F}^T \mathbf{F} = \mathbf{J}, \mathbf{F} \geq 0, \forall i \in \mathcal{Y}, \mathbf{F}_i = \mathbf{Y}_i, \end{gathered} \tag{3.11}$$

The constraint $\mathbf{F}^T \mathbf{F} = \mathbf{J}$ is a difficult constraint to optimize. If $\mathbf{J}$ is the identity matrix, then $\mathbf{F}^T \mathbf{F} = \mathbf{I}$ forms the Stiefel manifold [152]. Though a few different methods have been proposed to perform optimization with the orthogonal constraint [152–155], many methods require a specific form of the objective function for the optimization process to converge. Therefore, we instead employ the simple yet effective quadratic penalty method [151, 156] to optimize the loss function. The quadratic penalty method incorporates the equality constraints into the loss function by adding a quadratic constraint violation error for each equality constraint. The amount of violation is scaled by a weight τ, which gradually increases as more iterations of the optimization are performed, thus forcing the optimization process to satisfy the constraints. More details on the convergence properties of the quadratic penalty method can be found in [156]. To solve Equation 3.11, we move the constraints $\mathbf{F}^T \mathbf{F} = \mathbf{J}$ and $Tr\left(\mathbf{F}^T \mathbf{S} \mathbf{F}\right) = 0$ into the loss function as a penalty term. We rewrite the objective function as follows:

$$\begin{gathered} \min_{\mathbf{F}} f(\mathbf{F}) = \min_{\mathbf{F}} Tr\left(\mathbf{F}^T (\mathbf{L} + \mathbf{K} + \tau \mathbf{S}) \mathbf{F}\right) + \tau ||\mathbf{F}^T \mathbf{F} - \mathbf{J}||_F^2 \\ s.t.\ \mathbf{F} \geq 0,\ \forall i \in \mathcal{Y}, \mathbf{F}_i = \mathbf{Y}_i. \end{gathered} \tag{3.12}$$

For each τ, we minimize Equation 3.12 until convergence. Once converged, τ is multiplied by 2 and Equation 3.12 is minimized again.

To solve for Equation 3.12 given a fixed τ, we perform projected nonnegative gradient descent [157], which iteratively updates the solution at iteration l, i.e. $\mathbf{F}^{(l)}$, to $\mathbf{F}^{(l+1)}$ as follows:

$$\mathbf{F}^{(l+1)} = P\left[\mathbf{F}^{(l)} - \alpha^{(l)}\nabla\mathbf{f}(\mathbf{F}^{(l)})\right] \tag{3.13}$$

where the projection function P:

$$P[\mathbf{F}_{ij}] = \begin{cases} \mathbf{F}_{ij} & \text{if } \mathbf{F}_{ij} > 0 \\ 0 & \text{otherwise} \end{cases}, \tag{3.14}$$

is an element-wise function which maps an element back to the feasible region, i.e. in this case a negative number to zero. The step size $\alpha^{(l)}$ is found in a line search-like fashion, where we search for an $\alpha^{(l)}$ which provides sufficient decrease in the function value, i.e.

$$f(\mathbf{F}^{(l+1)}) - f(\mathbf{F}^{(l)}) \leq \sigma Tr\left(\nabla f(\mathbf{F}^{(l)})^T(\mathbf{F}^{(l+1)} - \mathbf{F}^{(l)})\right). \tag{3.15}$$

Following [157], $\sigma = 0.01$ in our experiments. The gradient of our loss function f is

$$\nabla f(\mathbf{F}) = 2\left(\mathbf{L} + \mathbf{K} + \tau\mathbf{S}\right)\mathbf{F} + 4\tau\mathbf{F}\left(\mathbf{F}^T\mathbf{F} - \mathbf{J}\right). \tag{3.16}$$

Details on convergence guarantees are shown in [157]. To satisfy the face recognition constraints, the values of $\mathbf{F}$ for the rows in $\mathcal{Y}$ are set according to $\mathbf{Y}$ and never updated by the gradient.

The main advantage of projected nonnegative gradient descent over the popular multiplicative updates for nonnegative matrix factorization [152, 158] is that elements with zero values will have the opportunity to be non-zero in later iterations. However, for multiplicative updates, zero values will always stay zero. In our scenario, this means that if $\mathbf{F}_{ij}^{(l)}$ shrinks to 0 at iteration l in the optimization process, the decision that "observation i is not individual j" is final and cannot be changed, which is not ideal. The projected nonnegative gradient descent method does not have this issue as the updates are additive and not multiplicative.

$\mathbf{J}$ is a diagonal matrix, where each element on the diagonal, $\mathbf{J}_{ii}$, corresponds to the number of observations belonging to class i, i.e. m_i. As m_i is unknown beforehand, m_i is estimated by the number of recognized faces belonging to class i plus a constant β, which is proportional to the number of observations n. In our experiments, we set $\beta = \frac{n}{1000}$.

To initialize NMO, we temporarily ignore the mutual exclusion and spatial locality constraint and only use the manifold and face recognition information to find the initial

Data: Location hypothesis $\mathbf{p}_{(i)}$, $t_{(i)}$, and appearance $\mathbf{x}_{(i)}$, $1 \leq i \leq n$. Face recognition matrix $\mathbf{Y} \in \mathbb{R}^{n \times c}$.
Result: Final label assignment matrix $\mathbf{F}$

Compute Laplacian matrices $\mathbf{L}$, $\mathbf{K}$; // Sec. 3.4
Compute spatial locality matrix $\mathbf{S}$; // Sec. 3.5
Compute diagonal matrix $\mathbf{J}$; // Sec. 3.6
Compute diagonal matrix $\mathbf{U}$ from $\mathbf{Y}$; // Sec. 3.6
Initialize $\mathbf{F}^{(0)}$ with Equation 3.17 ;
$l \leftarrow 0$; // iteration count
$\tau \leftarrow 10^{-4}$; // initial penalty
repeat // Solve for Equation 3.12 with penalty method
  $\tau \leftarrow \tau \times 2$; // gradually increase penalty τ
  repeat // projected gradient descent
    Compute $\mathbf{F}^{(l+1)}$ from $\mathbf{F}^{(l)}$ with Equation 3.13;
    $l \leftarrow l + 1$;
  until *convergence*;
until $\tau \geq 10^{11}$;
return $\mathbf{F}^{(l)}$

Algorithm 1: Main steps in nonnegative matrix optimization tracking algorithm.

value $\mathbf{F}^{(0)}$. $\mathbf{F}^{(0)}$ is obtained by minimizing Equation 3.17.

$$\min_{\mathbf{F}^{(0)}} Tr\left((\mathbf{F}^{(0)})^T(\mathbf{L}+\mathbf{K})\mathbf{F}^{(0)} + (\mathbf{F}^{(0)}-\mathbf{Y})^T\mathbf{U}(\mathbf{F}^{(0)}-\mathbf{Y})\right). \tag{3.17}$$

$\mathbf{U} \in \mathbb{R}^{n \times n}$ is a diagonal matrix. $\mathbf{U}_{ii} = \infty$ (a large constant) if $i \in \mathcal{Y}$, i.e. the i-th observation has a recognized face. Otherwise $\mathbf{U}_{ii} = 1$. $\mathbf{U}$ is used to enforce the consistency between $\mathbf{F}^{(0)}$ and face recognition information. The global optimal solution for Equation 3.17 is $\mathbf{F}^{(0)} = (\mathbf{L}+\mathbf{K}+\mathbf{U})^{-1}\mathbf{U}\mathbf{Y}$ [159].

Finally, once the optimization is complete, we acquire a $\mathbf{F}$ which satisfies the mutual exclusion and spatial locality constraint. Therefore, trajectories can be computed by simply connecting neighboring observations belonging to the same class. At one time instant, if there are multiple detections assigned to a person, which is common in multi-camera scenarios, then the weighted average location is computed. The weights are based on the scores in the final solution of $\mathbf{F}$. A simple filtering process is also utilized to remove sporadic label assignments. In sum, the main steps of our NMO tracker are shown in Algorithm 1.

3.7 Solution Path Algorithm Optimization

We present a different method to perform optimization of Equation 3.8. The label matrix $\mathbf{F}$ is also relaxed so that the values are continuous, but different constraints are

utilized to enforce the mutual exclusion and spatial locality constraint. The mutual exclusion constraint signifies that each row of $\mathbf{F}$ can have at most one non-zero value. The spatial locality constraint specifies that for $(i,j) \in \mathcal{T}$, $\mathbf{F}_{il}\mathbf{F}_{jl} = 0$, or in other words there can only be at most one non-zero value in the vector $[\mathbf{F}_{il}, \mathbf{F}_{jl}]$. These constraints can be modeled with ℓ_0 norm constraints. Given a vector $\mathbf{x} \in \mathbb{R}^b$, the ℓ_p norm of $\mathbf{x}$ is defined as $\|\mathbf{x}\|_p = \left(\sum_{l=1}^{m} \mathbf{x}_l^p\right)^{\frac{1}{p}}$. Then the mutual exclusion constraint can be modeled as $\|\mathbf{F}_i\|_0 \leq 1$. Similarly, for the spatial locality constraint, the constraint can be modeled as $\|[\mathbf{F}_{il}, \mathbf{F}_{jl}]\|_0 \leq 1$. Therefore, we update Equation 3.8 to acquire the following equation.

$$\begin{aligned} &\min_{\mathbf{F}} Tr\left(\mathbf{F}^T(\mathbf{L}+\mathbf{K})\mathbf{F}\right) \\ &s.t.\ \ \forall i \in \mathcal{Y}, \mathbf{F}_i = \mathbf{Y}_i \\ &\|\mathbf{F}_r\|_0 \leq 1, 1 \leq r \leq n \\ &\forall (i,j) \in \mathcal{T}, \left\| \begin{bmatrix} \mathbf{F}_{il} & \mathbf{F}_{jl} \end{bmatrix} \right\|_0 \leq 1, 1 \leq l \leq c. \end{aligned} \tag{3.18}$$

The three constraints in the loss function correspond to face recognition, mutual exclusion and spatial locality constraints. Note that this formulation can also handle false positive detections, because $\|\mathbf{F}_r\|_0 \leq 1$ allows all elements in row r to be zero, i.e. this person detection does not belong to any class.

However, due to the ℓ_0 norm constraints, Equation 3.18 is still difficult to optimize. One naïve fix is to relax the ℓ_0 norm constraints to ℓ_1 norm constraints. This makes the problem convex and easy to solve. However, the relaxation comes at the price that the mutual exclusion and spatial locality constraint will no longer hold in the final solution, which may cause degradation in tracking performance. Therefore, we utilized the solution path algorithm to bridge the solutions computed under the ℓ_1 norm and ℓ_0 norm constraints.

Unlike traditional algorithms which only looks for the solution under a single parameter setting, the solution path algorithm finds the solution under many different parameters. This is done efficiently by utilizing the solution from the previous parameter setting as the initial value for the next parameter setting. The solution path algorithm has been successfully utilized in the machine learning community on problems such as the Lasso [160]. In the Lasso case[1] , the algorithm in [160] can solve for the solution of the Lasso for all regularization parameters $\lambda \in [0, \infty]$ [161]. The solutions for all the λ's are solved sequentially as the algorithm gradually increases the value of λ. The optimization problem solving for $\lambda^{(t)}$ from the t-th iteration is initialized with the solution acquired with $\lambda^{(t-1)}$ from the $(t-1)$-th iteration. In this way, since $\lambda^{(t-1)}$ and $\lambda^{(t)}$ have similar values, the algorithm will converge faster to the new solution compared to random

[1]The loss function of Lasso can be written as $\min_{\mathbf{w}} \frac{1}{2}\|\mathbf{y} - \mathbf{X}\mathbf{w}\|_2^2 + \lambda\|\mathbf{w}\|_1$, where $\mathbf{y} \in \mathbb{R}^m$ is the label, $\mathbf{X} \in \mathbb{R}^{m \times d}$ is the feature matrix, and $\mathbf{w} \in \mathbb{R}^d$ is the weight vector to be learned.

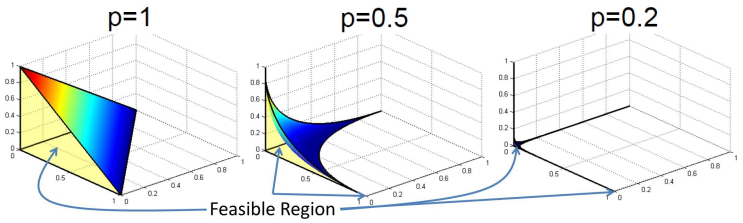

(A) Feasible region of 3 dimensional $\|\mathbf{v}\|_p \leq 1,\ \mathbf{v} \geq 0$ constraint as p decreases from 1, 0.5 to 0.2.

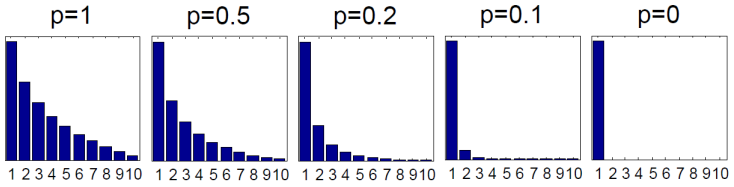

(B) Under 10-dimensional $\|\mathbf{v}\|_p \leq 1$ constraints, average distribution of randomly sampled vectors where the values of each vector are sorted in descending order.

FIGURE 3.5: Images showing that as p decreases, at most 1 non-zero value can remain, thus enforcing the mutual exclusion and spatial locality constraints.

initialization. In sum, the intuition is that if the previous and current parameter settings do not differ by too much, the solution from optimizing with the previous parameter setting can be used as a good initial starting point for the next parameter setting.

In our proposed method, we utilize the solution path algorithm to compute the solution of Equation 3.18. The solution path algorithm acts as a bridge between the two solutions: one with $p = 1$ norm constraints, and the other with $p = 0$ norm constraints. Starting from the solution under the convex ℓ_1 norm constraints, the algorithm successively solves the same optimization problem but under different ℓ_p norm constraints, where p gradually decreases from 1 to 0. The solution path ends as p approaches to 0, and a better solution to our original problem can be obtained. The bridge itself, which consists of the solutions under different ℓ_p norm constraints, is the *solution path* of the whole optimization process.

More specifically, we denote $p^{(m)}$ as the p used during the m-th iteration of the path algorithm. Then $p^{(1)} = 1$, $p^{(M)} \to 0$, and $p^{(m-1)} > p^{(m)}$ for $2 \leq m \leq M$. At each $p^{(m)}$, our system computes the solution $\mathbf{F}^{(m)}$ for Equation 3.18 but under $\ell_{p^{(m)}}$ norm constraints instead. The solution $\mathbf{F}^{(m-1)}$ acquired under $\ell_{p^{(m-1)}}$ norm constraints is used to initialize the optimization process under $\ell_{p^{(m)}}$ norm constraints. The solution $\mathbf{F}^{(1)}$ acquired under ℓ_1 norm constraints is solved directly because Equation 3.18 under ℓ_1 norm constraints is convex and easy to solve. We denote the set $\mathcal{F} = \{\mathbf{F}^{(1)}, \mathbf{F}^{(2)}, \ldots, \mathbf{F}^{(M)}\}$ as the solution path.

The physical meaning of gradually shrinking p is depicted in Figure 3.5. When p is still large, the tracker is not very strict on the mutual exclusion and spatial locality

constraint. However, as p decreases, the ℓ_0 norm constraints are gradually satisfied as at most one value stays non-zero.

In each iteration m of the solution path algorithm, we need to optimize Equation 3.18 under a fixed $p^{(m)}$ to acquire $\mathbf{F}^{(m)}$, and block coordinate descent is utilized.

3.7.1 Block Coordinate Descent

In each iteration m of the solution path algorithm, we need to solve Equation 3.18 under a fixed $p^{(m)} \in [0,\ 1]$ to acquire $\mathbf{F}^{(m)}$. Initialized with $\mathbf{F}^{(m-1)}$, block coordinate descent [162] is utilized to solve Equation 3.18. Block coordinate descent only updates variables of a single observation i while keeping variables of all other observations fixed. The updating of a single observation i is as follows. For notational clarity, we denote $\mathbf{G} = \mathbf{F}^{(m)}$ and p refers to $p^{(m)}$ in this section. We denote the i-th row of $\mathbf{G}$ as $\mathbf{G}_i = \begin{bmatrix}\mathbf{G}_{i1}, & \ldots, & \mathbf{G}_{ic}\end{bmatrix}$. Since all other observations are kept fixed, the loss function for $\mathbf{G}_i$ is simplified from Equation 3.18 to the following quadratic function.

$$\begin{aligned} &\min_{\mathbf{G}_i} \frac{1}{2} \|\mathbf{G}_i - \mathbf{a}\|_2^2 \ \ s.t.\ \|\mathbf{G}_i\|_p \leq 1, \\ &\forall (i,j) \in \mathcal{T}, \left\| \begin{bmatrix}\mathbf{G}_{il}, & \mathbf{G}_{jl}\end{bmatrix} \right\|_p \leq 1, 1 \leq l \leq c, \end{aligned} \tag{3.19}$$

where $\mathbf{a} \in \mathbb{R}^c$. Each element l in $\mathbf{a}$ is computed as follows.

$$\mathbf{a}_l = \frac{\sum_{j=1}^{n} (\mathbf{W}_{ij} + \mathbf{A}_{ij}) \mathbf{G}_{jl}}{\sum_{j=1}^{n} (\mathbf{W}_{ij} + \mathbf{A}_{ij})}. \tag{3.20}$$

$\mathbf{a}$ encodes the label information of the neighbors of observation i. $\mathbf{W}$ and $\mathbf{A}$ are the similarity matrices defined in Section 3.4. If there were no constraints, the optimal value of Equation 3.19 will be $\mathbf{G}_i = \mathbf{a}$, which strives for consistent labeling of an observation with its neighbors. If $\mathbf{G}_i$ contains a recognized face, then row i is not updated. The advantage of block coordinate descent is that non-neighboring observations can be solved in parallel, which makes the optimization process efficient.

To solve Equation 3.19, we notice that the spatial locality constraint only consists of two numbers $\mathbf{G}_{il}$ and $\mathbf{G}_{jl}$, where $\mathbf{G}_{jl}$ is fixed if only observation i is optimized. Therefore, the constraint $\left\| \begin{bmatrix}\mathbf{G}_{il}, & \mathbf{G}_{jl}\end{bmatrix} \right\|_0 \leq 1$ can be converted to the linear constraint $\mathbf{G}_{il} \leq \left(1 - \mathbf{G}_{jl}^p\right)^{\frac{1}{p}} = \mathbf{u}_l$, where, for convenience, $\mathbf{u} \in \mathbb{R}^c$ represents the upper bound of each element in $\mathbf{G}_i$. However, with this simplification, Equation 3.19 is still difficult to solve due to the ℓ_p norm constraint from the mutual exclusion constraint. Therefore the optimization process has two steps. We first clip the values of each element in $\mathbf{a}$ to be at most $\mathbf{u}$ and get the clipped vector $\mathbf{a}'$, i.e. $\mathbf{a}'_l = \min(\mathbf{a}_l, \mathbf{u}_l)$, $1 \leq l \leq c$. Then the following

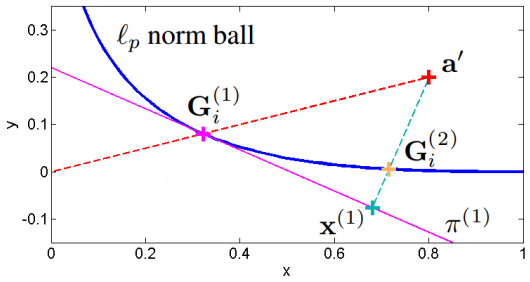

FIGURE 3.6: Illustration of the first iteration of iterative projection method. $\mathbf{G}_i^{(2)}$ is derived from $\mathbf{G}_i^{(1)}$, which is derived from $\mathbf{a}'$.

simplified equation is optimized.

$$\min_{\mathbf{G}_i} \left\|\mathbf{G}_i - \mathbf{a}'\right\|_2^2 \; s.t. \; \|\mathbf{G}_i\|_p \leq 1. \tag{3.21}$$

If $\|\mathbf{a}'\|_p \leq 1$, then the solution of $\mathbf{G}_i = \mathbf{a}'$. Otherwise, Equation 3.21 can be solved by iteratively projecting $\mathbf{a}'$ onto the region $\|\mathbf{G}_i\|_p \leq 1$.

3.7.2 Iterative Projection Method

We propose an iterative projection method to solve Equation 3.21 when $\|\mathbf{a}'\|_p > 1$. For convenience, the region which satisfies $\left\{\mathbf{v} \mid \|\mathbf{v}\|_p \leq 1\right\}$ is referred to as the ℓ_p *norm ball*. Since, $\|\mathbf{a}'\|_p > 1$, it is clear that all local optimal $\mathbf{G}_i^*$ are on the boundary of the ℓ_p norm ball. We denote π^* as the normal of the tangent plane of the ℓ_p norm ball at $\mathbf{G}_i^*$. According to the KKT conditions [162], a (local) optimal point $\mathbf{G}_i^*$ should have the following property: π^* is parallel to the gradient direction of the quadratic function $\|\mathbf{G}_i - \mathbf{a}'\|_2^2$ at $\mathbf{G}_i^*$. Therefore, we propose the following iterative projection method to find a local optimal as shown in Figure 3.6.

To initialize the algorithm, given $\mathbf{a}'$ which $\|\mathbf{a}'\|_p > 1$, we first draw a line between $\mathbf{a}'$ and the origin. Let $\mathbf{G}_i^{(1)} \in \mathbb{R}^c$ be the place where the line intersects the boundary of the ℓ_p norm ball, i.e. $\left\|\mathbf{G}_i^{(1)}\right\|_p = 1$. $\mathbf{G}_i^{(1)}$ serves as the initialization. This intersection can be found efficiently with binary search. Now, given a $\mathbf{G}_i^{(l-1)}$ from iteration $l-1$, we compute $\mathbf{G}_i^{(l)}$ for iteration l as follows. We first compute the tangent plane $\pi^{(l-1)}$ of the ℓ_p norm ball at $\mathbf{G}_i^{(l-1)}$. Next $\mathbf{a}'$ is projected onto $\pi^{(l-1)}$ and the projection is denoted as $\mathbf{x}^{(l-1)}$. We then draw a line between $\mathbf{a}'$ and $\mathbf{x}^{(l-1)}$ and find the intersection of the line with the boundary of the ℓ_p norm ball. The intersection is denoted as $\mathbf{G}_i^{(l)}$, which is the value of $\mathbf{G}_i$ for iteration l. These steps are repeated till convergence. The loss function (Equation 3.21) monotonically decreases with such an update rule, which is proved in Appendix A.

Data: Location hypothesis $\mathbf{p}_{(i)}$, $t_{(i)}$, and appearance $\mathbf{x}_{(i)}$, $1 \leq i \leq n$. Face recognition matrix $\mathbf{Y} \in \mathbb{R}^{n \times c}$, $p^{(1)}, \ldots, p^{(M)}$
Result: solution path $\mathcal{F}$

Compute Laplacian matrices $\mathbf{L}$, $\mathbf{K}$; // Sec. 3.4

// Sol. of convex ℓ_1 norm constraint as initialization

$\mathcal{F} \leftarrow \{\mathbf{F}^{(1)}\}$; // Solution path set
$m \leftarrow 2$; // path algorithm iteration count
repeat // Solution path algorithm, Sec. 3.7
  $\mathbf{G} \leftarrow \mathbf{F}^{(m-1)}$ // Initialize with $\mathbf{F}^{(m-1)}$
  // Solve Equation 3.18 under $\ell_{p^{(m)}}$ norm constraint
  repeat // Block coordinate descent, Sec. 3.7.1
    for $\forall$ *observations* i **do**
      Update $\mathbf{G}_i$ by solving Equation 3.19
    end
  until *convergence*;
  $\mathbf{F}^{(m)} \leftarrow \mathbf{G}$;
  Add $\mathbf{F}^{(m)}$ to $\mathcal{F}$;
  $m \leftarrow m + 1$;
until $m \leq M$;
return $\mathcal{F}$

Algorithm 2: Solution path tracking algorithm.

Finally, once the solution from Equation 3.18 is acquired, we can compute the trajectories from the solution the same way it was computed for the nonnegative matrix optimization method.

The steps of solution path tracking algorithm are summarized in Algorithm 2, and the time complexity is as follows. We optimize Equation 3.18 by updating $\mathbf{G}_i$ with Equation 3.19 for each of the n observations. As proved in Appendix A, the iterative projection algorithm requires $\mathcal{O}\left(c(k + q + \log(c))\right)$ per iteration, where q is the average number of constraints per observation, and k is the number of nearest neighbors of each observation. Thus, solving Equation 3.18 is $\mathcal{O}\left(nc(k + q + \log(c)) * \text{MaxIter}\right)$, which is efficient as it is approximately linear in the number of observations (n), classes (c), nearest neighbors (k), and constraints (q).

The solution path algorithm has two key benefits. First, it can optimize loss functions with ℓ_0 norm constraints, which is a common but difficult-to-optimize constraint in sparsity and relaxed combinatorial problems. Second, the solution path can be viewed as the "decision-making process" of the tracker, which can be utilized to automatically pinpoint uncertainty in tracking for manual correction in an active learning scenario [163]. More details are in Section 3.9.8.

3.8 Comparing Nonnegative Matrix Optimization and Solution Path Algorithm

The two proposed methods: NMO and SPA, all solve the same general loss function: Equation 3.8. The main difference is in how the mutual exclusion constraints were enforced to solve the loss function. For SPA, the mutual exclusion is modeled by $\|\mathbf{F}_i\|_0 \leq 1,\ 1 \leq i \leq n$, which is precisely the mutual exclusion constraint: each row can have at most one non-zero value. For NMO, mutual exclusion is achieved by the constraints $\mathbf{F}^T\mathbf{F} = \mathbf{J}$ and $\mathbf{F} \geq 0$, which is more complex than the constraints of SPA. For SPA, elements on different rows of $\mathbf{F}$ are decoupled. However, for NMO, $\mathbf{F}^T\mathbf{F} = \mathbf{J}$ means that elements on column i have to sum to $\mathbf{J}_{ii}$, thus coupling all elements of $\mathbf{F}$ in the same column. In general, having more complex constraints such as the constraints for NMO often lead to more complex optimization landscapes, thus causing the algorithm to more likely enter a non-ideal local minimum. So we would expect that SPA to perform better than NMO in the tracking task as SPA models the constraints in a simpler and more precise form than NMO.

3.9 Experiments and Results

3.9.1 Data Sets

As our goal is identity-aware tracking, we only focused on tracking sequences in which identity information such as face recognition was available. Therefore, many popular tracking sequences such as the PETS 2009 sequences [164], Virat [165], TRECVID 2008 [166] and Town Centre [167] were not applicable as the faces in these sequences were too small to be recognized. The following four data sets were utilized in our experiments.

terrace1: The 4 camera *terrace1* [111] data set has 9 people walking around in a 7.5m by 11m area for 5000 frames under 25fps, which corresponds to a total of around 13 minutes of video. The scene is very crowded, thus putting the spatial locality constraint to test. The POM grid computed had width and height of 25 centimeters per cell. Person detections were extracted for every frame. As the resolution of the video is low, one person did not have a recognizable face. For the sake of performing identity-aware tracking on this dataset, we manually added two identity annotations for each individual at the start and end of the person's trajectory to guarantee that each individual had identity labels. None of the trackers utilized the fact that these two additional annotations were the start and end of a trajectory. In total, there were 794 identity labels out of 57,202 person detections.

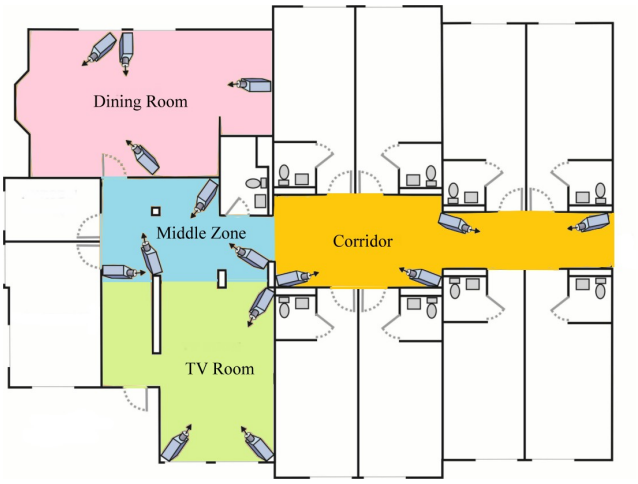

FIGURE 3.7: The approximate location and direction of the cameras in the nursing home. The colored regions are public areas.

Caremedia 6m: The 15 camera *Caremedia 6m* [2, 3] data set has 13 individuals performing daily activities in a 15 camera nursing home scene for 6 minutes 17 seconds, which corresponds to a total of around 94 minutes of video. The data set was first used in [2]. Manual annotations of people standing or walking in the scene were provided every second and further interpolated to every frame. Sitting people were not annotated. The 15 surveillance cameras were set up on the ceilings of the public areas in a nursing home as shown in Figure 3.7. There are many occlusions caused by walls which are typical in indoor scenes. There are also many challenging scenes such as long corridors with sparse camera setups, where heavy occlusions are common. There is also no single camera which has a global view of the whole environment, which is typical in many surveillance camera setups, but atypical in the data sets that have been used to perform multi-camera tracking. The data set records activities in a nursing home where staff maintains the nursing home and assist residents throughout the day. As the data set covers a larger area and is also longer than *terrace1*, we ran into memory issues for trackers which take POM as input when our cell size was 25 centimeters. Therefore, the POM grid computed in our experiments had width and height of 40 centimeters per cell. Person detections were extracted from every sixth frame. In total, there were 2,808 recognized faces out of 12,129 person detections. Though on average there was a recognized face for every 4 person detections, but recognized faces were usually found in clusters and not evenly spread out over time. So there were still long periods of time when no faces were recognized.

Caremedia 8h: The 15 camera *Caremedia 8h* data set [168] has 49 individuals performing daily activities in the same nursing home as *Caremedia 6m*. There is a total of 116.25 hours of video, which corresponds to 7 hours 45 minutes wall time. The videos were recorded on 2005/10/06 from 13:15 to 21:00. Ground truth of standing or walking

people was annotated every minute. Sitting people were not annotated. Person detections were extracted from every sixth frame. In total, there were 70,994 recognized faces out of 402,833 person detections.

Caremedia 23d: The 15 camera *Caremedia 23d* data set consists of nursing home recordings spanning over a 26 day window: 2005/10/06 to 2005/10/31, with 3 days missing (10/13, 10/14, 10/22) due to hardware issues. For 2005/10/06, the recordings are the same as *Caremedia 8h*. For 2005/10/31, the recordings started at 6am and ended at 12pm. For the remaining 21 days, the recordings were from 6am to 9pm. This leads to a total of 4,935 hours of video. To the best of our knowledge, this is the longest sequence to date to be utilized for multi-object tracking experiments, thus enabling us to evaluate tracking algorithms in realistic long-term tracking scenarios. *Caremedia 23d* has 65 individuals performing daily activities in the same nursing home as *Caremedia 6m*. To make the annotation process feasible, ground truth of standing or walking people was annotated every 30 minutes, and annotations were only performed on individuals who have been identified in the first 7 days of the data set. Sitting people were not annotated. Person detections were extracted at every sixth frame. In total, there were 3.1 million recognized faces out of 17.8 million person detections.

3.9.2 Baselines

We compared our method with three identity-aware tracking baselines. As discussed in Section 3.1, it is non-trivial to modify a non-identity-aware tracker to incorporate identity information. Therefore, other trackers which do not have the ability to incorporate identity information were not compared.

Multi-Commodity Network Flow (MCNF): The MCNF tracker [113] can be viewed as an extension of the K-Shortest-Path tracker (KSP, [112]) with identity aware capabilities. The KSP is a network flow-based method that utilizes localization information based on POM. Given the POM localizations, a network flow graph is formed. The algorithm will then find the K shortest paths to the graph, which correspond to the K most likely trajectories in the scene. MCNF further duplicates the graph in KSP for every *identity group* in the scene. The problem is solved with linear programming plus an additional step of rounding non-integral values.

Following [113], we re-implemented the MCNF tracker. In our experiments, the graph is duplicated c times, because for our setup each individual belongs to its own identity group. Gurobi [169] was used as our linear program solver. The global appearance template of each person was computed from the appearance of person detections which had recognized faces. Occlusions were computed from a raw probability occupancy

map, and occluded observations were not used to generate templates nor compare color histograms. Following [113], the input of MCNF was taken from the output of POM and KSP to save computation time. The source code of POM and KSP were from the authors [111, 112]. For trajectories which came closer to three grid cells, the cells in between the two trajectories were also activated so that the MCNF had the freedom to switch trajectories if necessary. This setting is referred to as *MCNF w/ POM*. The base cost of generating a trajectory, which is a parameter that controls the minimum length of the generated tracks, was set to -185 for all *MCNF w/ POM* experiments.

For the two Caremedia data sets, we also took the person detection (PD) output and generated POM-like localization results which were also provided to MCNF. The POM-like localization results were generated by first creating a grid for the nursing home scene, and then aggregating all person detections falling into each grid at each time instant. This setting is referred to as *MCNF w/ PD*. For all *MCNF w/ PD* experiments, the grid size is 40 centimeters, the base cost of generating a trajectory is -60, and detections were aggregated over a time span of 6 frames to prevent broken trajectories. For the *Caremedia 8h* and *Caremedia 23d* set, the Gurobi solver was run in 12,000 frame batches to avoid memory issues.

Lagrangian Relaxation (LR): [146] utilized LR to impose mutual exclusion constraints for identity-aware tracking in a network flow framework very similar to MCNF, where each identity has their own identity specific edges. Lagrange multipliers enforce the mutual exclusion constraint over mutual-exclusive edges in the graph. To optimize with LR, dynamic programming first finds trajectories for each identity given the current network weights. Then, the Lagrange multipliers, which are a part of the network weights, are updated to penalize observations that violate the mutual exclusion constraint. This process is repeated again on the updated network weights till convergence. To fairly compare different data association methods, our LR-based tracker utilized the same appearance information used by all our other trackers, thus the structured learning and densely sampled windows proposed in [146] were not used. Specifically, LR used the same POM-like input and network as MCNF.

Non-Negative Discretization (NND): The Non-Negative Discretization tracker [2] is a primitive version of our proposed tracker. The two main differences are: 1) NND does not have the spatial locality constraint, thus requiring an extra Viterbi trajectory formulation step which needs the start and end of trajectories, and 2) a multiplicative update was used to perform non-negative matrix factorization. NND requires the start and end locations of trajectories, which are usually not available in real world scenarios. In our experiments, therefore, no start and end locations were provided to NND, and the final trajectories of NND were formed with the same method used by our proposed

tracker. NND utilized [159] to build the manifold, but internal experiments have shown that utilizing the method in [159] to build the Laplacian matrix achieved similar tracking performance compared to the standard method [149, 170] of subtracting the degree matrix with the affinity matrix. Therefore, to fairly compare the two data association methods, we utilized the same Laplacian matrix computation method for NND and our method. Also, the spatial affinity term $\mathbf{K}$ was not used in the originally proposed NND, but for fairness, the $\mathbf{K}$ term was added to NND.

3.9.3 Implementation Details

For person detection, we utilized the person detection model from [4, 171]. The person detection results from different camera views were mapped to a common 3D coordinate system using the camera calibration and ground plane parameters provided. Color histograms for the person detection were computed the same way as in [2]. HSV color histograms were used [109, 172]. We split the bounding box horizontally into regions and computed the color histogram for each region similar to the spatial pyramid matching technique [173]. Given L layers, there are $2^L - 1$ partitions for each template. L was 3 in our experiments. Since the person detector only detects upright people, tracking was not performed on sitting people or residents in wheelchairs. For POM, background subtraction was performed with [174].

For our proposed methods: nonnegative matrix optimization (NMO) and solution path algorithm (SPA), the parameters for all four data sets were as follows. The number of nearest neighbors used for appearance-based manifold construction was $k = 25$. The window to search for appearance-based nearest neighbors was $T = 8$ seconds. The fastest velocity one could walk was $V = 3$ m/s. The similarity threshold for looking for nearest neighbors was $\gamma = 0.85$. The maximum localization error was $\delta = 125$ to take into account camera calibration errors. For modeling spatial affinity, $\tilde{D}$ was 20 centimeters and $\tilde{T}$ was 6 frames. When computing the spatial locality constraint, we found that computing the velocity between all pairs of data points will generate too many constraints, thus only conflicting pairs of data points which were less than 6 frames apart were used. The above parameters were also used for NND. For NMO, the initial value of $\tau = 2 \times 10^{-4}$, and the final value was $\tau = 10^{11}$. For SPA, the step size for p was 1.05, i.e. $p^{(m+1)} \leftarrow p^{(m)}/1.05$, and there were a total of $M = 94$ different p values. $p^{(M)} = 0.01$.

For *Caremedia 6m*, *Caremedia 8h*, and *Caremedia 23d*, a preprocessing step to remove incorrect person detections was performed. Person detections with a width/height ratio

less than 0.4 (i.e. a "fatter" person detection, which could be only the upper half of a person) were removed.

Face Recognition

Face information was acquired from the PittPatt software[2], which can recognize a face when a person is close enough to the camera. We assumed that the gallery for the persons-of-interest is provided. There are two options to collect this gallery: 1) manually collect faces of the person or 2) perform face clustering over all detected faces and select clusters which consist of faces corresponding to the person-of-interest. Though the selection requires some manual effort, it does not consume a lot of time as the majority of faces have already been clustered. The latter option was utilized to create the *Caremedia 6m* and *Caremedia 8h* tracking sequences. As the PittPatt clusters are already very clean, and also the clusters were manually mapped, the face recognition was very accurate. Manual verification on *Caremedia 6m* showed 98% accuracy on face recognition.

For the *Caremedia 23d* set, it is too tedious for humans to map clusters into each individual. Therefore, we first manually mapped clusters for 7 days (10/06 to 10/12) of video. Then, based on these mapped clusters, the PittPatt tool was again utilized to perform face recognition on the remaining 16 days of video (10/15 to 10/31, excluding 10/22). Manual verification of the recordings on 2005/10/31 showed that purely automatic face recognition achieves 75% accuracy, which is still reasonable. More details on face recognition performance and its effect on tracking performance are detailed in Section 4.3.3.

For *Caremedia 6m*, *Caremedia 8h*, and *Caremedia 23d*, a preprocessing step to remove face recognitions that are highly likely to be incorrect was performed. First, for each individual, all its person detections with recognized faces were aggregated. Then, for each person detection, the distance between all other aggregated person detections was computed, and the median distance was extracted. Finally, the person detections with median distances in the top 10% were filtered out, i.e. the person detections which looked most dis-similar with the other person detections belonging to the same individual were filtered out.

[2]Pittsburgh Pattern Recognition (http://www.pittpatt.com)

3.9.4 Evaluation Metrics

Identity-aware tracking can be evaluated from a multi-object tracking point of view and a classification point of view. From the tracking point of view, the most commonly used multi-object tracking metric is *Multiple Object Tracking Accuracy* (MOTA[3]) [175, 176]. Following the evaluation method used in [2, 119], the association between the tracking results and the ground truth is computed in 3D with a hit/miss threshold of 1 meter. MOTA takes into account the number of true positives (TP), false positives (FP), missed detections (false negatives, FN) and identity switches (ID-S). Following the setting in [113][4] MOTA is computed as follows:

$$\text{MOTA} = 1 - \frac{\#\text{ FP} + \#\text{ FN} + \log_{10}(\#\text{ ID-S})}{\#\text{ ground truth}}. \tag{3.22}$$

However, the TP count in MOTA does not take into account the identity of a person, which is unreasonable for identity-aware tracking. Therefore, we compute identity-aware true positives (I-TP), which means that a detection is only a true positive if 1) it is less than 1 meter from the ground-truth and 2) the identities match. Similarly, we can compute I-FP and I-MD, which enables us to compute classification-based metrics such as micro-precision (MP $= \frac{\#\text{ I-TP}}{\#\text{ I-TP} + \#\text{ I-FP}}$), micro-recall (MR $= \frac{\#\text{ I-TP}}{\#\text{ I-TP} + \#\text{ I-FN}}$) and a comprehensive micro-F1 ($\frac{2 \times \text{MP} \times \text{MR}}{\text{MP+MR}}$) for each tracker. The *micro*-based performance evaluation takes into account the length (in terms of time) of each person's trajectory, so a person who appears more often has a larger influence to the final scores.

3.9.5 Tracking Results

Tracking results for the four data sets are shown in Table 3.1. As we are more interested in identity-aware tracking, we pay more attention to the F1-score from the classification-based metrics, which will only be high if both precision and recall are high. Our proposed methods: NMO and SPA may not always be the best in terms of MOTA scores, but we achieved the best performance in F1-scores across all four data sets. This means that our tracker can not only track a person well but also accurately identify the individual. Figure 3.9 and Figure 3.10 show some qualitative examples of our tracking result. As there is randomness in SPA, we ran the experiment 5 times and showed the results of the run with median performance. For micro-F1, the 95% confidence intervals for *terrace1*, *Caremedia 6m* and *Caremedia 8h* runs were less than 0.006, thus demonstrating the

[3]Code modified from http://www.micc.unifi.it/lisanti/source-code/.

[4]There are two common transformation functions (denoted as $c_s()$ in [176]) for the identity-switch term, either $\log_{10}$ [113, 176] or the identity function [175]. We have selected the former as this is what was used in MCNF, which is one of our baselines.

Method	Micro-Precision	Micro-Recall	**Micro-F1**	TP	FN	FP	ID-S	**MOTA**
Face only	0.493	0.018	0.035	646	24708	284	5	0.014
KSP w/ POM	N/A	N/A	N/A	22182	2990	767	187	0.852
MCNF w/ POM	0.593	0.532	0.561	21864	3298	644	197	0.844
LR w/ POM	0.609	0.478	0.535	19216	5996	521	147	0.743
NND	0.613	0.238	0.343	8035	17267	1771	57	0.249
NMO w/o SLC	0.704	0.346	0.464	10642	14655	1745	62	0.353
NMO	0.692	0.635	0.663	21370	3873	1783	116	0.777
SPA	0.752	0.705	0.727	22263	2996	1407	100	0.826

(A) Tracking performance on *terrace1* sequence.

Method	Micro-Precision	Micro-Recall	**Micro-F1**	TP	FN	FP	ID-S	**MOTA**
Face only	0.942	0.362	0.523	12369	21641	727	9	0.342
KSP w/ POM	N/A	N/A	N/A	21286	11794	36035	939	-0.406
MCNF w/ POM	0.117	0.238	0.157	23493	9769	44452	757	-0.594
MCNF w/ PD	0.746	0.578	0.652	19941	13749	5927	329	0.422
LR w/ PD	0.802	0.565	0.663	19415	14408	4203	196	0.453
NND	0.861	0.726	0.787	25628	8364	3100	27	0.663
NMO w/o SLC	0.869	0.726	0.791	25578	8408	3080	33	0.662
NMO	0.865	0.755	0.807	26384	7576	3537	59	0.673
SPA	0.871	0.755	0.809	26531	7458	3004	30	0.692

(B) Tracking performance on *Caremedia 6m* sequence.

Method	Micro-Precision	Micro-Recall	**Micro-F1**	TP	FN	FP	ID-S	**MOTA**
Face only	0.858	0.256	0.394	164	471	19	2	0.230
MCNF with PD	0.743	0.418	0.535	265	347	71	25	0.342
LR with PD	0.787	0.405	0.535	261	360	52	16	0.351
NND	0.588	0.505	0.543	314	281	174	42	0.283
NMO w/o SLC	0.638	0.549	0.590	349	257	151	31	0.357
NMO	0.648	0.571	0.607	370	241	149	26	0.386
SPA	0.650	0.581	0.614	375	236	152	26	0.389

(C) Tracking performance on *Caremedia 8h* sequence.

Method	Micro-Precision	Micro-Recall	**Micro-F1**	TP	FN	FP	ID-S	**MOTA**
Face only	0.819	0.199	0.154	125	512	28	2	0.154
MCNF w/ PD	0.712	0.355	0.474	205	412	92	22	0.209
LR w/ PD	0.663	0.357	0.464	215	411	116	13	0.174
NMO	0.698	0.532	0.604	326	299	147	14	0.300
SPA	0.663	0.556	0.605	341	284	180	14	0.326

(D) Tracking performance on *Caremedia 23d* sequence.

TABLE 3.1: Tracking performance of each method on 4 data sets. POM: Probabilistic Occupancy Map proposed in [111] as input. PD: Person detection as input. SLC: Spatial locality constraint. "w/" and "w/o" are shorthand for "with" and "without" respectively. We did not perform the *MCNF w/ POM* on the *Caremedia 8h* and *Caremedia 23h* sequences as it was already performing poorly on the shorter sequence.

stability of our method. NMO and SPA achieved very similar performance, and SPA was only statistically significantly better than NMO for the *terrace1* data set.

The importance of the spatial locality constraint (SLC) is also shown in Table 3.1a. Without the spatial locality constraint in the optimization step (*NND* and *NMO w/o SLC*), performance degraded significantly for *terrace1*, where the tracking scene is extremely crowded and the appearance feature is not very discriminative as most people wear dark clothing. On the other hand, the performance drop on the *Caremedia* sequences was minimal, which could be because of 1) the *Caremedia* sequence is not as crowded as *terrace1*, and 2) people in *Caremedia* sequences have less similar appearance, thus purely relying on color histograms already provide very good performance. We believe both explanations are valid, and more analysis of the second explanation is in Section 4.3.

The MCNF tracker was also a very strong baseline. For *terrace1*, KSP and consequently MCNF achieved very good MOTA results with POM person localization. MCNF was slightly worse than KSP on MOTA scores because though MCNF is initialized by KSP, MCNF is no longer solving a problem with a globally optimal solution. However, for the *Caremedia 6m* sequence, results were poor. Through manual analysis, we found that POM, which is used for person localization in KSP and MCNF, had difficulty in localizing on long corridors where cameras only view the principal direction of the corridor. For example, when there are multiple people on the corridor, their foreground masks tend to merge together into a single blob. Thus there will be many different ways the generative POM model can synthesize the foreground image for each camera view. This leads to ambiguities in person localization, which will significantly hurt tracking performance. Cameras with a side-view on the corridor will significantly alleviate this issue, but this is usually not available in a corridor setting. Also, the indoor scene of *Caremedia 6m* is more complex than *terrace1*. Therefore, even though there are 15 cameras in *Caremedia 6m*, occlusions caused by walls mean that the camera coverage is not as perfect as *terrace1*, thus causing more ambiguities in POM localization. Lastly, there were other non-person moving objects such as carts and rolling closets in the scene, which would also be detected by POM. These ambiguities caused false positives which lead to poor KSP performance. As MCNF input was based on KSP output, *MCNF w/ POM* also performed poorly. However, this is unfair, as MCNF performed poorly due to inaccurate localization, which is unrelated to its data association method. Therefore, to fairly compare MCNF, we provided MCNF with the same localization information used by our method and ran the *MCNF w/ PD* experiment. With the new localization based on person detections, MCNF was able to achieve competitive results. This experiment shows that even if a tracker performs poorly, it may simply be due to a single malfunctioning component, and if the component is switched with another

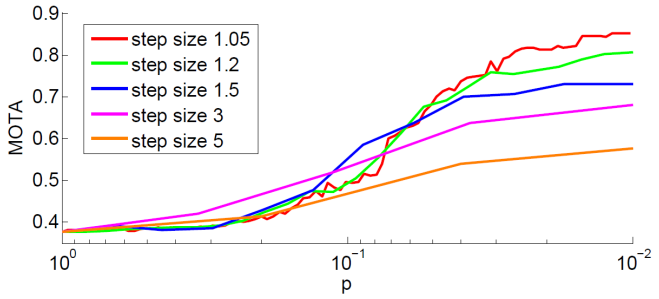

FIGURE 3.8: Tracking performance on *terrace1* data set under different step sizes and ℓ_p norm constraints.

effective component, the tracker can still achieve good results. We believe this is a fairer way of comparing different trackers. Nevertheless, with the same person detection as input, our method still outperformed MCNF in all sequences in terms of F1-score.

The performance of *Face only* clearly shows the contribution of face recognition and tracking. For the Caremedia related sequences, face recognition could already achieve certain performance, but our tracker further improved this performance by roughly 15% absolute, which is still very significant. Furthermore, for *terrace1*, there are very limited faces, thus face recognition plays a minor role in tracking performance. However, we were still able to achieve reasonable performance, which shows that our tracker is effective as most of the heavy-lifting was performed by the tracking algorithm.

For SPA, we also tested the performance under different step sizes s, i.e. $p^{(m+1)} \leftarrow p^{(m)}/s$, for varying values of p on the *terrace1* sequence as shown in Figure 3.8. We can see that smaller step size leads to better MOTA scores, which shows that directly optimizing under ℓ_0 norm constraints (very large step size) may converge to bad local minimum. Also, there is a big performance drop if one only solved the tracking problem under ℓ_1 norm constraints, which only achieves MOTA 0.378. However, by using the solution path algorithm to compute the solution under ℓ_0 norm constraints, SPA was able to improve MOTA to 0.83.

3.9.6 Discussion - Advantages of Tracker

The key advantages of our tracker are as follows:

Face recognition information is integrated into the framework: Face recognition serves as a natural way to automatically assign identities to trajectories in long-term tracking scenarios, where manual intervention is prohibitively costly. When the tracker loses track of a person, face recognition can also aid in automatic re-initialization. Also, in long-term scenarios, it is common that people will change clothes, thus drastically

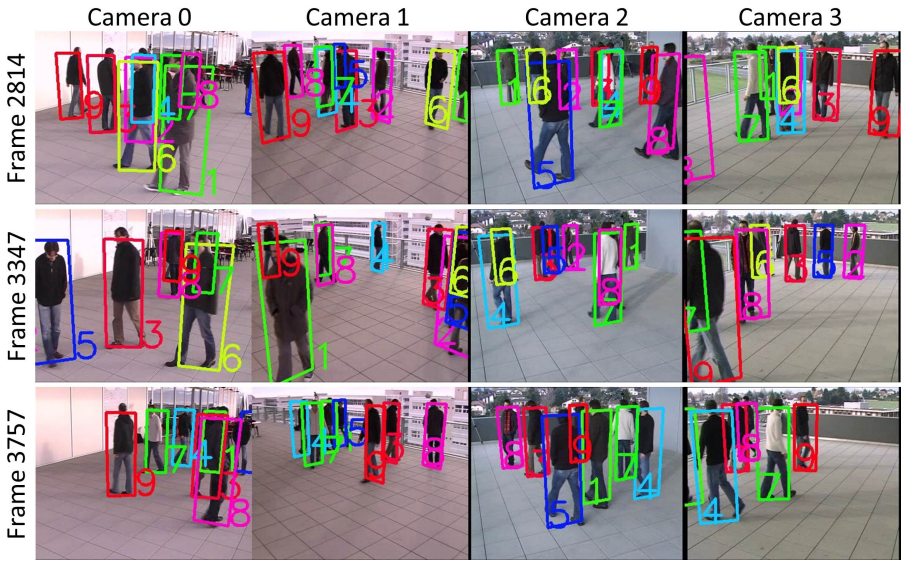

FIGURE 3.9: Snapshots of tracking results from the 4 camera *terrace1* sequence using SPA.

changing their appearance. Face recognition will still be able to recognize this person, making our method robust to large appearance changes of a single person.

Naturally handle appearance changes: Handling appearance changes is crucial because the appearance of the tracking target can change gradually in different parts of the scene. In our tracker, the appearance templates of the tracked target are implicitly encoded in the manifold structure we learn. Therefore, if the appearance of a tracked object changes smoothly along a manifold, our algorithm can model the change. No fixed global appearance model is required to track each individual, and no threshold is required to decide when to adaptively update the appearance model. If there is a drastic change in appearance for a tracked object, then the appearance manifold will highly likely be broken as the nearest neighbor search will not select the detections where the object's appearance changed drastically. However, the spatial affinity Laplacian matrix $\mathbf{K}$ still can potentially connect the correct observations.

Take into account appearance from multiple neighbors: Our tracker models appearance by taking into account the appearance information from multiple neighboring points, which enables us to have a more stable model of appearance. Linear programming and network flow-based methods can only either model appearance globally and assume the appearance of a target will not change, or model appearance similarity only over the previous and next detection in the track.

Handle multiple detections per frame for one individual: In multi-camera scenes, it is common that at one time instant, multiple detections from different cameras correspond to the same physical person. This phenomenon may be difficult to deal with

FIGURE 3.10: Snapshots of tracking results from *Caremedia 8h* data set using NMO. To increase readability, not all arrows are drawn and only 12 out of 15 cameras are shown.

for single-camera multi-object trackers based on network flow [116, 117], because the spatial locality constraint for these methods are enforced based on the assumption that each individual can only be assigned a single person detection per frame. Therefore, multi-camera network flow-based methods such as [112, 113] utilize a two-step process where the POM is first used to aggregate evidences from multiple cameras to perform localization. Then the data association step is used to compute trajectories. The two steps are necessary so that the spatial locality constraint can be enforced for network flow methods. In our case, our formulation of the spatial locality constraint, which is based on the velocity to travel between two detections being under a certain threshold, can be viewed as a generalization of the aforementioned assumption, and this enables us to incorporate the localization and data association steps into a single optimization framework.

No discretization of the space required in multi-camera scenarios: Previous multi-camera network flow methods [112, 113] require discretization of the tracking space in multi-camera scenarios to make the computation feasible. Finer grids run into memory issues when the tracking sequence is long and covers a wide area, and coarser grids run the risk of losing precision. However, our tracker works directly on person detections, and discretization is not necessary.

3.9.7 Discussion - Limitations of Tracker

There are also limitations to our tracker.

Assumes at least one face recognition per trajectory: If there is a trajectory where no faces were observed and recognized, then our tracker will completely ignore this trajectory, which is acceptable if we are only interested in identity-aware tracking. Otherwise, one potential solution is to find clusters of unassigned person detections and assign pseudo-identities to them to recover the trajectories.

Only bounded velocity model employed: To employ the more sophisticated constant velocity model, we could use pairs of points as the unit of location hypotheses, but this may generate significantly more location hypotheses than the current approach.

Assumes all cameras are calibrated: To perform multi-camera tracking, we first map all person detections into a global coordinate system. In order to do so, the intrinsic and extrinsic parameters of the cameras need to be provided. If a camera moves, the updated extrinsic parameters also need to be provided.

Face recognition gallery required beforehand: In order to track persons-of-interest, the gallery is required beforehand. This is the only manual step in our whole system,

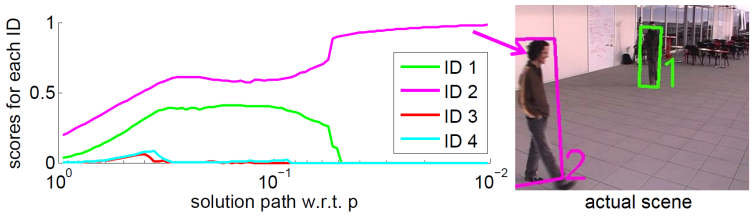

(A) Stable solution path: easy observation. It is clearly ID 2.

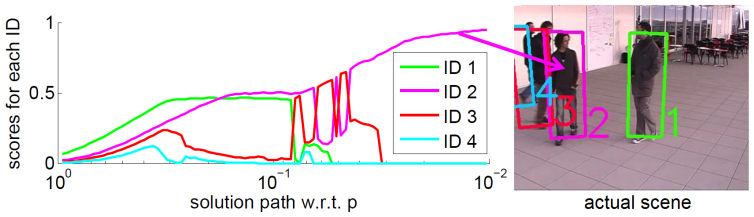

(B) Turbulent solution path: more confusing observation. Could be ID 2 or ID 3 as they are close together.

FIGURE 3.11: Visualization of the decision-making process of our tracker. Easy and confusing examples can be identified.

which could be alleviated when the detected faces are clustered thus making it very efficient for humans to map the face clusters to persons-of-interest. Also, in a nursing home setting, the people we are interested in tracking and observing are fixed, thus this is a one-time effort which could be used for days, weeks or even months of recordings.

Assumes perfect face recognition: The current framework assumes perfect face recognition, which may not be applicable in all scenarios. Therefore, we also analyzed the effect of face recognition errors on tracking performance in Section 4.3.3.

3.9.8 Analyzing the Solution Path

An advantage of the solution path is that it can be utilized to locate uncertainty in the tracker's prediction, which is not addressed in most multi-object trackers. We emphasize that this uncertainty is different from the confidence of detected people or tracklets used by many trackers [117, 177], which focuses on the confidence of the *input data*. In our case we are interested in estimating the confidence of the *output tracking results*. [178] mentioned that the non-integer results acquired from their linear-programming-based multi-object tracker can also be interpreted as the uncertainty of tracking output, but no experiments were performed in this direction.

In this section, we demonstrate how to utilize the solution path to locate potential tracking errors. The solution path records the class membership values in the label matrix $\mathbf{F}$ for all values of p. If the solution path for an observation shows high scores for multiple individuals as shown in Figure 3.11b, this may indicate that the tracker is uncertain, which can be captured with the entropy measure [179]. Specifically, for

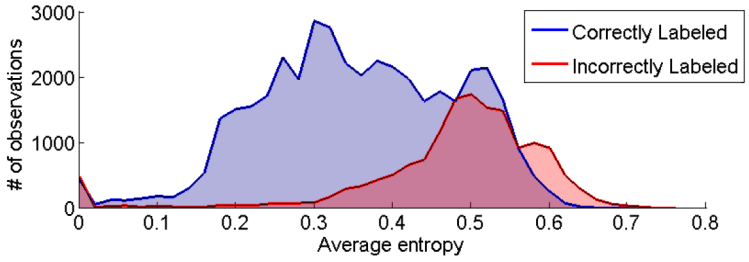

FIGURE 3.12: Entropy histogram of correctly and incorrectly labeled observations for *terrace1*.

iteration m, we denote $\mathbf{G}_i = \mathbf{F}_i^{(m)}$ as the score distribution for the i-th observation. According to the mutual exclusion constraint, $\|\mathbf{G}_i\|_{p^{(m)}} \leq 1$, i.e. $\sum_{j=1}^{c} \mathbf{G}_{ij}^{p^{(m)}} \leq 1$. Then, $\mathbf{G}_{ij}^{p^{(m)}}$ for all $1 \leq j \leq c$ can be viewed as a probability distribution[5] and the entropy is computed as follows: $e_i^{(m)} = -\sum_{j=1}^{c} \mathbf{G}_{ij}^{p^{(m)}} \log\left(\mathbf{G}_{ij}^{p^{(m)}}\right)$. $e_i^{(m)}$ captures the spread of the score distribution for observation i at iteration m. We compute the uncertainty of an observation by summing the entropy of the observation for iterations where $p \in [0.01, 0.1]$, as most fluctuations were observed in this range, i.e. $\bar{e}_i = \sum_{p^{(m)} \in [0.01,0.1]} e_i^{(m)}$.

There are other methods to compute uncertainty, such as computing the residual error for each observation. However, the residual error for a sample is only a single number, but our method provides richer information as the decision process for the whole solution path is taken into account. One may argue that we can also utilize the intermediate results of other optimization methods and treat them as the decision-making process. However, these unconverged intermediate results do not have an obvious physical meaning. For our case, the solution path consists of converged solutions from multiple unique optimization problems. Each solution has clear physical meanings: the class membership hypothesis given the current strictness (value of p) of the mutual exclusion and spatial locality constraint. In sum, our entropy measure provides deeper insights into the tracking process.

To validate our entropy metric, Figure 3.12 shows the histogram of $\bar{e}_i$ for both correctly and incorrectly assigned observations. Figure 3.12 shows that incorrect observations tend to have larger entropy, thus supporting our claims. In the next section, we demonstrate the usage of the entropy measure for improving multi-object tracking in an active learning scenario.

[5]The sum of $\sum_{j=1}^{c} \mathbf{G}_{ij}^{p^{(m)}}$ may not always be 1 if the constraint is not tight, but it is usually 1 in most cases.

3.9.9 Active Learning based on the Solution Path Algorithm

In challenging scenarios, it is inevitable for trackers to make mistakes, and it would be very useful if the tracker can pinpoint potential errors for human verification and labeling. However, human verification is very expensive, thus one should first present to the human annotators the instances which will improve the tracker the most if the labels of the instances were acquired. The task of automatically pinpointing such instances is called active learning [163]. Active learning for efficient manual refinement of tracking results has been explored in [180, 181], which utilizes a *single* object tracker to track multiple objects. In our case our tracker is a *multi*-object tracker which can aid active learning.

A widely used heuristic in active learning is *uncertainty sampling*, i.e. selecting the instances of which the classifier is least certain. Uncertainty sampling is a good fit to our entropy measure, which reflects the uncertainty of our tracker's output. To evaluate our entropy-based sampling method, we performed active learning experiments as follows. The tracker is run iteratively, and after each iteration, the tracker automatically identifies the 5 most confusing observations and requests for their labels. The additional labels are added into $\mathcal{Y}$ and the tracker is rerun. This iteration is repeated 10 times. To select the confusing observations, three methods were utilized: sampling based on entropy values, sampling based on time difference from closest labeled instance (baseline), and sampling based on the residual error (baseline). The sampling based on entropy values favors the observations with higher entropy, i.e., the probability of the i-th observation being selected is $\frac{1}{\text{Rank}(\bar{e}_i)}$, where the rank instead of the absolute entropy values was used to favor higher ranked observations. Time difference sampling favors observations which are furthest away in terms of time from any labeled instance, thus having a higher likelihood of having an identity switch. Residual error sampling favors observations which have a high residual error in the final optimization result. A high residual error may indicate that this observation is incorrect. During sampling, we also add a simple filter to avoid sampling all 5 observations from the same region (within 1 meter) and time (within 2 seconds). The results shown in Figure 3.13 demonstrate that our entropy-based sampling beat the baselines by a large margin. Time difference sampling also shows some gains, but residual sampling performs poorly because high residual error mostly occurs near observations with recognized faces. Recognized faces have a fixed score of 1, but scores of neighboring observations will be significantly smaller (e.g. 0.3 or less), thus causing a large residual error, but labeling observations near recognized faces is not helpful in improving tracking. In sum, our entropy measure for uncertainty sampling is effective in active learning.

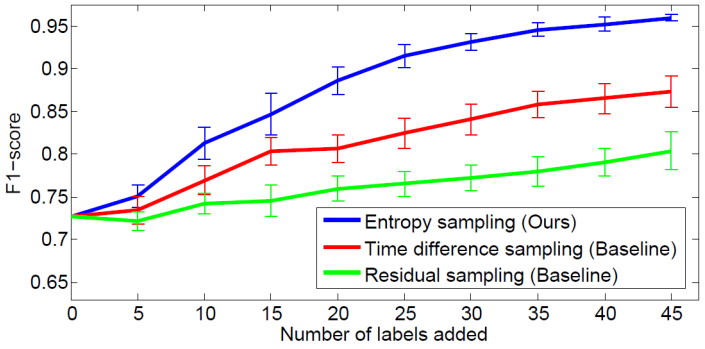

FIGURE 3.13: Performance of tracker in each iteration of active learning on the *terrace1* data set. Experiments for the three sampling methods were performed 20 times each, and the 95% confidence intervals are drawn.

3.10 Summary

In this chapter, we proposed a multi-object tracker which can localize and identify each person at each time instant. The tracker utilizes identity information acquired from external knowledge such as face recognition to not only enhance multi-person tracking performance but also assign a real-world identity to each tracked target. The spatial-temporal smoothness constraint was utilized for modeling appearance/spatial affinity and formulating the spatial locality constraint. We proposed two optimization methods: Nonnegative Matrix Optimization (NMO) and the Solution Path Algorithm (SPA) to solve our tracker's loss function. Experiments showed that our two methods outperform the state-of-the-art, and in general SPA performed slightly better than NMO as it more concisely models the mutual exclusion constraint and the spatial locality constraint.

Our tracker is fully automatic except for the acquisition of the face recognition gallery, which does not require too much effort assuming the people we are observing (in the nursing home) do not change often. We further demonstrated the scalability of our method by applying our tracker on 4,935 hours of surveillance video, where our tracker is able to locate a person-of-interest around 56% of the time with 66% precision. However, in this chapter, we have only explored different optimization methods to enhance tracking. The appearance features utilized are still handcrafted color histograms. In the next chapter, we explore the possibility of utilizing deep appearance features to replace color histograms and further enhance tracking.

Chapter 4

Deep Person Re-Identification for Multi-Person Tracking

Deep learning has not only shown to be very effective in multiple vision tasks such as object recognition [5], pose estimation [182] and single object tracking [97], but it has also been shown to be effective in person re-identification (ReID) [183–185]. The task of person ReID is to classify whether a pair of person detections are the same individual or not. This becomes very challenging when the pair of person detections is detected by different cameras, which leads to a difference in viewpoints of the person and a potential mismatch in color distributions.

On the other hand, previous work has leveraged person ReID techniques to enhance multi-person tracking [125]. Handcrafted features such as HOG [132] and color histograms were utilized to compute the affinity of the appearance of person detections. However, recent work [183–185] have shown that deep features perform significantly better than handcrafted features in person ReID, which motivates us to revisit the task of utilizing person ReID techniques to enhance multi-person tracking. Therefore, in this chapter, we explore the fusion of deep person ReID methods with our proposed multi-object tracker to enhance tracking performance.

A crucial prerequisite for deep learning is to acquire enough training data. To train person ReID networks, one needs a large number of positive (same-person) and negative (different-person) detection pairs. Though there are public person ReID data sets [184] available, these data sets tend to 1) be limited in size and 2) have domain differences with the current data set of interest. Therefore, we propose an unsupervised method to collect large amounts of ReID training data directly from the current data set.

To overcome domain difference and lack of training data, we propose to utilize the spatial-temporal smoothness constraint, which is an internal constraint in video, to automatically collect person ReID training data directly from unlabeled multi-camera surveillance environment footage. The intuition is that a person cannot be at two places at the same time, thus if two separate person detections were detected in a single frame, then they cannot be the same person and is a negative training example. To collect positive examples, the multi-camera setup is utilized. In a small time window, if two cameras both detect a person at the same 3D location, then it is highly likely that the two detections correspond to the same individual and the pair of detections can be treated as a positive sample. Based on the two aforementioned rules which could be utilized in an unsupervised fashion, we were able to utilize thousands of hours of multi-camera surveillance environment footage and automatically collect millions of diverse yet accurate cross-view in-domain person ReID training data to train our networks, which is the key novelty of our method. Experiments show that deep person ReID combined with multi-object tracking further improves tracking performance.

In sum, the contributions of this chapter are as follows.

1. We propose an unsupervised method to collect large amounts of same-view and cross-view person ReID training data. As the method is unsupervised and can be applied directly to the scene of interest, our method is able to overcome issues such as lack of training data and domain mismatch.
2. We present experiments testing multiple deep ReID network architectures on both the person ReID task and the multi-person tracking task. Results show that the deep ReID networks learned based on our collected training examples can significantly improve tracking performance.

In the following sections, Section 4.1 gives an overview of existing deep ReID networks. Section 4.2 describes our proposed training data collection method. Section 4.3 presents experimental results on multi-person tracking and Section 4.4 concludes this chapter.

4.1 Review of Deep Person Re-Identification Networks

To utilize deep ReID for multi-person tracking, we first survey and explore existing deep ReID architectures. There are two popular deep person ReID architectures: the siamese network [183] and the "mixed network" [184, 185] as shown in Figure 4.1. Both network architectures take a pair of person detections as input and learn a model to differentiate whether these two person detections are the same individual or not.

(A) Diagram of the siamese network.

(B) Diagram of the mixed network.

FIGURE 4.1: Diagrams of common deep person ReID architectures during training.

For the siamese network [183], the pair of images goes through the same network (*Network A*), which generates a vector representation of each image. The loss used is the contrastive loss [186], which tries to learn parameters such that positive samples have vector representations which are very close in Euclidean distance, and negative samples are far in Euclidean distance. Negative samples further than a threshold are not penalized.

For the mixed network, the first half of the network is also siamese, where both images go through *Network B*. However, the mixed network will then merge the output of the two *Network B*'s and pass through another *Network C* to get the final output. The final output is a two-class classification prediction which predicts whether the current pair is a positive or negative pair. Therefore, the softmax loss is used to optimize the mixed network. The main novelty of the mixed network is in *Network C*, where previous work has designed specialized layers to compare the similarity of the two person detections. In [184], multiple layers such as the "patch matching" and "maxout-grouping" layers were proposed to handle geometric and photometric differences between the person detections. In [185], the "cross input neighborhood difference", "patch summary features" and "across patch features" layers were proposed to enhance person ReID.

The biggest difference between the two architectures is that siamese networks learn a vector representation for each input image, whereas mixed networks do not. Therefore, the siamese network is ultimately limited to using the Euclidean distance to measure the similarity of two images' vector representation. On the other hand, the mixed network can learn more sophisticated distance metrics than the siamese network because the output of *Network B* goes through *Network C*, which can be viewed as a highly non-linear distance metric to compare the output of the two *Network B*s'. This enables mixed networks to learn more sophisticated relations between person detection pairs. However, the siamese network is advantageous because learning a vector representation which is optimized under the Euclidean distance enables approximate nearest neighbor techniques to be used for k nearest neighbors search. This is very useful in our tracker, because when constructing the manifold, we need to find the k nearest neighbors of each person detection. In order to find nearest neighbors for the mixed network, one can no

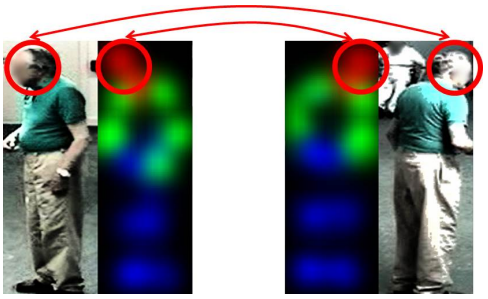

FIGURE 4.2: Visualization of pose estimation results on a person. As the pose estimation output can loosely locate the location of each body part, this could potentially help improve person ReID.

longer utilize approximate nearest neighbor search and is forced to compute all pair-wise person detection comparisons, which is in the order of $\mathcal{O}(n^2)$ and very time consuming.

Experiments on CUHK03

To evaluate the effectiveness of different network architectures, experiments were run on the current largest person ReID data set CUHK03 [184]. CUHK03 has 13,164 images from 1360 pedestrians. For each pedestrian, images from two camera views are provided. For each camera view, there are up to 5 images for the pedestrian. Following [184, 185], person ReID was evaluated as a retrieval task. CUHK03 has defined 20 standardized test sets with 100 people each. For a test set, each of the 100 people was used as queries. For each person/query, the model was given a single image of the person from one view and asked to retrieve the same person in the 100 images of people from the second view. A model performed better if the queried person was found higher up in the ranked list. We aggregated the retrieval results from each of the 100 queries over 20 test sets and drew the standard Cumulative Matching Characteristic (CMC) curve, which plotted the following: for a given rank, the percentage of queries who had their answers found above this rank.

The network architectures and features tested were as follows:

1. HSV Color histograms: the features used for our tracker in Chapter 3.
2. Ahmed et. al. CVPR15: A reimplementation of [185]. There were two differences: 1) hard negative mining was performed by [185] but not in this experiment, and 2) data augmentation by random translation was performed by [185] but not in this experiment. These may have caused a slight drop in performance. The meta-parameters used all follow [185], where the stochastic gradient descent with initial learning rate $\eta^{(0)} = 0.01$ was used. The inverse policy: $\eta^{(i)} = \eta^{(0)}(1 + \gamma \times i)^{-p}$ with $\gamma = 10^{-4}$ and $p = 0.75$ was used to update the learning rate. i denotes the

current mini-batch iteration. The momentum was $\mu = 0.9$ and weight decay was $\lambda = 5 \times 10^{-4}$. The maximum number of iterations was 210K.

3. Ahmed et. al. CVPR15 with pose: An experiment testing whether pose detection [8] results will help in person ReID. An example is shown in Figure 4.2. The hypothesis is that if pose estimation can locate the body parts of the person, this could potentially help match body parts of different person detections and improve person ReID.
4. Alexnet siamese: Our self-implemented siamese network, which is based on a simplified Alexnet [5]. The network has three 5x5 convolutional layers with 96, 256 and 256 filters respectively. Each convolution layer is followed by a ReLU and a max pooling to reduce the input size by a factor of 2. This is followed by two fully connected layers with size 512. The last layer is a contrastive loss layer. For training, stochastic gradient descent with initial learning rate 0.002 was used for the first 12K iterations. Then the learning rate was dropped to 0.0004 and the network was trained for another 12K iterations. The momentum was $\mu = 0.9$ and weight decay was $\lambda = 5 \times 10^{-4}$.
5. Alexnet 6 channels: This network has the exact same network architecture as the "Alexnet siamese" network, but instead of a siamese network, this network is a mixed network without a *Network B*. The two 3 channel RGB input images were directly concatenated to create a 6 channel output, which is fed into our simplified Alexnet. The meta-parameters used to train the model were the same as "Alexnet siamese".

All the models were implemented with Caffe [187]. To train each network, we generated around 30K positives and 600K negatives. The 30K positives included horizontal reflection as data augmentation. The positive-negative ratio during the actual training process was 1:3.

Results are shown in Figure 4.3. Clearly, deep models performed significantly than handcrafted HSV color histograms used by our tracking in Chapter 3. Deep models also performed more or less in the same space. "Alexnet 6 channels" is the best performer, which shows that a network with no specialized layers for person ReID could also perform very well. However, "Alexnet 6 channels" had 8 times more parameters than "Ahmed et. al. CVPR15", which may also be a reason for its good performance. "Ahmed et. al. CVPR15 Reproduce" performed slightly worse than "Ahmed et. al. CVPR15 Original". This may be because we did not do hard negative mining in our implementation, which was shown to be very useful in [185]. Interestingly, adding pose information did not really improve person ReID. Finally, "Alexnet siamese" performed slightly worse than "Alexnet 6 channels", which shows that more complex distance metrics are useful in comparing person detections.

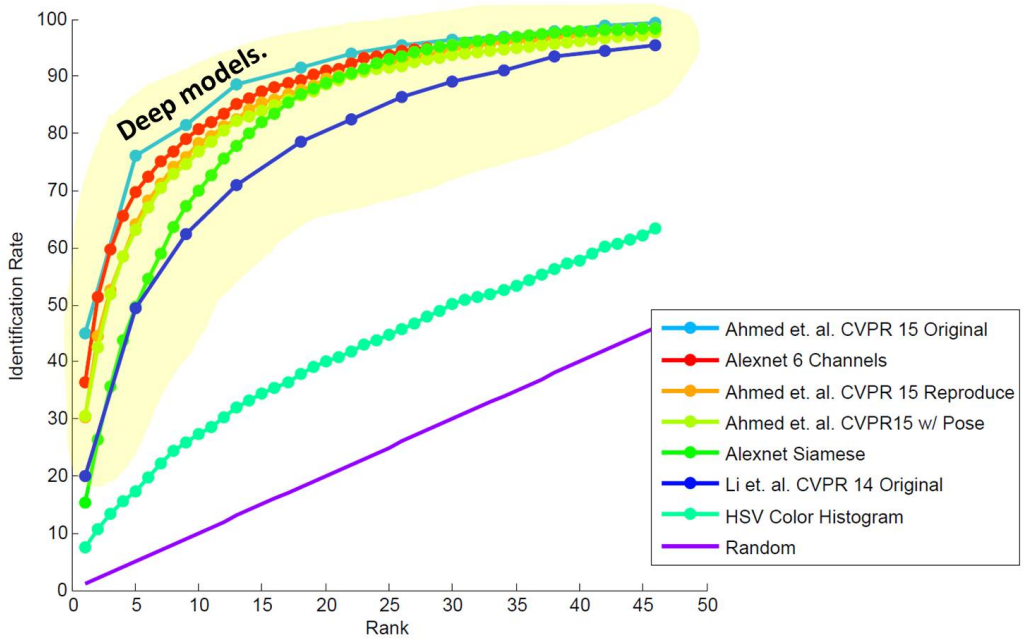

FIGURE 4.3: CMC curve on CUHK03 for different features and network architectures. The runs "Ahmed et. al. CVPR 15 Original" and "Li et. al. CVPR 14 Original" were copied from the respective papers [185] and [184]. The run "Ahmed et. al. CVPR 15 Reproduce" is based on our own implementation of [185].

In sum, our experiments showed that the models we trained are on par with the state-of-the-art [185]. Also, we find that a generic network with more parameters can still perform well or sometimes even better than networks with specialized layers for person ReID. Our next step is to apply these models to multi-person tracking, but before training models, one needs to first collect in-domain person ReID training data for each data set. Therefore, in the next section, we will detail our unsupervised method to collect person ReID training data.

4.2 Unsupervised Collection of Person Re-Identification Training Data

Though person ReID data sets already exist, domain discrepancies between different data sets may cause person ReID performance to drop when an out-of-domain model is utilized. Thus it would be ideal to train person ReID networks on in-domain data. However, it would be very tedious if manual annotation of training data is required for all new data sets. Therefore, we propose an unsupervised method to collect in-domain person ReID training data from multi-camera surveillance scenarios.

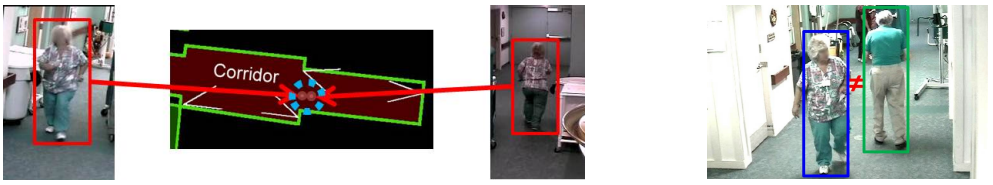

(A) Illustration of a positive example. (B) Illustration of a negative sample.

FIGURE 4.4: Illustration and intuition of how person ReID samples can be collected in an unsupervised manner.

Based on the spatial-temporal smoothness constraint, the fundamental assumption made is that a person cannot be at multiple places at the same time. If two person detections are very close in space and time, then it is highly likely they correspond to the same person. This criterion is used when building the spatial affinity Laplacian matrix (Section 3.4.2) for our tracker, but in this chapter, we instead utilize the criterion to collect positive person ReID training samples. All person detection pairs which qualify the constraints of Equation 3.6 were selected as positive samples. On the other hand, if moving between two person detections exceeds the maximum speed a person can reasonably walk, then it is highly likely they are not the same individual. As this criterion is also used in our tracker, we reused the velocity equation from Equation 3.3 and the velocity constraints from Equation 3.10 to find negative samples. Intuitive examples are shown in Figure 4.4.

The key novelty of our method is extending these two assumptions to the multi-camera setting. The idea of utilizing these two assumptions is not new and has been utilized in other single-view multi-object tracking papers [124, 188]. However, to the best of our knowledge, we are the first work to apply this idea to very large amounts of multi-camera data. The multi-camera scenario enables us to automatically collect large amounts of training pairs with very large viewpoint changes, thus providing abundant data for deep networks to learn an effective cross-camera representation. Examples of collected training data are shown in Figure 4.5.

There are two limitations to our method of unsupervised collection of training data. First, our assumption: a person cannot be at multiple places at the same time, can actually fail when the surveillance cameras are not perfectly time-synchronized. In this case, incorrect negative training data, i.e. person detections of the same person but treated as negative data, could be collected. The second limitation is that we assume the surveillance cameras have significant view overlap. If this view overlap does not exist or is too small, then the system will not be able to harvest large amounts of cross-view positive examples.

4.3 Multi-Person Tracking with Appearance Features from Deep Person Re-Identification Models

In this section, we detail the tracking experiments performed to evaluate the effectiveness of the networks trained on the data collected in an unsupervised manner.

4.3.1 Experiment Setup

Collecting positive and negative samples: We ran the unsupervised data collection process over 4 video sets: 1) *terrace1*, 2) *Caremedia 8h*, 3) a subset of *Caremedia 23d*, which included data sampled from 12 days (10/07 - 10/18) of videos, and 4) the whole *Caremedia 23d* data set. Networks were trained on the collected data and applied to the respective data sets. An exception is *Caremedia 6m*, which utilized the model trained from *Caremedia 8h*.

For each data set, at least 500K positives and 1M negatives were used to train the network. Specifically, we were able to collect 474K (same view) and 109K (different view) positives pairs from *Caremedia 8h*, which has 116.25 hours of video. Note that these numbers are before data augmentation. On the other hand, CUHK03 only has 30K positives after data augmentation such as horizontal reflection. This clearly demonstrates the power of unsupervised collection of training examples, and when we ran our algorithm over the 5000 hours of Caremedia 23-day videos, tens of millions of positive pairs were collected.

Examples of collected training data from *Caremedia 8h* are shown in Figure 4.5, which shows that intra-camera positives look very similar and not very informative. However, inter-camera positives can look very different, yet they all clearly belong to the same person. Therefore, the diverse training data potentially enables the person ReID model to really learn to perform cross-view person ReID.

Network training: During training, 3 different network architectures were utilized: "Ahmed et. al. CVPR15", "Alexnet siamese", and "Alexnet 6 channels". The same training parameters as Section 4.1 were used to train the networks. The only minor change was that for the tracking experiments, the final layer for "Alexnet siamese" only had 252 dimensions instead of 512. This was to match the number of dimensions in the HSV color histogram so that the comparison was fair.

Baseline runs: We had two baselines. The first baseline was the HSV color histogram run, which was based on a handcrafted feature and does not require any training data.

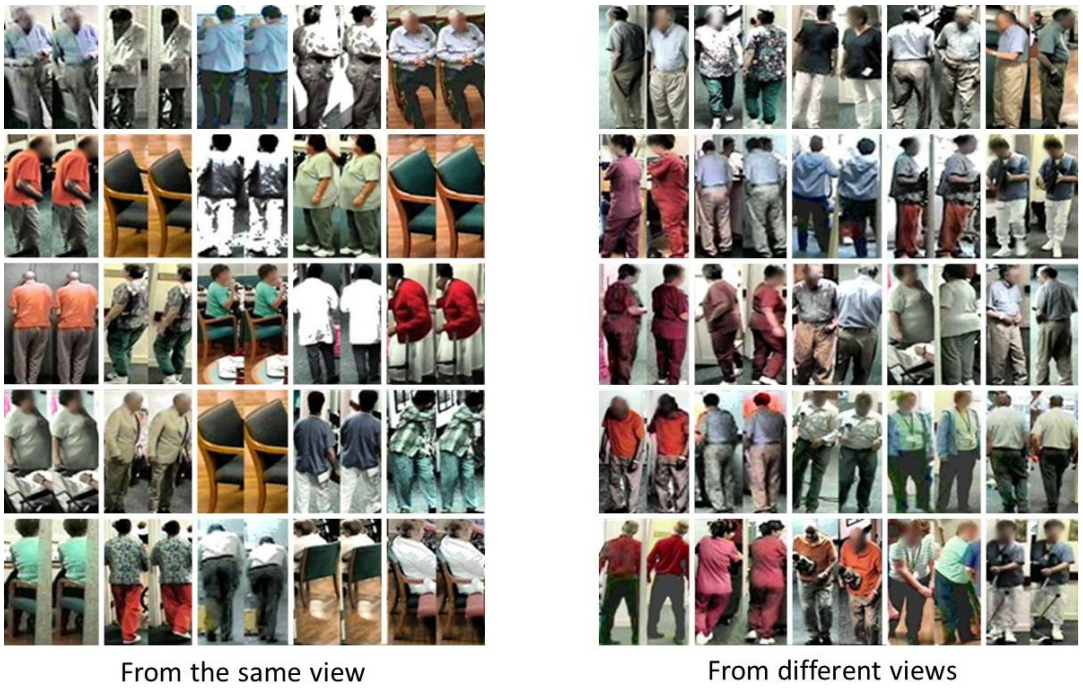

(A) Positive samples.

(B) Negative samples.

FIGURE 4.5: Example of positive and negative samples collected by our method on *Caremedia 8h*.

The second baseline was the tracking run based on the deep ReID network trained on CUHK03, which is an out-of-domain data set with respect to Caremedia.

Tracking parameters: As our deep network features already utilized spatial affinity information, we further shrunk the spatial affinity parameters to $\tilde{D} = 5$ centimeters, and $\tilde{T} = 3$ frames. Also, the appearance similarity threshold was adjusted to $\gamma = 0.99$ to reflect the different scale of confidence output of our network. All other parameters were the same.

4.3.2 Tracking Results and Discussion

Tracking results are shown in Table 4.1. Overall, for Caremedia-based sequences, deep features provided a slight boost in performance. However, on *terrace1*, tracking based on deep features was able to achieve near perfect performance. This demonstrates the effectiveness of our collected training data and deep networks. More detailed discussion is provided in the next few paragraphs.

Why was there a big improvement on *terrace1* but not on *Caremedia 6m*? The huge improvement on *terrace1* based on deep features was mainly due to the lack of discriminative power of the HSV color histogram features for this data set. From Figure 3.9, we can see that most people in the tracking sequence wear dark clothing, which was very challenging for HSV color histogram features. However, there were still enough discriminative cues available to distinguish each person, and the deep networks were able to latch onto these cues based on the training data collected. Note that both HSV color histograms and the "Alexnet siamese" network output were 252-dimensional vector representations, but the "Alexnet siamese" network was able to enhance tracking to near perfect performance. This demonstrates that these deep features are both discriminative and compact. A further qualitative analysis of nearest neighbors found by different features is shown in Figure 4.6. We can see that deep features had the ability to generalize across cameras whereas the color histograms only found nearest neighbors from the same camera. Though cross-camera color differences could be alleviated through the spatial affinity Laplacian matrix, an appearance feature which has the ability to generalize across cameras is still significantly more powerful.

On the other hand, for the *Caremedia* sequences the improvement based on deep features were not as substantial. One key reason is because people in *Caremedia* sequences, as shown in Figure 3.10, were easily distinguished based on their color, thus deep features were not able to significantly surpass HSV color histogram features on this data set.

Method	Micro-Precision	Micro-Recall	**Micro-F1**	TP	FN	FP	ID-S	**MOTA**
Face only	0.493	0.018	0.035	646	24708	284	5	0.014
SPA w/ HSV	0.752	0.705	0.727	22263	2996	1407	100	0.826
SPA w/ siamese trained on CUHK03	0.263	0.271	0.267	16910	7902	8678	547	0.346
SPA w/ Ahmed et. al. CVPR15	0.977	0.962	0.969	24477	852	462	30	0.948
SPA w/ Alexnet 6 channels	0.967	0.947	0.957	24250	1085	575	24	0.934
SPA w/ siamese	0.982	0.972	0.977	24644	697	440	18	0.955

(A) Tracking performance on *terrace1* sequence.

Method	Micro-Precision	Micro-Recall	**Micro-F1**	TP	FN	FP	ID-S	**MOTA**
Face only	0.942	0.362	0.523	12369	21641	727	9	0.342
SPA w/ HSV	0.871	0.755	0.809	26531	7458	3004	30	0.692
SPA w/ siamese trained on CUHK03	0.876	0.646	0.744	22429	11566	2611	24	0.583
SPA w/ Ahmed et. al. CVPR15	0.866	0.788	0.825	27040	6952	4508	27	0.663
SPA w/ Alexnet 6 channels	0.862	0.789	0.824	27120	6880	4044	19	0.679
SPA w/ siamese	0.914	0.745	0.821	25363	8637	2455	19	0.674

(B) Tracking performance on *Caremedia 6m* sequence.

Method	Micro-Precision	Micro-Recall	**Micro-F1**	TP	FN	FP	ID-S	**MOTA**
Face only	0.858	0.256	0.394	164	471	19	2	0.230
SPA w/ HSV	0.650	0.581	0.614	375	236	152	26	0.389
SPA w/ siamese trained on CUHK03	0.648	0.513	0.573	334	287	143	16	0.323
SPA w/ Ahmed et. al. CVPR15	0.694	0.606	0.647	391	237	135	9	0.415
SPA w/ Alexnet 6 channels	0.695	0.606	0.648	389	239	131	9	0.418
SPA w/ siamese	0.713	0.589	0.645	382	251	122	4	0.414

(C) Tracking performance on *Caremedia 8h* sequence.

Method	Micro-Precision	Micro-Recall	**Micro-F1**	TP	FN	FP	ID-S	**MOTA**
Face only	0.819	0.199	0.154	125	512	28	2	0.154
SPA w/ HSV	0.650	0.581	0.614	341	284	180	14	0.326
SPA w/ siamese trained on Caremedia 8h	0.675	0.523	0.589	317	305	161	17	0.269
SPA w/ siamese trained on 12 out of 23 days of Caremedia 23d	0.698	0.573	0.629	348	273	158	18	0.324
SPA w/ siamese trained on Caremedia 23d	0.725	0.574	0.641	355	272	139	12	0.355

(D) Tracking performance on *Caremedia 23d* sequence.

TABLE 4.1: Tracking performance with handcrafted HSV color histograms versus deep models. For brevity, only the Solution Path Algorithm tracker (SPA) from Table 3.1 are shown here. Also, unless otherwise specified, all deep feature-based runs were trained on in-domain data collected from their respective data set.

(A) Nearest neighbors found by color histogram features.

(B) Nearest neighbors found by deep features.

FIGURE 4.6: Visualization of nearest neighbors found by color histograms and deep features.

Feature	*terrace1* NN Error Rate	*Caremedia 6m* NN Error Rate
Color Histograms	0.075	0.064
Deep Features	0.014	0.049

TABLE 4.2: Nearest neighbor (NN) error rate of color histograms and deep features on *terrace1* and *Caremedia 6m*.

We further calculated the error rate of the nearest neighbors (NN) found in the appearance affinity computation step. Results in Table 4.2 show that color histograms make significantly more error on the *terrace1* sequence compared to deep features, thus the large improvement in tracking performance. The similar error rates on *Caremedia 6m* also support the minimal tracking improvement of deep features over color histograms on *Caremedia 6m*. Nevertheless, these results show that the deep network still has learned discriminative features to disambiguate each person in the scene based on the training data collected in an unsupervised manner.

Why is the NN error rate of deep features on *Caremedia 6m* higher than *terrace1*? Table 4.2 shows that the error rate of deep features is similar to color histograms for *Caremedia 6m*, and the hypothesis is that the deep network did not receive enough training data for 1) each individual person and 2) each region / camera view of the nursing home.

To validate the first hypothesis, we first computed the number of ReID training pairs harvested for each individual in *Caremedia 6m* and *terrace1*. Then the number of training

pairs and the tracking F1-score of each individual were plotted as shown in Figure 4.7a. We can clearly see that 1) individuals with many training pairs tend to perform better and 2) individuals in *terrace1* have more pairs than *Caremedia 6m*. These observations support our first hypothesis.

To validate the second hypothesis, we first discretized the nursing home into many regions and then computed the tracking error rate per region. The error was computed by dividing the number of incorrectly classified person detections with the total number of ground-truth in the region. The number of training pairs per region was also computed, and the statistics of each region is shown on a nursing home map in Figure 4.8. Figure 4.8 indicates that regions with higher tracking errors tend to have less training pairs. Therefore, we further correlated the number of training pairs per region with the error rate per region as shown in Figure 4.7b. Results show that regions with more training pairs tend to have lower tracking error rates. The correlation is -0.56.

A qualitative analysis to analyze the cross-camera generalization ability of the feature was further performed. The appearance features corresponding to the same individual were extracted from different camera views, and the pair-wise similarity matrices of the features are shown in Figure 4.9. We can clearly see that cross-camera generalization was successful for Figure 4.9a, which was a region (intersection of the corridor and living room) with many training pairs. However, cross-camera generalization failed completely for Figure 4.9b, which was a region (end of the corridor) with less training pairs. The above observations support our second hypothesis.

In sum, deep features were not as effective on *Caremedia* sequences because the scene had significantly more variability than *terrace1*. There were more people walking around in a larger area which was covered by more cameras. Therefore, the amount of data required to learn all the variations in the scene for all camera pairs was significantly larger. To make matters worse, the amount of training data per person is less than *terrace1*. Therefore, if one is to tackle these challenges, two key points are 1) make sure all regions have enough training pairs and 2) collect training pairs from as many different individuals as possible.

Cross-data set generalization capability of deep networks is limited. As shown in Table 4.1, when we applied an out-of-domain deep network trained on CUHK03 to Caremedia and *terrace1*, performance dropped significantly. Performance on *terrace1* dropped to near random. These results act as a warning that deep networks can easily overfit to the training data, and if the testing data is not in domain, then features acquired from deep networks can hurt performance. Therefore, this makes our unsupervised training data collection method an even more ideal candidate in providing in-domain samples for training deep networks.

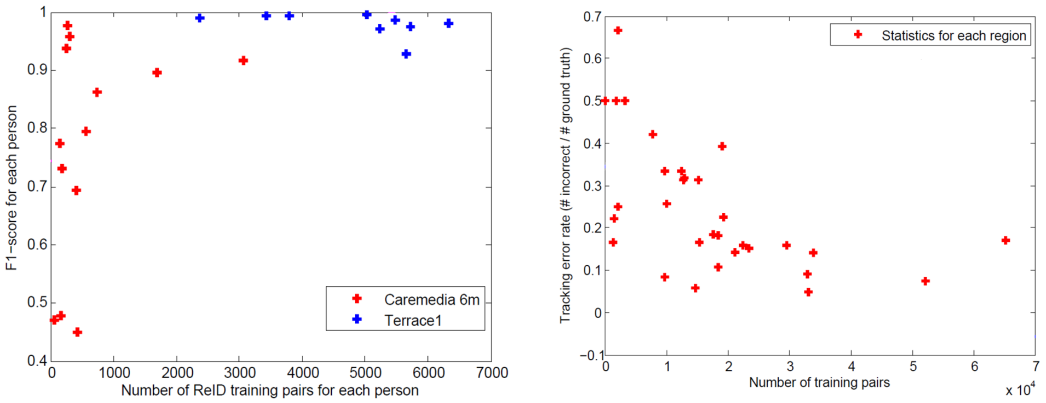

(A) Scatter plot of number of training pairs versus final tracking F1-score for each person.

(B) Scatter plot of number of training pairs versus tracking error rate for each region.

FIGURE 4.7: Figures demonstrating that the number of training pairs used for deep learning is highly correlated with tracking performance.

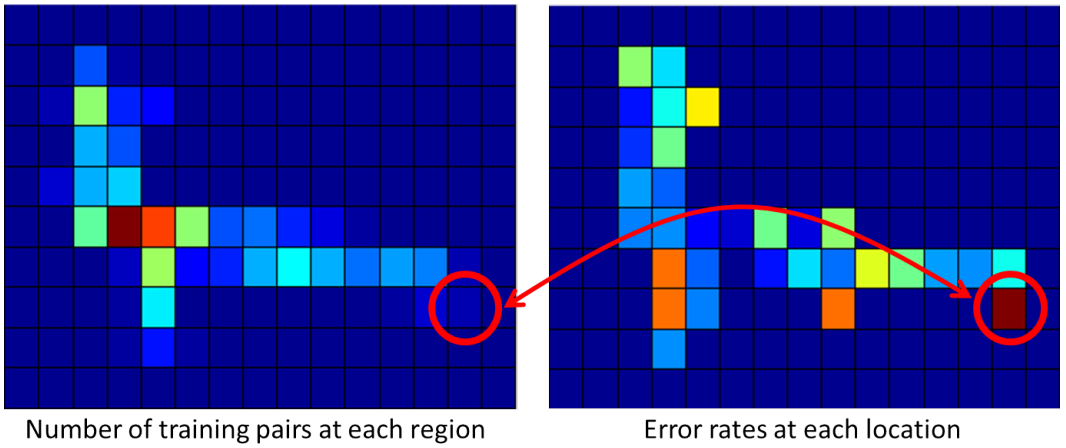

FIGURE 4.8: Statistics including the number of training pairs and error rates at each region in the nursing home. Dark red corresponds to higher values, and dark blue corresponds to lower values.

No clear winner in deep network architectures for tracking. If we compared the performance of different deep network architectures, there is no clear winner. Despite the fact that siamese networks were inferior to other network architectures in the person ReID task, siamese networks performed as well as other networks on all tracking data sets. These results are very encouraging in that siamese networks have the nice property of generating a vector representation for each person detection, thus enabling the utilization of approximate nearest neighbor techniques for efficient nearest neighbor search. This property is crucial because finding nearest neighbors is a fundamental component of our tracker (Section 3.4.1), and if we want to apply our tracker to large-scale or time critical scenarios, one needs to perform nearest neighbor search efficiently. For mixed networks such as "Ahmed et. al. CVPR15" and "Alexnet 6 channels", comparing two person detections requires a feedforward pass through the network, which is

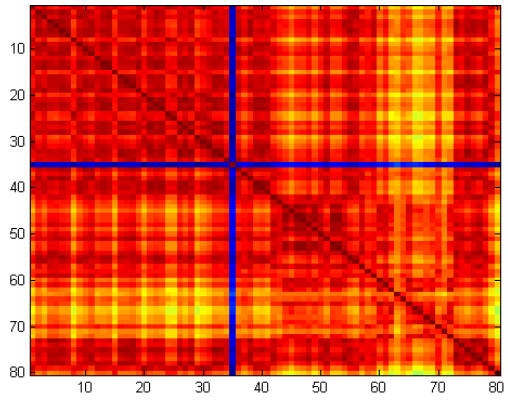

(A) The pair-wise similarity of deep features for 80 detections of the same person. The detections were from four cameras. The camera start/end IDs are 1-33, 34-57, 58-72, 73-80, but as cross-camera generalization was very successful, the "squares" which mark the "boundary" of each camera are no longer obvious. ID 35 is an outlier.

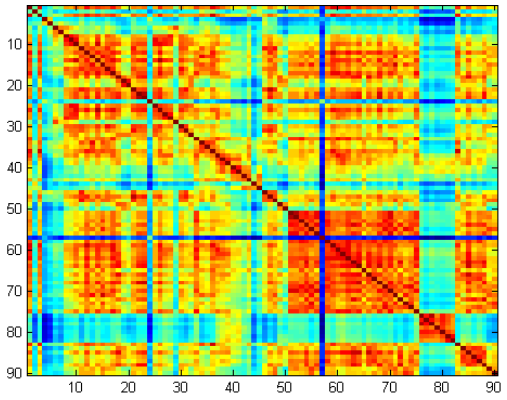

(B) The pair-wise similarity of deep features for 90 detections of the same person. The detections were from five cameras. The camera start/end IDs are 1-45, 46-74, 75-82, 83-85 and 86-90. Cross-camera generalization was not as successful, especially for IDs 75-82, as they are not similar with detections from any other camera.

FIGURE 4.9: Pair-wise similarity of deep features across multiple cameras. Detections from different cameras have been grouped into consecutive IDs, and if there are clear "squares" along the diagonal, then this means that the intra-camera similarity is significantly larger than inter-camera similarity, which implies that cross-camera generalization was not successful.

extremely time consuming and significantly slower than computing the pairwise distance between two vectors. Therefore, this is the main reason why the other two architectures: "Ahmed et. al. CVPR15" and "Alexnet 6 channels" were not run on the *Caremedia 23d* sequence.

Distribution of person appearance varies over different days in *Caremedia 23d*. As shown in Table 4.1d, tracking performance was the best when the deep network was trained on person ReID training data collected over all 23 days. Performance degraded when only 12 days of footage was used to collect training data, and performance further dropped when only the footage from *Caremedia 8h* was used to gather training data. This shows that the distribution of the training data for *Caremedia 8h* is still different compared to *Caremedia 23d*, which means that the distribution of person appearance varies over time even in the same nursing home environment. This demonstrates the importance of being able to automatically collect in-domain training data, which enables our model to automatically adapt to the distribution of a new day.

Already achieves reasonable long-term tracking performance. Examining the performance on the *Caremedia 23d* sequence, our best performing tracker is able to localize a person with 73% precision and 57% recall over 23 days of video. In other words, for a given person, our tracker is able to find him/her 57% of the time, and if

FIGURE 4.10: Challenging scenarios for person detection.

our tracker predicts that a person detection is a given person, then our tracker is correct 73% of the time. Though the performance is not high, but achieving such performance over the 4,935 hours of surveillance video in the *Caremedia 23d* sequence opens the door to automatic surveillance video analysis, which we will demonstrate in Chapter 6.

4.3.3 Analysis of Tracking Errors

Though our tracker was able to achieve near perfect tracking performance on *terrace1*, there is still large room for improvement on the Caremedia sequences. In this section, we analyze the failure cases of our tracker, which may account for the remaining gap between the current performance and perfect performance.

Detection errors/misses: This is one of the main causes of tracking errors. As our tracking algorithm is based on tracking-by-detection, a person which was not detected by the detection algorithm will not be tracked. We performed an analysis on the false negatives of *Caremedia 6m*, which showed that 72.5% were caused by the person detector not being able to detect the person. If the ground-truth instances that have no corresponding detection were removed, the tracking F1-score on *Caremedia 6m* increases from 0.821 to 0.899, which is getting close to near perfect performance. Qualitatively, Figure 4.10 shows some examples of difficult person detection scenarios. These scenarios include difficult poses and occlusion. A possible solution to increase recall is to utilize deep models such as the Faster RCNN [189], which has shown to significantly outperform the Deformable Part-based Models we used.

Face Recognition: As described in Section 3.9.3, manual verification on *Caremedia 6m* shows that 98% of the face recognitions were correct. The high accuracy shows that face recognition errors were not the main cause of the remaining performance gap for *Caremedia 6m*. However, as our purely automatic face recognition performance on *Caremedia 23d* achieves only around 75% accuracy (Section 3.9.3), we analyzed the effect of incorrect face recognition on tracking performance. Face recognition errors at different error rates were randomly generated on the *Caremedia 6m* set. Errors were generated by randomly changing an already recognized face to another person's face. Results are shown in Figure 4.11, which show that performance drops steadily as face

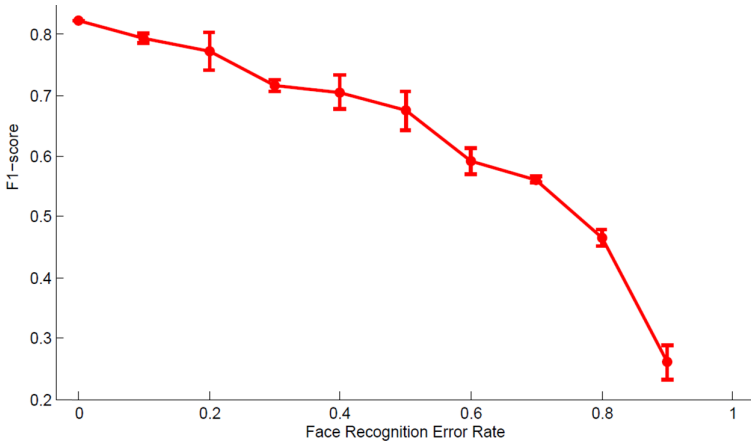

FIGURE 4.11: Analyzing the effect of face recognition errors on tracking performance on *Caremedia 6m*. At each error rate, the experiment was repeated 3 times and the 95% confidence interval is shown.

recognition errors increase, and a 25% error (75% accuracy) lead to around 10% drop in F1, which coincides with the results on *Caremedia 23d*. For the first 7 days in *Caremedia 23* where the face clusters were manually mapped into each person, the average F1 score was 0.699. For the remaining 16 days, where face recognition was computed completely automatically, the F1 score dropped to 0.591, which is a 10% drop. Another potential source of performance drop is when no faces were recognized for a trajectory. In this case, our tracker will completely ignore this trajectory.

Camera Synchronization: This is the other main cause of tracking errors. Due to hardware issues, the Caremedia videos were not time synchronized. To make matters worse, the video encoding process was not completely error free, and many recordings have "holes" which last up to a few seconds. Though the location of the encoding errors could be automatically found, and synchronization with audio was sometimes effective, there were many cases when the videos were still not synchronized. In the worst case, synchronization errors were up to 20 seconds, which will confuse the tracker as the same person could be at more than one place at the same time. Figure 4.12 shows an example.

Camera Calibration: Camera calibration errors were also a source of error. As the nursing home scene no longer exists, the calibration of Caremedia cameras was performed directly on the video footage, and only rough estimates of the intrinsic and extrinsic camera parameters could be acquired. This caused issues in the localization of people. An example is shown in Figure 4.13, where the localization of the yellow bounding box in the lower right camera view was accurate, but the yellow bounding box in the upper right camera view was not accurate. However, as camera calibration errors were only severe at some locations, we believe it does not cause as much error as missed detections, face recognition errors and synchronization issues.

FIGURE 4.12: Example of synchronization error in the Caremedia data set where two sets of cameras provide contradicting information on the location of a person.

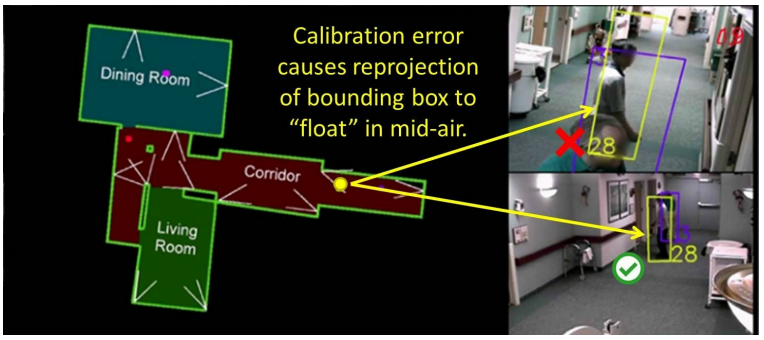

FIGURE 4.13: Example of calibration error in the Caremedia data set. The localization of the yellow bounding box in the upper right camera view was not accurate.

4.4 Summary

In this chapter, we demonstrated the effectiveness of utilizing an internal constraint: spatial-temporal smoothness, to automatically collect large amounts of person ReID training data for training deep ReID models. As the collected samples were accurate, diverse and in-domain, the features acquired from the deep models trained on the collected samples were able to further improve tracking performance. On the *terrace1* sequence, our tracker was able to achieve near perfect performance thanks to the very effective training data collected and the ability of deep networks to learn powerful features to distinguish each person.

Combined with the advances from the current chapter and Chapter 3, our tracker was able to locate a person with 73% precision and 57% recall in 4,935 hours of surveillance video. These promising results motivate and enable us to perform surveillance video summarization, which is detailed in Chapter 6.

Chapter 5

Unsupervised Adaptation of Image-based Pose Detectors to Video

Pose detection focuses on finding the location of each joint of a person, which would be very useful information when trying to understanding the action of a person. For example, in the nursing home environment, through pose estimation of elderly people sitting in a dining room, we can automatically compute the eating speed (frequency of food to mouth) of each elderly person, which would be very useful in assessing the person's state of health.

Pose estimation algorithms have been developed for analyzing static images [8, 190–192] and video [6, 35, 193–195]. The standard procedure for evaluating these methods is to train and test a pose detector on different splits of the same data set, which implies that both sets are from the same domain. The pose detectors trained based on this standard procedure face one big problem. If the detectors were to be applied to a new (surveillance) video data set, there is highly likely to be domain difference between the training set and the new video data set, thus leading to degradation in pose detection performance. An example is shown in Figure 5.1, which shows that the appearance, configuration and viewing angle of poses are different for each data set.

A straightforward method to overcome this domain difference is to manually label training data for each new domain. However, manually labeling each new domain may be too tedious to perform. Therefore, we propose to utilize constrained self-training to automatically harvest in-domain training data directly from unlabeled surveillance videos. The collected in-domain training data is then combined with the existing out-of-domain training data to build a more effective pose estimator for the new domain.

(A) Snapshot of training data from PARSE (top row) and LEEDS sports (bottom row).

(B) Snapshots of people from Caremedia data set.

FIGURE 5.1: Snapshots of pose detection targets from different data sets.

Starting from a static image-based pose detector, we propose to perform constrained self-training to gradually adapt the pose detector to video data. Self-training [32, 33] is the iterative process of adding testing instances with highly confident predictions into the training set to enhance the current model. However, as highly confident instances may not always be correct, we constrain the self-training process by only selecting highly confident poses which follow the internal spatial-temporal smoothness constraints. The assumption is that pose estimation results in neighboring frames should not vary too much. If the estimated poses for two neighboring frames vary greatly, then it is highly likely that one of the detected poses is incorrect despite the fact that they both may have high confidence scores. In this case, we will ignore these two pairs of frames. The advantage of our method is that since it is fully unsupervised, it has the ability to harvest training examples from large amounts of unlabeled in-domain testing videos. Therefore, we can afford to be very conservative and only select instances in which we are very confident, i.e. it is acceptable if we throw away 99.99% of the data as long as if we still have a 0.01% harvest rate on a very large unlabeled set.

We emphasize that our main goal is not to utilize the spatial-temporal smoothness constraint to enhance pose estimation in video, but to utilize this constraint as a *consistency check* for better self-training of pose estimation models, which leads to better domain adaptation from images to video. Our method has a different motivation and method of utilizing the spatial-temporal smoothness constraints for video pose estimation compared to [6, 194], which directly learns a video-based pose detector. Video-based pose detectors utilize spatial-temporal smoothness constraints themselves to acquire a pose detection result, so utilizing the same constraint to verify whether a pose detection is correct or not is unreasonable.

The advantage of our algorithm is two folds. First, our method is not constrained to a specific pose estimation model. Any method which outputs a confidence score corresponding to the detected pose can be used. Second, our method is fully automatic, thus it has the potential to adapt to large varieties of video domains without any supervision. In sum, our contributions are as follows:

1. We propose to automatically adapt image pose detectors to video based on constrained self-training, which utilizes the spatial-temporal smoothness constraint.
2. Experiments performed on the Caremedia video data set with two pose detectors: [8, 190] demonstrates the effectiveness of our method.

5.1 Related Work - Pose Estimation

Pose estimation in images [190–192] and video [6, 35, 193–195] has been intensively studied but still remains to be a challenging topic.

One main challenge of pose estimation is developing effective and efficient models to parse human joints. As human limbs form a tree structure, tree-structured models (also called pictorial structures) [6, 190, 196] have been widely used for pose estimation as they are computationally efficient and effective. However, as these models do not take into account the relation between the two hands and legs, double counting is a big problem, e.g. the pose estimation prediction associates both the left and right hand to the same physical hand. Self-occlusion is also a big problem, as different parts may articulate and occlude other parts. To model the interacting joints, many loopy graph-based models have been introduced [193, 197, 198], but these models are usually harder to optimize and significantly more time consuming to run. [192] replaced the loops in the graph by introducing multiple layers of simple classifiers, i.e. a sequential prediction model, which leads to the efficient and effective pose machine algorithm. Many video-based pose estimation algorithms have also been proposed [6, 193–195], but they also face the same trade-off of faster but coarser tree-models versus slower but more fine-grained graph models. Furthermore, video-based methods are more difficult to train because the annotation of video training data is required, which is significantly more tedious than annotating a single image.

In the advent of deep learning, multiple deep convolutional pose estimators were proposed. In terms of how the output and loss of the deep network were formulated, there are roughly two families. One kind of network directly outputs the (x, y) Cartesian coordinates of each body joint [182, 199], i.e. the network directly regresses over the coordinates and the network is optimized with the Euclidean loss between the predicted

and ground-truth locations. The second kind of network outputs a heat-map to the locations of each joint [8, 200], and the network is optimized by minimizing the Euclidean loss between the predicted and ground-truth heat-maps. The main advantage of utilizing the heat-map is that uncertainties in joint locations are preserved, whereas only outputting the (x, y) locations provide no information in terms of confidence. Therefore, when the entire heat-map is fed into the next model in a sequential prediction framework, the next model can utilize the uncertainties to generate better pose estimation predictions [8].

On the other hand, regardless of how the loss of a deep pose estimator was formulated, both [199] and [8] were formulated under the sequential prediction model. [199] iteratively predicted the necessary offset required to move the current joint prediction to the correct pose location. [8] had multiple stages where each stage outputs a heat-map for each joint. The heat-map from the previous stage was taken as input and refined by the next stage. More details of [8] are in Section 5.3.

Another main challenge of pose estimation comes from the large configuration of possible human poses, which is difficult enumerate even with the large data sets currently available. Current popular pose estimation data sets include PARSE [201] with 305 annotated full-body poses, BUFFY [202] with 748 upper body poses, VideoPose2.0 [6] with 1286 upper body frames, FLIC [191] with 5K upper body frames, extended LEEDS Sports [203] with 12K poses, and MPII human pose dataset [204] with 40K poses. Even though coverage increases as the data sets become larger, but as the coverage of these data sets are still not perfect, in-domain data will still be very useful in enhancing pose estimation. This motivates us to utilize constraint self-training to automatically adapt an image-based pose detector to any video data set.

Finally, our work can be viewed as an extension to the classic pose detector [196]. [196] proposed to track each limb of a person by first finding highly confident pose detections of the person using a pre-trained lateral person pose detector and then directly learning an appearance model for each limb of the person, thus involving two models. In our work, we merge these two models by updating the pose detector directly based on the highly confident pose detections. Also, our work utilizes spatial-temporal constraints to select highly confident poses, which was not used in [196].

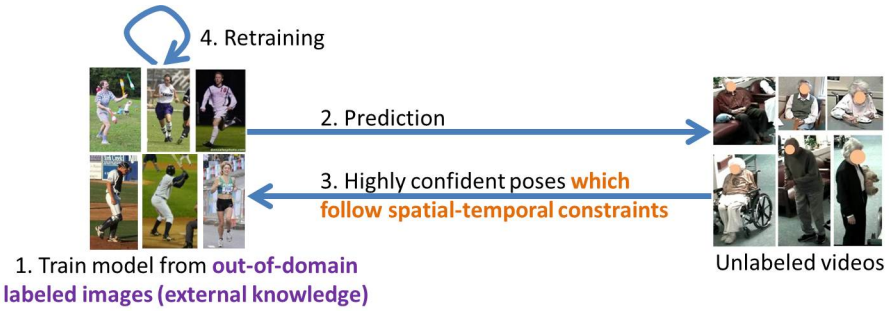

FIGURE 5.2: Illustration of constrained self-training.

5.2 Constrained Self-Training for Unsupervised Domain Adaptation

We propose to automatically adapt image-based detectors to video based on constrained self-training (CST). As shown in Figure 5.2, the inputs to our algorithm are out-of-domain training images and videos on which we would like to perform pose estimation. The output will be a pose estimator adapted to the video domain at hand. The main steps of our method are as follows:

1. Train a pose detector on out-of-domain labeled images, which can be viewed as external knowledge.
2. Perform pose estimation on unlabeled input videos with the current model.
3. Harvest pseudo-training data by selecting predicted poses that not only have high confidence but also violate the continuity and tracking constraints the least.
4. Update/retrain pose estimation model based on newly selected data. Go to step 2 till maximum iterations reached.

The continuity and tracking constraints, which both stem from the spatial-temporal smoothness constraints, are the key to preventing the self-training procedure from utilizing incorrect pose estimation examples for training. In the following sections, we will describe the two constraints in detail.

5.2.1 Continuity Constraint

The continuity constraint captures the fact that limbs should not move too far in a short period of time. Therefore, based on the body part location predictions of each frame, we compute the smoothed trajectories for each body part. Let P be the number of body parts, and F be the total number of frames in a video. Let p_i^f, $1 \leq i \leq P$, $1 \leq f \leq F$ be the location of part i detected by the pose detector in frame f. Let $\widetilde{p}_i^f$ be the location of the body parts for the smoothed trajectories. We find the smoothed trajectories by

minimizing the following equation.

$$\min_{\widetilde{p}_i^f|_{i=1}^P|_{f=1}^F} \sum_{f=1}^{F}\sum_{i=1}^{P}\left(\left\|\widetilde{p}_i^f - p_i^f\right\|_2^2 + \alpha\left\|\widetilde{p}_i^{f+1} - \widetilde{p}_i^f\right\|_2^2\right). \tag{5.1}$$

The first term makes sure the smoothed trajectory is consistent with the detections. The second term minimizes the distance between detections in adjacent frames, which forces the trajectory to be smooth. α controls the relative weight between these two terms.

5.2.2 Tracking Constraint

The tracking constraint assumes that the body parts in different frames should be consistent with local optical flow based tracking results. The tracking procedure is performed as follows. For each pose estimation in each frame, we track each body part for 1 second. Each body part is tracked with dense trajectories [205] based on the KLT tracker [206]. Dense trajectory keypoints are extracted from the bounding box of the body part and tracked. As the body parts are tracked for 1 second, we can compute a location hypothesis for the tracked body part for each frame in the 1-second window. The body part location hypothesis for a frame is the average location of the tracked keypoints in that frame.

For a body part in a single frame, it will have multiple location hypotheses from neighboring frames. We merge these location hypotheses to compute the most likely location of the body part by performing a weighted sum over all the location hypotheses. The weight of each location hypothesis corresponds to the detection confidence of the detected pose which provided the specific hypothesis. Let the results of the weighted sum be T_i^f. We update Equation 5.1 such that the smoothed trajectories also need to be close to the tracking hypotheses.

$$\min_{\widetilde{p}_i^f|_{i=1}^P|_{f=1}^F} \sum_{f=1}^{F}\sum_{i=1}^{P}\left(\left\|\widetilde{p}_i^f - p_i^f\right\|_2^2 + \alpha\left\|\widetilde{p}_i^{f+1} - \widetilde{p}_i^f\right\|_2^2 + \beta\left\|\widetilde{p}_i^f - T_i^f\right\|_2^2\right). \tag{5.2}$$

β controls the relative weighting of the tracking constraint.

5.2.3 Selecting Positive Examples

We now utilize the continuity and tracking constraint to add pose detections which are highly likely to be correct into the self-training process. Once we have computed $\widetilde{p}_i^f$ by solving Equation 5.2, we can compute the pose detections which are not only confidently

detected by the pose detector, but also violate the constraints the least. Let c^f be the confidence of the pose detection in frame f. Let s^f denote the negated error of the two constraints:

$$s^f = -\sum_{i=1}^{P} \left(\left\| \widetilde{p}_i^f - p_i^f \right\|_2^2 + \alpha \left\| \widetilde{p}_i^{f+1} - \widetilde{p}_i^f \right\|_2^2 + \beta \left\| \widetilde{p}_i^f - T_i^f \right\|_2^2 \right). \tag{5.3}$$

Then we select potential training data by looking for pose estimations which have c^f and s^f higher than a threshold. Once we have selected a few positive testing instances, we add the testing data into the training data and reiterate through this process.

The CST training data collection process does not guarantee that the collected instances are correct. Through the constraints, we are only able to collect training instances which were very "stable" in the adjacent frames. However, the stability of the labeling is not equivalent to the correct labeling, and in our experiments, we show how the labeling errors actually affect CST performance.

5.3 Experiments

We evaluated our constrained self-training pose estimation approach with the following setup.

Pose Estimators: To demonstrate that our method is agnostic to the pose estimator used, we performed pose estimation experiments with the Flexible Mixture-of-Parts (FMP, [190]) and Convolutional Pose Machines (CPM, [8]).

FMP utilizes a tree structure to model a person, and each body part is represented by a mixture of configurations. HOG [132] was used as the low-level feature. The code was acquired directly from the authors [190], and the optimal parameters: 26 joints and 6 clusters were used to train FMP. There is no clear way to fine-tune FMP with the newly harvested in-domain pseudo-training samples, so a new model was retrained whenever a new set of training instances were provided.

CPM is a deep pose estimator with multiple stages as shown in Figure 5.3. There are two main parts: the low-level network and the high-level network. The low-level network consists of 4 convolutional layers with filter size $5 \times 5 \times 128$ for all layers and max-pooling in the first three layers which reduce the size of the original image by a factor of 8. This captures the lower level details of the image. Then the high-level network will take as input the output of the low-level network and the output of the previous high-level network. For the first high-level network, there are 3 convolutional layers with filter size $9 \times 9 \times 512$, $1 \times 1 \times 512$ and $1 \times 1 \times 15$. For the other high-level

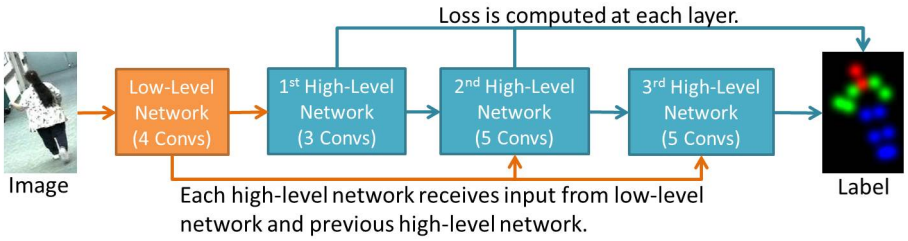

FIGURE 5.3: Illustration of the CPM pose estimator with 3 high-level network stages.

networks, there are 5 convolutional layers with filter size $9 \times 9 \times 64$, $9 \times 9 \times 64$, $9 \times 9 \times 128$, $1 \times 1 \times 128$ and $1 \times 1 \times 15$. All outputs of the high-level network are connected to a Euclidean loss of the ground-truth heat-map. The advantage of the multi-layer design is that double counting can be alleviated. For example, if the left and right wrists were all predicted on the same physical wrist at stage $s-1$, then stage s has the ability to learn to change the location of one of the wrists to the other physical wrist. In our experiments, there were 3 high-level networks. The CPM implementation[1] was based on Caffe [187]. If a CPM was trained from scratch, the base learning rate was 2×10^{-5}, and the learning rate was divided by 3 every 66,000 iterations. Batch size was set to 12. For fine-tuning, the base learning rate was 5×10^{-6}, and the number of iterations utilized was 2.5 $\times$ number of fine-tuning instances. In the prediction phase, the locations with the highest scores were selected as the locations of each body part, and the confidence of the pose was computed by averaging the highest scores of each body part.

Data Sets: The FMP pose estimators were trained on PARSE [201], which had 305 full-body poses, and the negative set was from the INRIA Person database. Data augmentation was performed by mirroring and rotating the images by -15, -7.5, 7, 7.5 degrees. One limitation of FMP is that the method assumes all joints are visible, thus when training over the Caremedia pose data set, only the poses where all joints were visible were used.

The CPM pose estimators were trained on LEEDS Sports [203, 207]. There were 11K training images, and each image was resized to 304-by-304. Data augmentation was performed by mirroring and rotating the images from -150 to 180 degrees in 30-degree intervals. 213,000 iterations were run to train the CPM network on LEEDS Sports.

The target domain for domain adaptation was the Caremedia data set, where 3,193 poses were annotated. 14 joints were annotated if the joints were visible. Some examples are shown in Figure 5.4. To compare the effectiveness of our self-training method, we also evaluated the performance of models which used in-domain ground-truth instances for fine-tuning. To perform fine-tuning experiments, the Caremedia data set was split

[1] Code modified from Shih-En Wei's implementation of CPM.

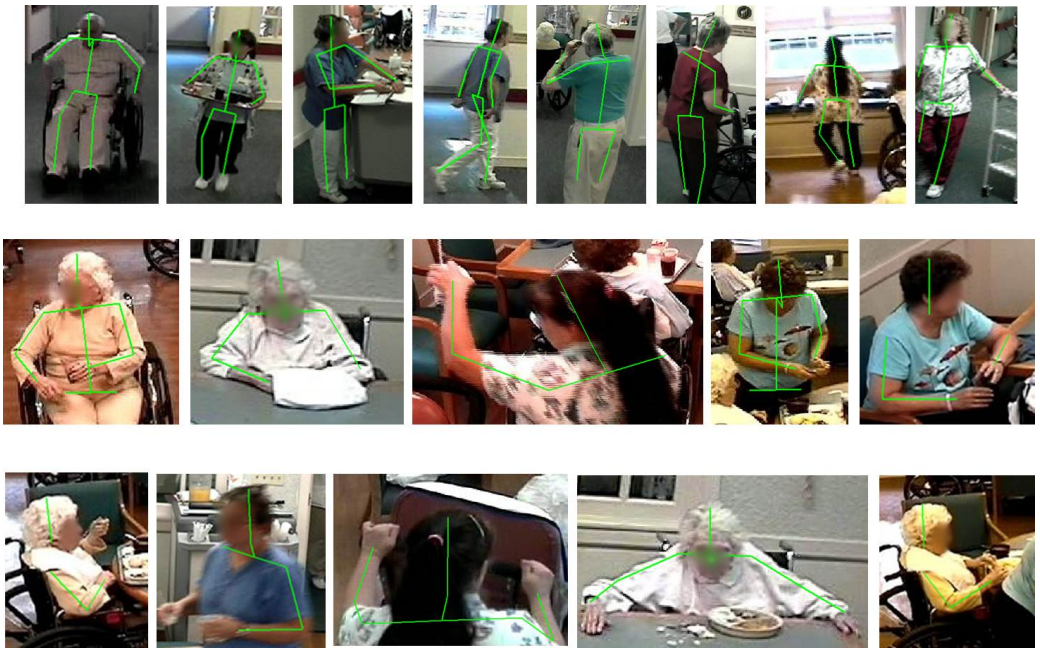

FIGURE 5.4: Annotated poses from the Caremedia data set.

into two folds, where one fold was used for fine-tuning and the other fold was used for testing. The prediction results from the two folds were combined and an overall score was computed. The folds were split so that ground-truth instances of a single individual would all be in the same fold. This was to prevent the pose estimator from "memorizing" a single individual. Data augmentation was performed by mirroring and rotating the images by -15, -7.5, 7.5 and 15 degrees. Also, to understand the effect of training data size versus pose estimation performance, we randomly sampled from the training fold 50, 200, 584 and 800 instances 5 times each and utilized each sampled training set to fine-tuning the CPM. For FMP, we sampled 50 and 227 instances per fold.

Parameters: The self-training methods were presented 10-second video clips which encompassed each of the 3,193 annotated poses. For each video clip, at most one pose estimation which had a score larger than the threshold was selected. For FMP, the minimum confidence thresholds used for self-training was $c^f \in \{0.9, 1.0\}$ and CST was $c^f \in \{0.4, 0.5\}$, $s^f \in \{-600, -1000\}$. For CPM, the minimum confidence thresholds used for self-training was $c^f \in \{0.5, 0.6, 0.7\}$ and CST was $c^f \in \{0.5, 0.6, 0.7\}$, $s^f = -350$. We ran the self-training for one iteration. Internal tests have shown that running on one iteration already saturates performance, which we believe was due to our unlabeled set not being big enough. We set $\alpha = 5$ and $\beta = 0$ in our experiments. $\beta = 0$ because we found in our preliminary experiments that KLT keypoint tracking cannot find many keypoints to track in low-resolution Caremedia video, which leads to severe body-part tracking error. Therefore, the tracking continuity term was not utilized in our experiments. This issue could be alleviated by utilizing a patch-based tracker instead of a

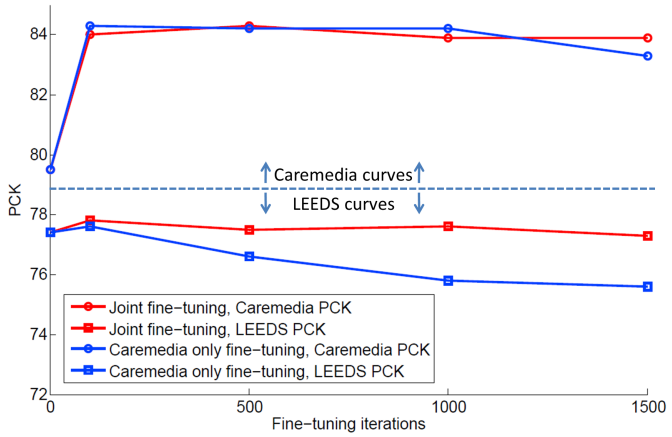

FIGURE 5.5: Performance of LEEDS and Caremedia with joint fine-tuning and Caremedia only fine-tuning.

keypoint-based tracker.

Evaluation Metrics: We utilized the widely used Percent of Correct Keypoints (PCK, specifically PCK@0.2) [191] as our evaluation metric. For PCK@0.2, a keypoint is counted as correct if the distance between the keypoint and the ground-truth is less than $0.2 \times d$, where d is the diameter of the torso, i.e. distance between the left hip and the right shoulder. In this way, the accuracy for each of the 14 keypoints can be computed.

Results and Discussion

Before performing large numbers of fine-tuning experiments, we first tested two different fine-tuning methods for CPMs: fine-tuning only with Caremedia training data, and joint fine-tuning with both Caremedia and LEEDS training data. One hypothesis is that joint fine-tuning with both Caremedia and LEEDS training data can improve Caremedia performance. Joint fine-tuning is performed by providing 12 (which is the batch size) training instances from both data sets to the network per iteration. We ran fine-tuning with both fine-tuning methods on the training samples collected by CST when $c^f = 0.6$ and $s^f = -350$. Then, for different iterations, we predicted the fine-tuned model on both LEEDS and Caremedia. Results are shown in Figure 5.5, which show that when fine-tuning only with Caremedia samples, performance on LEEDS drops. With joint fine-tuning, performance of LEEDS stays the same. However, there is no clear difference in performance between the two methods for the Caremedia data set. This shows that both fine-tuning methods are effective, and for simplicity, we utilized Caremedia only fine-tuning for our remaining experiments.

Method	PCK	In-domain (psuedo-)training instances
PARSE	64.6	0
CST, $c^f = 0.5$, $s^f = -600$	67.6	196
CST, $c^f = 0.4$, $s^f = -1000$	69.1	347
Self-training, $c^f = 1.2$	66.6	208
Self-training, $c^f = 1.0$	67.5	340
Self-training, $c^f = 0.9$	67.5	435
50 fine-tuning instances	68.5	50
227 fine-tuning instances	70.6	227

TABLE 5.1: PCK performance for self-training, CST and fine-tuning based on the FMP model trained on PARSE.

The performance of CST to adapt an image-based detector trained on PARSE or LEEDS Sports to Caremedia is summarized in Table 5.1 and Table 5.2 respectively. As the CPM is the state-of-the-art pose detector, a more detailed analysis of the CPM trained with different numbers of LEEDS Sports training examples are shown in Figure 5.6a.

From Figure 5.6a we can see that a LEEDS Sports model trained with 2,000 instances and enhanced with CST performed as well as a LEEDS Sports model with 11,000 instances. This shows that CST was equivalent to 9,000 out-of-domain instances, thus demonstrating the importance of acquiring in-domain data.

We can see that both self-training and CST were effective in enhancing both FMP and CPM pose estimators. For FMP, CST performed slightly better than self-training. However, there is no clear difference between the performance of self-training and CST for CPMs. This may be because a very conservative self-training c^f threshold collects around the same quality of training examples as CST. Though CST can afford a lower c^f threshold, it would end up only harvesting the same number of training examples because many examples were filtered out by the smoothness threshold s^f. This shows that the spatial-temporal smoothness constraint was not very cost-effective, and it was the external knowledge acquired from out-of-domain training data which provided most of the performance gain.

Compared with the fine-tuning scenario, CST was equivalent to around 50 manually collected in-domain training examples, which takes around 1 hour of manual human effort to acquire. Also, in general, the margin of improvement of both CST and fine-tuning decreased as more out-of-domain training samples were used for training.

Digging deeper into the figures, we can see clearly from Figure 5.6b that the quality of training instances collected manually versus through CST was different. For example, with 584 manually collected training instances, the PCK was 88.5, whereas for CST it was only 84.2. There are 3 possible reasons for this gap: 1) the automatically collected

Method	PCK	In-domain (psuedo-)training instances
LEEDS Sports 11K	79.5	0
CST, $c^f = 0.7$, $s^f = -350$	82.8	189
CST, $c^f = 0.6$, $s^f = -350$	84.2	584
CST, $c^f = 0.5$, $s^f = -350$	84.2	1220
CST, $c^f = 0.4$, $s^f = -350$	81.7	1708
Self-training, $c^f = 0.7$	84.5	675
Self-training, $c^f = 0.6$	83.9	1695
Self-training, $c^f = 0.5$	84.5	2592
50 fine-tuning instances	85.8	50
200 fine-tuning instances	87.4	200
584 fine-tuning instances	88.5	584
800 fine-tuning instances	89.8	800
1600 fine-tuning instances	90.5	1600

TABLE 5.2: PCK performance for self-training, CST and fine-tuning based on the CPM model trained on LEEDS Sports 11K.

training instances were inaccurate, 2) the collected instances were biased to a specific set and lacked variety, and 3) the collected instances were too easy thus not informative to the classifier. In order to understand the reason for this gap in performance, we manually corrected all the 584 pose estimation results collected by CST when $c^f = 0.6$ and $s^f = -350$. Then we utilized these manually corrected instances to fine-tune the CPM, and results are shown in Figure 5.7a. Results show that our CST actually achieved the same level of performance as "manually corrected CST" and "584 randomly sampled fine-tuning instances" for the upper body, which includes the head, shoulder, elbow and wrist. However, CST performed significantly worse on the hip, knee and ankles. Digging deeper into why CST was not as helpful on the hip, knee and ankle, we found that the labeling accuracy of these joints by CST was significantly lower than the other joints as shown in Figure 5.7b. There is a very clear positive correlation between the body joint labeling accuracy of CST versus the relative PCK performance of CST when compared to the "manually corrected CST" run. We believe this can largely explain the performance gap between CST and fine-tuning with manually labeled samples. This leads us to conclude that: 1) the collected instance were not too easy for the classifier because we see as much gain in performance on the upper body joints, 2) the collected instances have just as much variety as the randomly sampled manual instances, because the average PCK of the "manually corrected CST" and "584 randomly sampled fine-tuning instances" runs have similar performance, and 3) the accuracy of the automatically labeled instances played a key role in affecting CST performance.

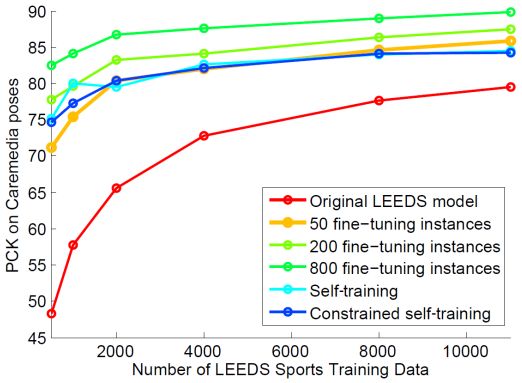

(A) PCK performance of self-training and "fine-tuning with manually labeled instances" when utilizing different numbers of out-of-domain LEEDS Sports training examples.

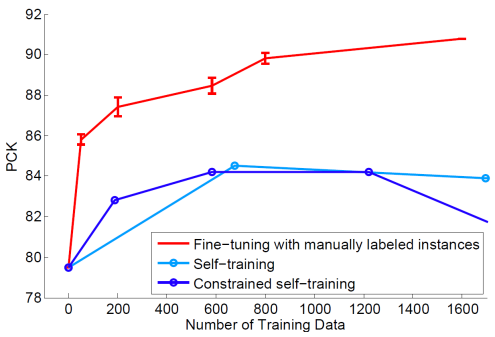

(B) Results of self-training and fine-tuning with 11,000 out-of-domain training examples. The 95% confidence interval is shown for the "fine-tuning with manually labeled instances".

FIGURE 5.6: Results of self-training compared to "fine-tuning on manually labeled instances" with the CPM model.

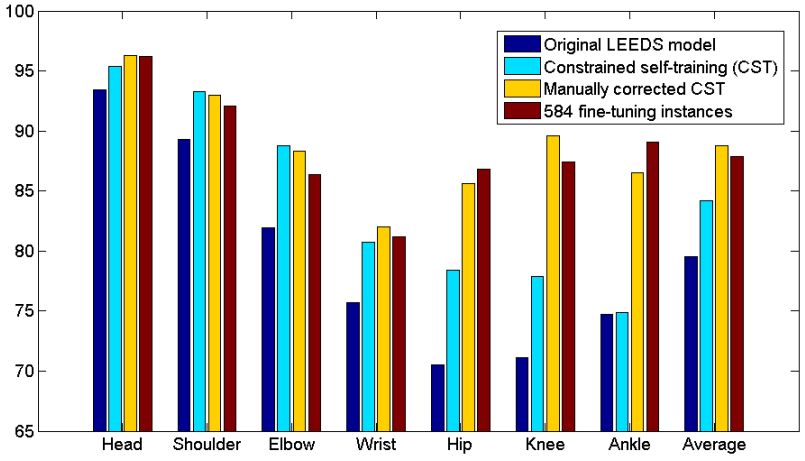

(A) PCK performance for different body parts under different conditions.

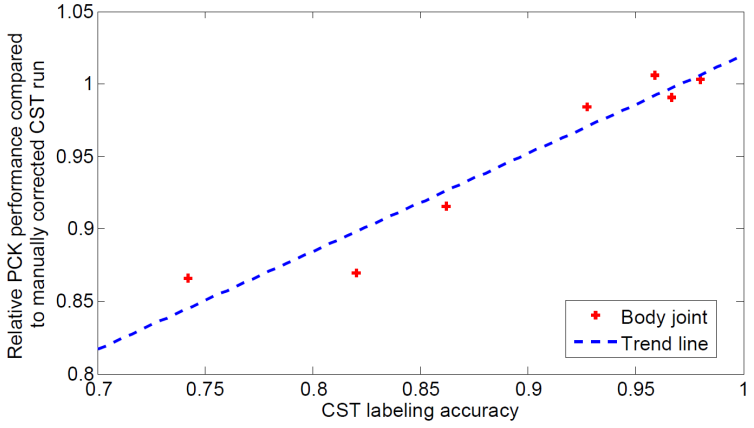

(B) The relation between CST labeling accuracy and PCK performance relative to the manually corrected CST run with the CPM model.

FIGURE 5.7: Analysis of CST performance drop.

FIGURE 5.8: Examples of pose estimation errors which were fixed through CST. Green and red lines correspond to the correct and incorrect limbs respectively. The image connected by a dotted line are training examples harvested from CST.

FIGURE 5.9: Pose estimation failure cases. Green and red lines correspond to the correct and incorrect limbs respectively.

Qualitative analysis of CST pose estimation was also performed. As CST directly harvests training examples from the testing data, CST can potentially "memorize" a person, thus enhancing the pose estimation performance for that specific person. Figure 5.8 shows the poses which were incorrectly predicted by the out-of-domain model but correctly predicted by the CST model. A CST collected instance which could have likely helped in correcting this pose is also shown. Examples of pose estimation failure cases are shown in Figure 5.9. Failure cases include double counting for the first three images, confusing hairstyles for the second image, and challenging upper-body poses with occlusions and another person.

5.4 Summary

We present constrained self-training, which utilizes the spatial-temporal smoothness constraint to adapt a static image-trained pose detectors to video data. The key advantage of our method is that the whole process is unsupervised, thus enabling us to potentially generalize to a large variety of video. Experiments showed that CST was effective in adapting two image pose detectors: FMP and CPM to the Caremedia video domain in

an unsupervised fashion, thus supporting that CST is agnostic to the pose detector used. For CPM, a pose estimator trained on 2,000 out-of-domain training examples combined with CST achieved equivalent performance to a model trained with 9,000 more (total of 11,000) out-of-domain training examples. Also, the effect of CST was equivalent to around 50 manually labeled in-domain instances, thus saving around 1 hour of manual effort. Detailed analysis of the training samples collected by CST showed that the samples collected were actually diverse and not simply focused on the easy instances. Also, for the upper body joints, the performance of models fine-tuned with CST collected instances achieved as good a performance compared to models fine-tuned on manually collected instances. However, CST labeling errors on the lower body heavily affected the pose estimation performance on the corresponding joints, which was the main cause of CST not performing as well as fine-tuning on manually collected instances. Another negative outcome is that self-training and CST performed very similarly, thus showing that the spatial-temporal smoothness constraint may not be very cost-effective in collecting accurate training examples. This shows that not all external knowledge or internal constraints are useful.

A future work is to apply CST to very large amounts and large varieties of video to automatically collect training data to improve a generic pose estimator. This process could be run iteratively to potentially perform never-ending pose estimation learning. However, the biggest bottleneck in our experiments was the speed of pose estimation on videos, which was the limiting factor for the number of videos used in our CST experiments. Therefore, developing efficient pose estimators for video will potentially enable us to unleash the full power of CST.

Chapter 6

Long-Term Surveillance Video Analysis

According to reports[1], there were 245 million surveillance cameras operating in 2014. This means that every hour, 245 million hours of surveillance video are generated. Though many surveillance cameras have lower frame-rates which will slightly alleviate the amount of data to be analyzed, the amount of data generated is still too much to analyze manually. Therefore, we demonstrate in this chapter two applications of automated long-term surveillance video analysis based on the identity-aware multi-object tracker and pose detector we developed. The first use case is video summarization and long-term statistics computation based on tracking output. The second use case is eating detection based on pose estimation.

6.1 Visual Diary Generation with Multi-Person Tracking

To demonstrate the usefulness of our tracking output, video summarization experiments were performed. We propose to summarize surveillance video using visual diaries, specifically in the context of monitoring elderly residents in a nursing home. Automatic visual diary generation for elderly nursing home residents enables doctors and staff to quickly understand the activities of a senior person throughout a day to facilitate the diagnosis of the elderly person's state of health. The visual diary for a specific person consists of two parts: 1) snippets which contain snapshots and textual descriptions of activities-of-interest performed by the person, and 2) activity-related statistics accumulated over time. The textual descriptions of the detected events enable efficient indexing of what a

[1] https://technology.ihs.com/532501/245-million-video-surveillance-cameras-installed-globally-in-2014

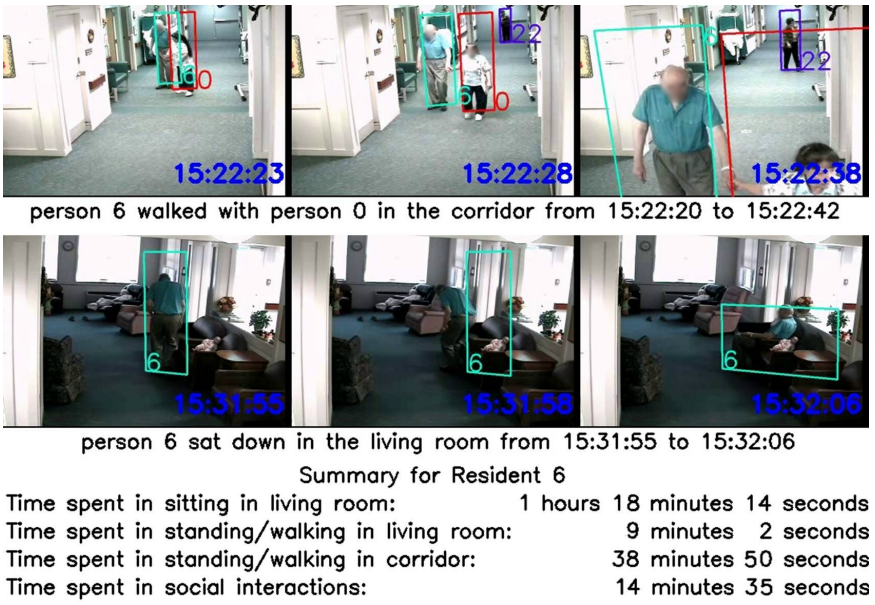

FIGURE 6.1: The visual diary for elderly resident 6 in a nursing home. The automatically generated textual description and 3 snapshots are shown for the two events. Long-term statistics are also shown.

person did at different times. The statistics for the activities detected can be accumulated over many days to discover long-term patterns. An example is shown in Figure 6.1, where the visual diary of a nursing home resident is shown.

We propose to generate visual diaries with a summarization-by-tracking framework. Using the trajectories acquired from our tracking algorithm, we extract motion patterns from the trajectories to detect certain activities performed by each person in the scene. The motion patterns are defined in a simple rule-based manner. Even though more complex methods such as variants of Hidden Markov Models [208] to detect interactions could also be used, this is not the main focus of our work. Also, our experiments show that with the rules we have defined, reasonable interaction detection performance was achieved. The activities we detect are as follows:

- Room change: Given the tracking output, we can detect when someone enters or leaves a room.
- Sit down / stand up: We trained a sitting detector [171] which detects whether someone is sitting. Our algorithm looks for tracks which end/begin near a seat and check if someone sat down/stood up at around the same time.
- Static interaction: if two people stand closer than distance D' for duration T', then it is likely that they are interacting.
- Dynamic interaction: if two people are moving with distance less than D' apart for a duration longer than T', and if they are moving faster than 20 cm/s, then it is highly likely that they are walking together.

According to [209], if people are travelling in a group, then they should be at most 7 feet apart. Therefore, we set the maximum distance D' between two people for there to be interaction to 7 feet. The minimum duration of interaction T' was set to 8 seconds in our experiments.

Given the time and location of all the detected activities, we can sort the activities according to time and generate the visual diary. The visual diary for a given individual consists of the following:

- Snippets: snapshots and textual descriptions of the activity. Snapshots are extracted from video frames during the interaction and textual descriptions are generated using natural language templates.
- Room/state timing estimates: time spent sitting or standing/walking in each room.
- Total interaction time: time spent in social interactions.
- Interacted targets: people with whom the person interacted.

Our proposed method of using tracking output for activity detection can be easily combined with traditional activity recognition techniques using low-level features such as Improved Dense Trajectories [210] with Fisher Vectors [211] to achieve better activity detection performance and detect more complex actions, but extending activity recognition to activity detection is out of the scope of this work.

6.1.1 Visual Diary Generation Results

We performed long-term surveillance video summarization experiments by generating visual diaries for the *Caremedia 8h* sequence based on trajectories acquired with our Solution Path Algorithm tracker and deep appearance features. To acquire ground truth for activity detection experiments, we manually labeled the activities of 3 residents throughout the sequence. The 3 nursing home residents were selected because they are the people who we would like to focus on for the automatic analysis of health status.

We evaluated the different aspects of the visual diary, including "room/state timing estimates", "interaction timing estimates", "interacted target prediction" and "snippet generation".

The evaluation of "room/state timing estimates", i.e. predicted room location and state (sitting or upright), of a person was done on the video frame level. A frame was counted as true positive if the predicted state for a given video frame agreed with the ground truth. False positives and false negatives were computed similarly.

To evaluate "interaction timing estimates", i.e. how much time a person spent in interactions, a frame was only counted as true positive if both the predicted results and

Visual diary components	Micro-Precision	Micro-Recall	Micro-F1
Snippet generation	0.382	0.522	0.441
Room/state timing estimates	0.809	0.511	0.626
Interaction timing estimates	0.285	0.341	0.311
Interacting target prediction	0.533	0.762	0.627

TABLE 6.1: Evaluation of the generated visual diary.

Patient	Time spent in ...					# interacted people
	sit in living room	stand/walk in living room	stand/walk in corridor	stand/walk in dining room	social interaction	
Patient 3	00:26:28	00:19:05	01:09:45	00:00:36	00:15:40	11
Patient 6	01:18:14	00:09:02	00:38:50	00:02:06	00:14:35	10
Patient 11	00:20:10	00:01:25	00:23:17	00:00:39	00:07:33	9

TABLE 6.2: Summary of important statistics for 3 nursing home residents in video with 7 hours 45 minutes wall time. Timing is formatted as hh:mm:ss. For example, patient 6 spent 1 hours 18 minutes and 14 seconds sitting in the living room.

ground truth results agreed that there was interaction and also the ID of the interacted targets matched. False positives and false negatives were computed similarly. For "interacted target prediction", i.e. who interacted with whom, a true positive was counted when the predicted and ground truth output both agreed that the resident interacted with a given person. False positives and false negatives were computed similarly.

The evaluation of "snippet generation" accuracy was done as follows. For snippet related to sit down, stand up and room change activities, a snippet was correct if the predicted result and ground truth result had less than 5 second time difference. For social interaction related snippets, a snippet was correct if 50% of the predicted snippet contained a matching ground-truth interaction. Also, if a ground-truth interaction was predicted as three separate interactions, then only one interaction would be counted as true positive while the other two would be counted as false positives. This prevented double counting of a single ground-truth interaction.

Based on the tracking output, we performed activity detection and visual diary generation on the three residents. 184 ground-truth snippets were annotated. The performance of visual diary generation is summarized in Table 6.1. From the table, 38% of the generated snippets were correct, and we have successfully retrieved 52% of the activities-of-interest. For "room/state timing estimates", a 51.1% recall shows that we know the state and room location of a person more than 50% of the time. The lower performance for "interaction timing estimates" is mainly caused by tracking failures, as both persons need to be tracked correctly for interactions to be correctly detected and timings to be accurate. However, if we only want to know the interaction targets, we still can achieve 63% F1-score. These numbers are not high, but given that our method

is fully automatic other than the collection of the face gallery, this is already a good first cut at generating visual diaries for the elderly.

As our visual diary generation is heavily based on tracking, we analyzed the effect of tracking performance on visual diary generation accuracy. We computed the snippet generation F1-score for multiple tracking runs with varying tracking performance. These runs include our baseline runs and also runs where we randomly corrupted face recognition labels to decrease tracking performance. Results are shown in Figure 6.3, which shows that as tracking performance increases, snippet generation F1 also increases with a trend which could be fitted by a second-order polynomial.

Figure 6.1 and Figure 6.2 show example visual diary snippets for the three residents. From the generated snippets, we can clearly see what each resident was doing at each time of the day. Long term statistics were also compiled as shown in Table 6.2, which clearly shows the amount of time spent by each person in each room and in social interactions.

6.1.2 Long-term (23 Day) Statistics

We also showed how the visual diary could be extended to utilize statistics over 23 days. The amount of time interacting with each person, the amount of time spent in interactions each day and the distanced walked every day were automatically computed and aggregated into a single report as shown in Figure 6.4. Based on our manual observation, ID 34 is resident 11's partner, which is reflected in our pie chart as ID 34 is ranked second in all the people with whom resident 11 interacts. These long-term statistics, which are too tedious to collect manually, have the potential to aid doctors and staff in assessing the health status of nursing home residents. Though there is not a very clear trend in Figure 6.4 for interaction timing and walking distance, we believe this is mainly due to our observation being limited to 23 days. If our analysis was performed over a period of half a year or a whole year, then it is likely some hidden trends will be visible from the automatically computed statistics.

6.2 Eating Detection with Pose Estimation

We explore the usefulness of our pose estimator for eating detection. As a proof-of-concept, our main goal is to automatically detect when a person "takes a bite", which could be useful in the analysis of eating speed and eating behavior. We propose to utilize the distance between the resident's wrist and his/her head to detect whether the person took a bite.

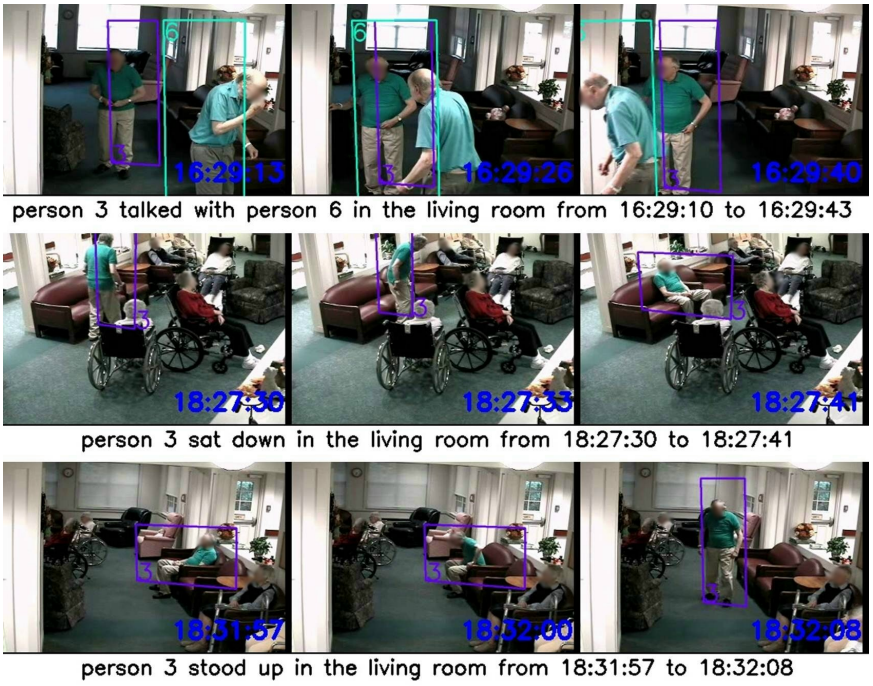

(A) Selected snippets for resident 3.

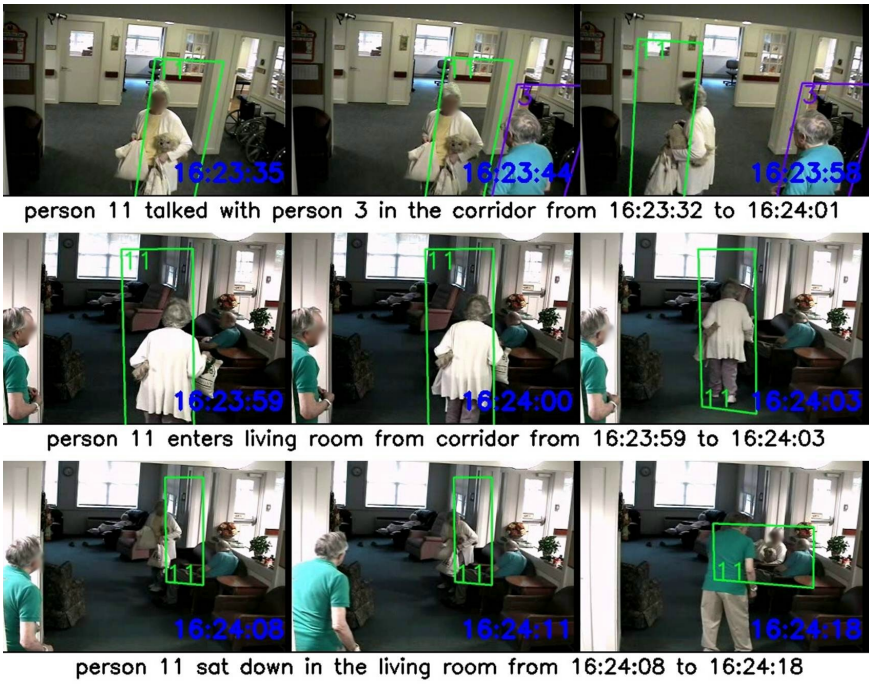

(B) Selected snippets for resident 11.

FIGURE 6.2: Selected visual diary snippets for each resident.

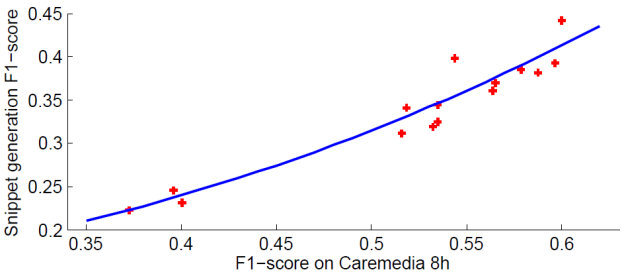

FIGURE 6.3: Performance of snippet generation under varying tracking performance.

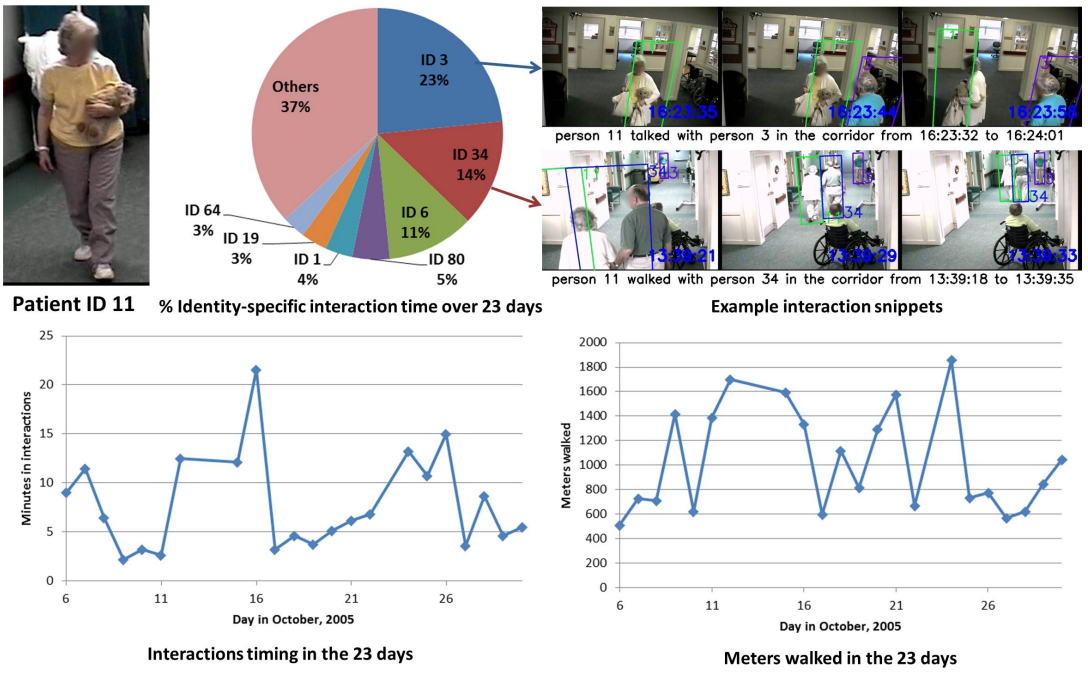

FIGURE 6.4: Long-term statistics report for resident 11. The total amount of time spent interacting with each person, the amount of time spent interacting each day and the total distance walked are shown. Visual diary snippets corresponding to the interaction targets are also shown.

3 residents were selected and for each resident, we annotated 15 minutes of eating footage for 7 out of the 23 days, thus leading to 105 minutes of footage per person. We manually selected the 15 minutes of video which contains footage of the resident of interest eating. The annotation protocol was that whenever a person touches his/her head with a spoon, fork, cup, hand or napkin, then it is a true positive.

The pose estimator was applied on all frames of the video. To make our computation faster, we manually cropped the bounding box to indicate the region of interest. This step could still be automatically performed by utilizing face recognition to locate the resident of interest. As wrist joints were often occluded or hard to distinguish, we only retained wrist joint detections which had a prediction score larger than 0.5. Then we smoothed the wrist joint detections over time to create a trajectory of the wrist. Finally,

the distance between the wrist and the head was computed, and if the distance was less than a certain threshold, a "taking a bite" action had taken place.

We evaluated our performance with frame-based precision, recall and F1. A video frame was true positive if both the prediction and ground-truth indicate that there was an eating action in that frame. False positives and false negatives were computed accordingly. The statistics from different people were aggregated to compute the final micro-F1 score, which takes into account the number of positive instances per person. Computing the distance threshold for eating was difficult because the threshold was greatly affected by the size of the person in the video and the angle of how the camera viewed the person. Therefore, to circumvent this issue, we report the F1 score at the break-even point, which is the threshold where precision equals recall. In this way, our performance was not affected by the quality of the selected threshold.

Pose detectors which used different training data were tested. 5 pose detectors used 50, 200, 800, 1600, and 3193 manually labeled in-domain instances respectively for fine-tuning. These in-domain instances included samples of the same individual eating, so it is expected that the performance will be higher. Our constrained self-training (CST) based pose estimator was also used. Results are shown in Table 6.3. We can see an improvement of CST and other fine-tuned pose detectors over the detector trained only on LEEDS Sports 11K, thus showing that there is significant domain difference. However, performance of our CST-based pose detector was significantly lower than the detector which was fine-tuned over 50 manually labeled instances. This is different from our observation in Chapter 5. One main reason is that CST collected more full-body poses and had less eating related poses, thus leading to poor performance on eating poses.

On the other hand, the performance on resident 3 was significantly better for all detectors. Our observation was that performing pose estimation for eating activities from a slight profile view was easier than the frontal view. For the frontal case, the elbow was often occluded by the table and not visible, and this may make the pose estimation for the wrist joint less accurate. However, for the side view case, all joints were clearly visible, thus leading to significantly better pose estimation. Figure 6.5 shows snapshots of pose estimation for the 3 eating residents.

In sum, we show that we were able to detect a "taking a bite" activity with 26% F1 if we used our CST pose estimator. However, a detector fine-tuned with manually labeled samples still achieved around 50% F1. This shows that there is still a big domain difference between LEEDS Sports and Caremedia, and the pose estimator enhanced with CST could not fully overcome this difference. Nevertheless, the detector fine-tuned with manually labeled samples is already useful in automatically aggregating the eating

	Res. 1 F1	Res. 2 F1	Res. 3 F1	Micro-F1
LEEDS Sports 11K	0.234	0.106	0.292	0.218
CST, $c^f = 0.6$, $s^f = -350$	0.232	0.179	0.359	0.262
50 fine-tuning instances	0.219	0.171	0.683	0.369
200 fine-tuning instances	0.348	0.274	0.601	0.416
800 fine-tuning instances	0.383	0.288	0.733	0.478
1600 fine-tuning instances	0.395	0.327	0.744	0.497
3193 fine-tuning instances	0.386	0.327	0.710	0.480

TABLE 6.3: Performance of "taking a bite" activity detection based on pose estimation for resident 1, 2, 3. A joint micro-F1 score is also reported.

FIGURE 6.5: Snapshots of pose estimation for eating residents. Success and failure cases are both shown.

footage of a resident of interest over long periods of time. The footage can potentially aid doctors and staff in discovering subtle changes of the person's eating behavior, such as slower movement or shakier hands, thus providing more information in better diagnosing the nursing home resident.

6.3 Summary

In this chapter, we have demonstrated how our developed multi-object tracker and pose estimator could be utilized to analyze very large amounts of surveillance video and detect certain events of interest with reasonable accuracy. Visual diary summarization achieved a precision of 38% and recall of 52%. Individual-specific interaction timing analysis also showed trends which were in line with manual observations. Also, our "taking a bite" activity detector based on CST achieves 26% F1. Though our numbers are not high, compared to tedious manual analysis of thousands of hours of surveillance video, our

methods are a strong alternative, and it potentially opens the door to automatic analysis of the ocean of surveillance video recorded every day.

Chapter 7

Conclusions and Future Work

In this thesis, we proposed to utilize external knowledge and internal constraints in video to perform large-scale surveillance video analysis in an unsupervised fashion. We have presented improvements in identity-aware multi-object tracking and pose estimation. For multi-object tracking, we first demonstrated how to utilize external knowledge: face recognition combined with an internal constraint: spatial-temporal smoothness to localize and identify each person at each time instant. Then the same spatial-temporal smoothness constraint was further utilized to automatically collect large amounts of person re-identification training data, which was used to learn deep appearance features and further enhance tracking. For pose estimation, out-of-domain pose estimation training samples and spatial-temporal smoothness constraints were jointly utilized to perform constrained self-training for unsupervised domain adaptation. Results show that the in-domain training samples collected through constrained self-training significantly improved pose estimation performance, but the spatial-temporal smoothness constraints were not cost-effective in this scenario. Finally, our methods were applied to analyze 23 days of multi-camera surveillance footage. Tracking results show that our system was able to localize a person 57% of the time with 73% precision. Summarization results show that we were able to compute long-term statistics which were coherent with manual observations. Overall, these results demonstrate the effectiveness of our methods, which potentially opens the door to the automatic analysis of thousands or tens-of-thousands of hours of surveillance video.

7.1 The Do's and Don'ts of Surveillance Video Analysis

Based on the experience gained during the process of analyzing Caremedia nursing home videos, this section attempts to provide a guideline for future endeavors in analyzing

large-scale surveillance video.

Prevent unnecessary post-processing through careful setup of the recording environment. Setting up surveillance cameras "correctly" in a new environment before starting the recording is one of the most important factors in successful surveillance video analysis. By "correct", we mean the following.

1. Stationary cameras: Make sure the cameras are stationary and will not move due to shaking of walls or the building. If the camera moves, the camera calibration will need to be dynamically updated, which is very difficult, unnecessary and also time consuming to do.
2. Camera calibration: Make sure the intrinsic and extrinsic parameters of each camera are computed beforehand. Make sure not to adjust the focal length or viewing angle of the camera after calibration.
3. Camera synchronization: Make sure that all the cameras in the same scene are time synchronized. Synchronizing videos after they were recorded is very difficult and also leads to unnecessary work.
4. Deal with frame drops: It is inevitable for surveillance recordings to sometimes drop frames due to issues such as network connectivity. Therefore, the system should be designed such that it can automatically detect which frames have been dropped and ensure that the frames that are recorded after the frame drop are still time synchronized.
5. Record with as high resolution as possible: Higher resolution images can increase the recall of person detection and face recognition, which will highly affect tracking performance. Though processing and storage may be an issue, but acquiring more hardware for processing is often easier than improving tracking performance on low-resolution video.
6. Cameras with overlapping views are very helpful: As shown in Chapter 4, we have successfully learned deep appearance features based on person ReID training data which were collected by exploiting overlapping views between cameras. Without view overlaps, multi-view person ReID training data can no longer be acquired, which may lead to deep appearance features with less generalization ability.
7. Set up cameras such that they view the same scene from different angles: Not only should camera views overlap, it would be even more helpful if the cameras view the scene from different angles. This enables more accurate localization of objects and also provides more 3D information than a stereo camera. Also, if one would like to focus on very detailed behavior analysis such as eating analysis, a profile and frontal view of the person can potentially significantly improve pose detection performance.

8. Crowded corridors require more cameras: It may be tempting to only set up one or two cameras at the start/end of a very long corridor, because when the corridor is relatively empty, the cameras have a very clear view of the scene. However, there can easily be a lot of occlusions in corridors, thus it is still important to set up cameras along the corridor.
9. Do a dry run: Before the actual recording, it is crucial to run a dry run of the whole recording and analysis pipeline to confirm that the whole system, including the camera calibration, time synchronization and subsequent analysis is running as expected.

In sum, the spirit is to set up the surveillance camera environment such that one could collect as much accurate information as possible and avoid spending unnecessary time post-processing the recorded data. Also, the more cameras the better, and it is better to set up too many cameras and ignore the output of a few cameras than regret not setting up enough cameras. One may argue that hardware also costs money, but it may still be worthwhile when compared to spending extra human effort developing new algorithms which may still not perform as well as simply setting up more cameras. This actually also leads to an interesting research question: how many cameras is "enough" for a scene? How should they be placed?

Focus on very large data sets, and do not be disappointed by low performance. Given that the sheer volume of surveillance videos generated every day is impossible for humans to manually handle, the value of a surveillance video analysis system is that it can automatically analyze large amounts of video. Therefore, if we are to evaluate a system, we should focus on very large surveillance video data sets. Analyzing very large data sets not only ensures the scalability of the system but also enable the system to be tested in a more realistic environment. In surveillance video analysis, the events-of-interest rarely occur, and if only a few videos are used, then it may be highly likely that one will over-fit. A system is only valuable when it can locate rare events in a very large data set. However, this is a very difficult task, and in many cases performance will be low. Nevertheless, one should not be discouraged. Given that the other option for surveillance video analysis is manual analysis, an automatic system which can perform significantly better than random is already a very good first cut at analyzing the ocean of surveillance videos generated every day.

7.2 Future Work

Future work in terms of long-term nursing home analysis and also surveillance video analysis in general would be as follows:

1. Automatically training a robust detector for a specific object or person pose: In specific surveillance scenes, there will be different objects that one would like to detect and track. However, it is often the case that a robust detector is not available for those objects. Therefore, in order to be able to utilize tracking-by-detection, being able to automatically train an in-domain object detector would be crucial. In the nursing home case, it would be very useful if a general purpose sitting person detector and wheelchair detector could be trained, so that we are not only limited to tracking pedestrian-like people. One direction could be to utilize unsupervised co-localization [61] or object discovery [62] mentioned in Chapter 2. The high-level idea is that given the large amount of unlabeled videos, objects that are of interest for tracking should form a large enough cluster which could be automatically discovered. Another direction for automatically collecting training data of sitting people could be to jointly utilize face recognition, pose detection and a chair detector, which are all external resources we already have. With face recognition, we would know there is a person there. With pose estimation and a chair detector, we can predict whether the person is sitting. If we have multi-camera information, we could take this one step further and collect images/video of the same sitting person viewed from multiple angles.
2. Adapting pose detectors to deal with heavy occlusions: In indoor surveillance scenes, joints are easily occluded by static objects such as tables and chairs. Therefore, to perform robust pose estimation it is crucial that the pose estimator has the ability to deal with occlusions. Automatically collecting such training data is hard, and clever assumption/constraints are required. One potential assumption that could be utilized is: a person's face and their hands have similar color. Based on this assumption, one would have a very strong prior for the location of a wrist, which could potentially be useful for collecting pose estimation training data.
3. Activity detection in surveillance videos: Being able to detect arbitrary activities of interest is also a crucial step for analyzing surveillance videos. The classic way of training activity detectors is also based on supervised learning, which requires manual annotation of training data. Motivated by our work on automatically collecting action examples from instructional videos [104], one could potentially collect activity training data from a surveillance scene based on cues from the audio channel and automatic speech recognition. These cues provide us indirect information on the activities currently occurring in the scene.

The above enhancements, if successful, will enable us to acquire more information for each surveillance scene with less manual effort. In the nursing home case, we will be able to track significantly more elderly residents and harvest even more information from nursing home surveillance videos.

Taking a step back, the two information sources we used: external knowledge and internal constraints are not just useful in surveillance video analysis. In general, high-precision external knowledge sources can provide the initial labels for an otherwise completely unlabeled testing set, thus giving us a starting point to tackle the task. For example, in order to localize and identify each person in the scene, we leveraged face recognition to give us an initial set of labels, on which we performed constrained optimization. On the other hand, internal constraints have the ability to constrain an unlabeled data set such that useful information can still be found. The internal constraints can be very strict, but since the constraint can be operated on the near infinite amount of unlabeled video data available, we can still collect a significant amount of useful information. For example, the spatial-temporal smoothness constraint enabled us to collect person re-identification data for any calibrated multi-camera network scenario. The exploitation of the massive amount and variety of unlabeled videos available potentially enables a machine learning algorithm to learn more generalizable models than models trained on manually labeled data sets. Therefore, when facing a new task on a new (unlabeled) data set, one could first try to look for suitable external knowledge or available internal constraints to acquire useful information and alleviate manual annotation.

Taking a step further back, we believe an even higher-level principle which encompasses the formulation of the two information sources we have proposed is: how can one be smart with the labeled and unlabeled data we have? In the era of big data, data is our best friend, and the people who have the creativity and ability to harness the infinite power locked in big data will be the ones who have the potential to make a large impact on society.

Appendix A

Details of Iterative Projection Algorithm for Tracking with Solution Path Algorithm

In Section 3.7.2, we wanted to solve the following optimization problem:

$$\min_{\mathbf{G}} f(\mathbf{a}') = \left\|\mathbf{G} - \mathbf{a}'\right\|_2^2 \quad s.t. \quad \|\mathbf{G}\|_p \leq 1, \tag{A.1}$$

where $\mathbf{a}', \mathbf{G} \in \mathbf{R}^c$, $\mathbf{a}' = (a_1, a_2, \cdots, a_c)^T$ is the known reference point and $\mathbf{G}$ is the queried projection point on ℓ_p ball $\|\mathbf{G}\|_p \leq 1$.

The details of our iterative projection algorithm for solving (A.1) are as follows:

1: If $\|\mathbf{a}'\|_p \leq 1$, then output $\mathbf{G} = \mathbf{a}'$, and terminate the entire procedure. Otherwise, record $\mathbf{s} = sign(\mathbf{a}')$ and reformulate $\mathbf{a}' \leftarrow \mathbf{s} \odot \mathbf{a}'$ to make all its elements non-negative (i.e. to let $\mathbf{a}'$ be located in the first quadrant). Initialize $\mathbf{G}^{(1)} = (g_1^{(1)}, g_2^{(1)}, \cdots, g_c^{(1)})^T$ as the intersection of the line segment, which connects $\mathbf{a}'$ and the origin, with the boundary of the ℓ_p ball $\|\mathbf{G}\|_p = 1$. This intersection can be found efficiently with binary search. Let $l = 1$ and ε be a small threshold value.

2: **Repeat**:

3: Compute the tangent plane of the ℓ_p ball boundary curve $\|\mathbf{G}\|_p = 1$ at $\mathbf{G}^{(l)}$ as:

$$\pi^{(l)} = \{\mathbf{v} | \mathbf{w}^{(l)T}(\mathbf{v} - \mathbf{G}^{(l)}) = 0\},$$

where

$$\begin{aligned}\mathbf{w}^{(l)} &= \left(\nabla \|\mathbf{G}\|_p\right)_{\mathbf{G}^{(l)}} \\ &= (p(g_1^{(l)})^{p-1}, p(g_2^{(l)})^{p-1}, \cdots, p(g_c^{(l)})^{p-1})^T,\end{aligned}$$

where $g_i^{(l)}$ is the i^{th} element of $\mathbf{G}^{(l)}$. Calculate the projection point of $\mathbf{a}'$ on $\pi^{(l)}$ as

$$\mathbf{x}^{(l)} = \mathbf{a}' - \frac{\mathbf{w}^{(l)T}\mathbf{a}' - \mathbf{w}^{(l)T}\mathbf{G}^{(l)}}{\left\|\mathbf{w}^{(l)}\right\|_2^2}\mathbf{w}^{(l)}.$$

4. If $\mathbf{x}^{(l)}$ is located in the first quadrant (i.e., $\mathbf{x}^{(l)} \succeq 0$), then draw a line segment $\mathbf{z}(t)$ between $\mathbf{a}'$ and $\mathbf{x}^{(l)}$ as

$$\mathbf{z}(t) = (\mathbf{x}^{(l)} - \mathbf{a}')t + \mathbf{a}', 0 \leq t \leq 1,$$

and compute its intersection point $\mathbf{G}^{(l+1)}$ with the ℓ_p ball boundary curve $\|\mathbf{G}\|_p = 1$ using binary search. Then let $l = l + 1$, and go to the next iteration.

5. If $\mathbf{x}^{(l)}$ is located outside the first quadrant, then calculate

$$t^* = \min_i(t_i^*), t_i^* = \frac{a_i}{a_i - x_i},$$

where a_i and x_i are the i^{th} elements of $\mathbf{a}'$ and $\mathbf{x}^{(l)}$, respectively. If $\mathbf{z}(t^*) = (\mathbf{x}^{(l)} - \mathbf{a}')t^* + \mathbf{a}'$ satisfies that $\|\mathbf{z}(t^*)\|_p \leq 1$, then use the similar binary search strategy as step 4 to calculate the projection point $\mathbf{G}^{(l+1)}$. Then let $l = l + 1$, and go to the next iteration.

6. If $\|\mathbf{z}(t^*)\|_p > 1$, this means that the line segment $\mathbf{z}(t)$ $(0 \leq t \leq 1)$ does not intersect with the ℓ_p ball boundary curve $\|\mathbf{G}\|_p = 1$. Calculate the critical point $\mathbf{y}(s^*)$ where

$$\mathbf{y}(s) = (\mathbf{x}^{(l)} - \mathbf{G}^{(l)})s + \mathbf{G}^{(l)}, 0 \leq s \leq 1,$$

and

$$s^* = \min_i(s_i^*), s_i^* = \frac{g_i^{(l)}}{g_i^{(l)} - x_i}.$$

Then draw a line segment $\mathbf{z}(t)$ between $\mathbf{a}'$ and $\mathbf{y}(s^*)$ and compute its intersection point $\mathbf{G}^{(l+1)}$ with the ℓ_p ball boundary curve $\|\mathbf{G}\|_p = 1$ using binary search. Then let $l = l+1$, and go to the next iteration.

7. **End Repeat** when $\left\|\mathbf{G}^{(l)} - \mathbf{G}^{(l-1)}\right\| < \varepsilon$

8. Output the projection point $\mathbf{G} = \mathbf{s} \odot \mathbf{G}^{(l)}$.

A.1 Theoretical Principle

We use step-by-step remarks to explain the theoretical principle underlying our algorithm in detail.

A.1.1 Remarks for steps 1 and 8

Remark 1: When $\|\mathbf{a}'\|_p > 1$, it is easy to prove that its projection on the ℓ_p ball $\|\mathbf{G}\|_p \leq 1$ (the solution of (A.1)) is located on its boundary $\|\mathbf{G}\|_p = 1$. Furthermore, its projection lies in the same quadrant as $\mathbf{a}'$ [212].

Remark 2: Due to the symmetry property of the ℓ_2 objective and the ℓ_p constraint of (A.1), we can equivalently solve this optimization problem by getting the solution $\mathbf{G}$ for $f(|\mathbf{a}'|)$, where $|\mathbf{a}'| = \mathbf{s} \odot \mathbf{a}'$ and $\mathbf{s} = sign(\mathbf{a}')$ (step 1), and then transfer $\mathbf{G}$ (with all positive elements according to Remark 1) back to $\mathbf{G} = \mathbf{s} \odot \mathbf{G}$ (step 8). Here $\odot$ is the Hadamard product which is the element-wise multiplication between two vectors.

Remark 3: When $\|\mathbf{a}'\|_p > 1$, since $\|\mathbf{0}\|_p < 1$, the intersection of the line segment, which connects $\mathbf{a}'$ and the origin $\mathbf{0}$, with the unit ℓ_p ball boundary $\|\mathbf{G}\|_p = 1$ can definitely be found.

A.1.2 Remark for step 3

Remark 4: In the first quadrant, it is evident that the unit ℓ_p ball boundary curve $\|\mathbf{G}\|_p = 1$ is convex. This means that the tangent plane of this curve at $\mathbf{G}^{(l)}$ is below it. See Figure A.1 for a better understanding.

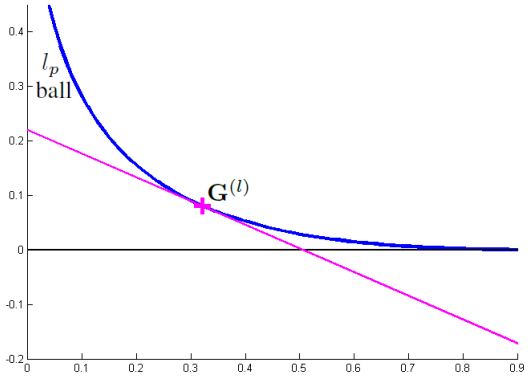

FIGURE A.1: Principle illustration for Remark 4.

A.1.3 Remark for step 4

Remark 5: Since $\|\mathbf{a}'\|_p > 1$ and $\left\|\mathbf{x}^{(l)}\right\|_p \leq 1$ (based on Remark 4), the intersection $\mathbf{G}^{(l+1)}$ of the line segment $\mathbf{z}(t)$ $(0 \leq t \leq 1)$ and $\|\mathbf{G}\|_p = 1$ definitely exists. Since $\mathbf{x}^{(l)}$ is the projection of $\mathbf{a}'$ on $\pi^{(l)}$ and $\mathbf{G}^{(l)}$ is located on $\pi^{(l)}$, we have $\left\|\mathbf{x}^{(l)}-\mathbf{a}'\right\|_2^2 \leq \left\|\mathbf{G}^{(l)}-\mathbf{a}'\right\|_2^2$. Besides, since $\mathbf{G}^{(l+1)}$ is obtained at $\mathbf{z}(t')$ for certain $0 \leq t' \leq 1$ and $\mathbf{x}^{(\mathbf{l})}$ and $\mathbf{a}'$ are the two end points of $\mathbf{z}(t)$, we have $\left\|\mathbf{G}^{(l+1)}-\mathbf{a}'\right\|_2^2 \leq \left\|\mathbf{x}^{(l)}-\mathbf{a}'\right\|_2^2$. It thus holds that $\left\|\mathbf{G}^{(l+1)}-\mathbf{a}'\right\|_2^2 \leq \left\|\mathbf{G}^{(l)}-\mathbf{a}'\right\|_2^2$. See Figure A.2 for a better understanding.

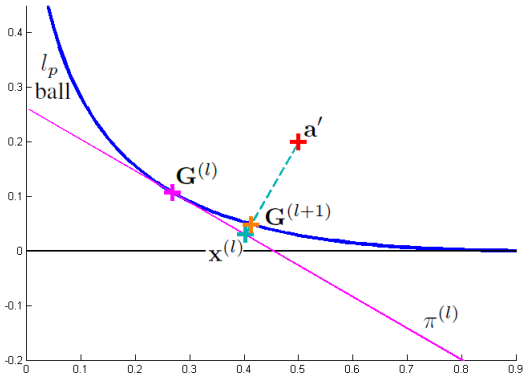

FIGURE A.2: Principle illustration for Remark 5.

A.1.4 Remark for steps 5 and 6:

Remark 6: Along the line segment $\mathbf{z}(t)$ $(0 \leq t \leq 1)$ connecting $\mathbf{a}'$ and $\mathbf{x}^{(l)}$, the critical point where the i^{th} element changes signs can be calculated by:

$$(x_i - a_i)t_i^* + a_i = 0 \implies t_i^* = \frac{a_i}{a_i - x_i}.$$

Then it is evident that the critical point of $\mathbf{z}(t)$ (location where it leaves the first quadrant) is at

$$t^* = \min_i(t_i^*).$$

We then have:

(i) When $\|\mathbf{z}(t^*)\|_p \leq 1$, since $\|\mathbf{a}'\|_p > 1$, the intersection of $\mathbf{z}(t)$ $(0 \leq t \leq 1)$ and $\|\mathbf{G}\|_p = 1$ exists in the first quadrant. Thus we can use binary search to find this intersection point. Based on the similar proof as Remark 5, we have $\left\|\mathbf{G}^{(l+1)}-\mathbf{a}'\right\|_2^2 \leq \left\|\mathbf{G}^{(l)}-\mathbf{a}'\right\|_2^2$.

(ii) When $\|\mathbf{z}(t^*)\|_p > 1$, we know that $\mathbf{z}(t^*)$ is not inside the ℓ_p ball $\Omega = \{\mathbf{G}|\, \|\mathbf{G}\|_p \leq 1\}$. Since $\overline{\Omega}$ in the first quadrant is convex (equivalent to that its boundary curve $\|\mathbf{G}\|_p = 1$ in the first quadrant is convex) and $\mathbf{a}' \in \overline{\Omega}$, it holds that the entire line segment $\mathbf{z}(t)$

$(0 \leq t \leq 1)$ is in $\overline{\Omega}$ and has no intersection with the curve $\|\mathbf{G}\|_p = 1$ in the first quadrant. We thus utilize the following strategy to find the next iteration point.

By connecting the last iteration point $\mathbf{G}^{(l)}$ and the projection point $\mathbf{x}^{(l)}$, we can formulate a line segment $\mathbf{y}(t)$ $(0 \leq t \leq 1)$. Using the similar strategy like (i), we can find the critical point $\mathbf{y}(s^*)$ at which $\mathbf{y}(t)$ goes out of the first quadrant, where

$$s^* = \min_i(s_i^*), s_i^* = \frac{g_i^{(l)}}{g_i^{(l)} - x_i},$$

where $g_i^{(l)}$ and x_i are the i^{th} element of $\mathbf{G}^{(l)}$ and $\mathbf{x}^{(l)}$, respectively. Since both $\mathbf{y}(s^*)$ and $\mathbf{G}^{(l)}$ are on the tangent plane $\pi^{(l)}$, and $\mathbf{y}(s^*)$ is closer to the projection point $\mathbf{x}^{(l)}$ of $\mathbf{a}'$ than $\mathbf{G}^{(l)}$, we have that $\|\mathbf{y}(s^*) - \mathbf{a}'\|_2^2 \leq \left\|\mathbf{G}^{(l)} - \mathbf{a}'\right\|_2^2$.

Since $\pi^{(l)}$ is below the curve $\|\mathbf{G}\|_p = 1$ based on Remark 4, we know that $\|\mathbf{y}(s^*)\|_p \leq 1$. Then together with $\|\mathbf{a}'\|_p > 1$, it holds that the intersection $\mathbf{G}^{(l+1)}$ of the line segment, which connects $\mathbf{a}'$ and $\mathbf{y}(s^*)$, with $\|\mathbf{G}\|_p = 1$ definitely exists in the first quadrant, and $\left\|\mathbf{G}^{(l+1)} - \mathbf{a}'\right\|_2^2 \leq \|\mathbf{y}(s^*) - \mathbf{a}'\|_2^2$. We thus have $\left\|\mathbf{G}^{(l+1)} - \mathbf{a}'\right\|_2^2 \leq \left\|\mathbf{G}^{(l)} - \mathbf{a}'\right\|_2^2$. The aforementioned procedure is illustrated in Figure A.3.

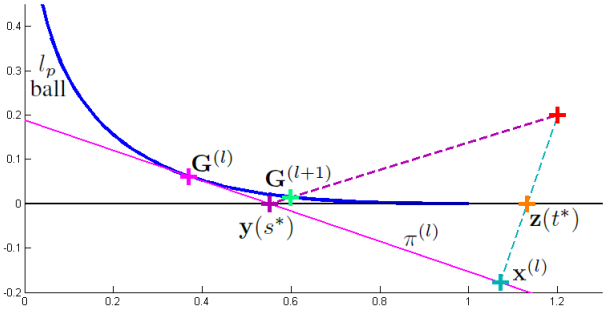

FIGURE A.3: Principle illustration for Remark 6(ii).

Based on the aforementioned Remarks 4, 5 and 6, we know that during the iterative process of our algorithm, the objective $\left\|\mathbf{G}^{(l)} - \mathbf{a}'\right\|_2^2$ is monotonically decreasing with respect to the iteration number l under the constraint $\left\|\mathbf{G}^{(l)}\right\|_p \leq 1$. Our algorithm is thus convergent and expected to arrive at a reasonable local minimum of the original problem.

Bibliography

[1] Shoou-I Yu, Lu Jiang, Zhongwen Xu, Yi Yang, and Alexander Hauptmann. Content-based video search over 1 million videos with 1 core in 1 second. In *ICMR*, 2015.

[2] Shoou-I Yu, Yi Yang, and Alexander Hauptmann. Harry potter's marauder's map: Localizing and tracking multiple persons-of-interest by nonnegative discretization. In *CVPR*, 2013.

[3] Yi Yang, Alexander Hauptmann, Ming-Yu Chen, Yang Cai, Ashok Bharucha, and Howard Wactlar. Learning to predict health status of geriatric patients from observational data. In *Computational Intelligence in Bioinformatics and Computational Biology*, 2012.

[4] Pedro F. Felzenszwalb, Ross B. Girshick, David A. McAllester, and Deva Ramanan. Object detection with discriminatively trained part-based models. *IEEE Transactions on Pattern Analysis and Machine Intelligence*, 2010.

[5] Alex Krizhevsky, Ilya Sutskever, and Geoffrey E Hinton. ImageNet classification with deep convolutional neural networks. In *NIPS*, 2012.

[6] Benjamin Sapp, David Weiss, and Ben Taskar. Parsing human motion with stretchable models. In *CVPR*, 2011.

[7] Shoou-I Yu, Lu Jiang, Zhongwen Xu, Zhenzhong Lan, et al. CMU-Informedia @ TRECVID. In *TRECVID Video Retrieval Evaluation Workshop*, 2014.

[8] Shih-En Wei, Varun Ramakrishna, Takeo Kanade, and Yaser Sheikh. Convolutional pose machines. In *CVPR*, 2016.

[9] Alon Halevy, Peter Norvig, and Fernando Pereira. The unreasonable effectiveness of data. *IEEE Intelligent Systems*, 2009.

[10] Vladimir Naumovich Vapnik and Vlamimir Vapnik. *Statistical learning theory*, volume 1. Wiley New York, 1998.

[11] Antonio Torralba and Alexei A Efros. Unbiased look at dataset bias. In *CVPR*, 2011.

[12] Jia Deng, Wei Dong, Richard Socher, Li-Jia Li, Kai Li, and Li Fei-Fei. ImageNet: A large-scale hierarchical image database. In *CVPR*, 2009.

[13] Jingen Liu, Jiebo Luo, and Mubarak Shah. Recognizing realistic actions from videos "in the wild". In *CVPR*, 2009.

[14] Paul Over, George Awad, Martial Michel, Jonathan Fiscus, Greg Sanders, Barbara Shaw, Wessel Kraaij, Alan F. Smeaton, and Georges Quenot. TRECVID 2012 – an overview of the goals, tasks, data, evaluation mechanisms and metrics. In *TRECVID*, 2012.

[15] Carl Vondrick, Donald Patterson, and Deva Ramanan. Efficiently scaling up crowdsourced video annotation. *International Journal of Computer Vision*, 2013.

[16] Olga Russakovsky, Li-Jia Li, and Li Fei-Fei. Best of both worlds: Human-machine collaboration for object annotation. In *CVPR*, 2015.

[17] Luis Von Ahn and Laura Dabbish. Labeling images with a computer game. In *Proceedings of the SIGCHI conference on Human factors in computing systems*, 2004.

[18] Jia Deng, Jonathan Krause, and Li Fei-Fei. Fine-grained crowdsourcing for fine-grained recognition. In *CVPR*, 2013.

[19] Meng Wang and Xiaogang Wang. Automatic adaptation of a generic pedestrian detector to a specific traffic scene. In *CVPR*, 2011.

[20] Meng Wang, Wei Li, and Xiaogang Wang. Transferring a generic pedestrian detector towards specific scenes. In *CVPR*, 2012.

[21] Carolina Galleguillos, Boris Babenko, Andrew Rabinovich, and Serge Belongie. Weakly supervised object localization with stable segmentations. In *ECCV*, 2008.

[22] Xiao Liu, Dacheng Tao, Mingli Song, Ying Ruan, Chun Chen, and Jiajun Bu. Weakly supervised multiclass video segmentation. In *CVPR*, 2014.

[23] Yu Zhang, Xiaowu Chen, Jia Li, Chen Wang, and Changqun Xia. Semantic object segmentation via detection in weakly labeled video. In *CVPR*, 2015.

[24] Andrew Carlson, Justin Betteridge, Bryan Kisiel, Burr Settles, Estevam R Hruschka Jr, and Tom M Mitchell. Toward an architecture for never-ending language learning. In *AAAI*, 2010.

[25] Richard C Wang and William W Cohen. Language-independent set expansion of named entities using the Web. In *Internation Conference on Data Mining*, 2007.

[26] Xinlei Chen, Abhinav Shrivastava, and Abhinav Gupta. Neil: Extracting visual knowledge from Web data. In *ICCV*, 2013.

[27] Santosh K Divvala, Ali Farhadi, and Carlos Guestrin. Learning everything about anything: Webly-supervised visual concept learning. In *CVPR*, 2014.

[28] Chao-Yeh Chen and Kristen Grauman. Watching unlabeled video helps learn new human actions from very few labeled snapshots. In *CVPR*, 2013.

[29] Kevin Tang, Vignesh Ramanathan, Li Fei-Fei, and Daphne Koller. Shifting weights: Adapting object detectors from image to video. In *NIPS*, 2012.

[30] Pramod Sharma, Chang Huang, and Ram Nevatia. Unsupervised incremental learning for improved object detection in a video. In *CVPR*, 2012.

[31] Xiaodan Liang, Si Liu, Yunchao Wei, Luoqi Liu, Liang Lin, and Shuicheng Yan. Towards computational baby learning: A weakly-supervised approach for object detection. In *ICCV*, 2015.

[32] Chuck Rosenberg, Martial Hebert, and Henry Schneiderman. Semi-supervised self-training of object detection models. In *Workshop on Application of Computer Vision*, 2005.

[33] Anna Margolis. A literature review of domain adaptation with unlabeled data. 2011.

[34] Shoou-I Yu, Deyu Meng, Wangmeng Zuo, and Alexander Hauptmann. The solution path algorithm for identity-aware multi-object tracking. In *CVPR*, 2016.

[35] Haoquan Shen, Shoou-I Yu, Yi Yang, Deyu Meng, and Alexander Hauptmann. Unsupervised video adaptation for parsing human motion. In *ECCV*, 2014.

[36] Jian Li, Timothy M Hospedales, Shaogang Gong, and Tao Xiang. Learning rare behaviours. In *ACCV*, 2010.

[37] Timothy M Hospedales, Jian Li, Shaogang Gong, and Tao Xiang. Identifying rare and subtle behaviors: A weakly supervised joint topic model. *IEEE Transactions on Pattern Analysis and Machine Intelligence*, 2011.

[38] Quannan Li, Jiajun Wu, and Zhuowen Tu. Harvesting mid-level visual concepts from large-scale Internet images. In *CVPR*, 2013.

[39] Le Wang, Gang Hua, Jianru Xue, Zhanning Gao, and Nanning Zheng. Joint segmentation and recognition of categorized objects from noisy Web image collection. *IEEE Transactions on Image Processing*, 2014.

[40] Parthipan Siva and Tao Xiang. Weakly supervised action detection. In *BMVC*, 2011.

[41] Alessandro Prest, Cordelia Schmid, and Vittorio Ferrari. Weakly supervised learning of interactions between humans and objects. *IEEE Transactions on Pattern Analysis and Machine Intelligence*, 2012.

[42] Kyaw Kyaw Htike and David Hogg. Weakly supervised pedestrian detector training by unsupervised prior learning and cue fusion in videos. In *International Conference on Image Processing*, 2014.

[43] Hakan Bilen, Marco Pedersoli, and Tinne Tuytelaars. Weakly supervised object detection with convex clustering. In *CVPR*, 2015.

[44] Enver Sangineto. Statistical and spatial consensus collection for detector adaptation. In *ECCV*, 2014.

[45] Adrien Gaidon, Gloria Zen, and Jose A Rodriguez-Serrano. Self-learning camera: Autonomous adaptation of object detectors to unlabeled video streams. *arXiv preprint arXiv:1406.4296*, 2014.

[46] Minh Hoai Nguyen, Lorenzo Torresani, Fernando de la Torre, and Carsten Rother. Weakly supervised discriminative localization and classification: A joint learning process. In *ICCV*, 2009.

[47] Chong Wang, Kaiqi Huang, Weiqiang Ren, Junge Zhang, and Steve Maybank. Large-scale weakly supervised object localization via latent category learning. *IEEE Transactions on Image Processing*, 2015.

[48] Maxime Oquab, Léon Bottou, Ivan Laptev, and Josef Sivic. Is object localization for free? Weakly-supervised learning with convolutional neural networks. In *CVPR*, 2015.

[49] Thomas Deselaers, Bogdan Alexe, and Vittorio Ferrari. Weakly supervised localization and learning with generic knowledge. *International Journal of Computer Vision*, 2012.

[50] Alexander Vezhnevets and Joachim M Buhmann. Towards weakly supervised semantic segmentation by means of multiple instance and multitask learning. In *CVPR*, 2010.

[51] Deepak Pathak, Evan Shelhamer, Jonathan Long, and Trevor Darrell. Fully convolutional multi-class multiple instance learning. *arXiv preprint arXiv:1412.7144*, 2014.

[52] Jifeng Dai, Kaiming He, and Jian Sun. Boxsup: Exploiting bounding boxes to supervise convolutional networks for semantic segmentation. In *ICCV*, 2015.

[53] Deepak Pathak, Philipp Krahenbuhl, and Trevor Darrell. Constrained convolutional neural networks for weakly supervised segmentation. In *ICCV*, 2015.

[54] George Papandreou, Liang-Chieh Chen, Kevin Murphy, and Alan L. Yuille. Weakly- and semi-supervised learning of a DCNN for semantic image segmentation. In *ICCV*, 2015.

[55] Seunghoon Hong, Hyeonwoo Noh, and Bohyung Han. Decoupled deep neural network for semi-supervised semantic segmentation. In *NIPS*, 2015.

[56] Vicky Kalogeiton, Vittorio Ferrari, and Cordelia Schmid. Analysing domain shift factors between videos and images for object detection. *arXiv preprint arXiv:1501.01186*, 2015.

[57] Alessandro Prest, Christian Leistner, Javier Civera, Cordelia Schmid, and Vittorio Ferrari. Learning object class detectors from weakly annotated video. In *CVPR*, 2012.

[58] Le Wang, Gang Hua, Rahul Sukthankar, Jianru Xue, and Nanning Zheng. Video object discovery and co-segmentation with extremely weak supervision. In *ECCV*, 2014.

[59] P. Tokmakov, K. Alahari, and C. Schmid. Weakly-Supervised Semantic Segmentation using Motion Cues. *arXiv:1603.07188*, 2016.

[60] Ke Tang, Armand Joulin, Li-Jia Li, and Li Fei-Fei. Co-localization in real-world images. In *CVPR*, 2014.

[61] Armand Joulin, Kevin Tang, and Li Fei-Fei. Efficient image and video co-localization with Frank-Wolfe algorithm. In *ECCV*, 2014.

[62] Suha Kwak, Minsu Cho, Ivan Laptev, Jean Ponce, and Cordelia Schmid. Unsupervised object discovery and tracking in video collections. In *ICCV*, 2015.

[63] Li-Jia Li and Li Fei-Fei. OPTIMOL: Automatic online picture collection via incremental model learning. *International Journal of Computer Vision*, 2010.

[64] Bolei Zhou, Vignesh Jagadeesh, and Robinson Piramuthu. Conceptlearner: Discovering visual concepts from weakly labeled image collections. In *CVPR*, 2015.

[65] Marcos Rubinstein, Armand Joulin, Johannes Kopf, and Ce Liu. Unsupervised joint object discovery and segmentation in Internet images. In *CVPR*, 2013.

[66] Xinlei Chen, Abhinav Shrivastava, and Abhinav Gupta. Enriching visual knowledge bases via object discovery and segmentation. In *CVPR*, 2014.

[67] Xinlei Chen and Abhinav Gupta. Webly supervised learning of convolutional networks. In *ICCV*, 2015.

[68] Lixin Duan, Dong Xu, Ivor Wai-Hung Tsang, and Jiebo Luo. Visual event recognition in videos by learning from Web data. *IEEE Transactions on Pattern Analysis and Machine Intelligence*, 2012.

[69] Andrej Karpathy, George Toderici, Sanketh Shetty, Thomas Leung, Rahul Sukthankar, and Li Fei-Fei. Large-scale video classification with convolutional neural networks. In *CVPR*, 2014.

[70] Lu Jiang, Shoou-I Yu, Deyu Meng, Teruko Mitamura, and Alexander G Hauptmann. Bridging the ultimate semantic gap: A semantic search engine for Internet videos. In *ICMR*, 2015.

[71] Bart Thomee, David A Shamma, Gerald Friedland, Benjamin Elizalde, Karl Ni, Douglas Poland, Damian Borth, and Li-Jia Li. The new data and new challenges in multimedia research. *arXiv preprint arXiv:1503.01817*, 2015.

[72] Kyaw Kyaw Htike and David Hogg. Adapting pedestrian detectors to new domains: A comprehensive review. *Engineering Applications of Artificial Intelligence*, 2016.

[73] Vishal M Patel, Raghuraman Gopalan, Ruonan Li, and Rama Chellappa. Visual domain adaptation: A survey of recent advances. *IEEE Signal Processing Magazine*, 2015.

[74] Hidetoshi Shimodaira. Improving predictive inference under covariate shift by weighting the log-likelihood function. *Journal of statistical planning and inference*, 2000.

[75] Raghuraman Gopalan, Ruonan Li, and Rama Chellappa. Domain adaptation for object recognition: An unsupervised approach. In *ICCV*, 2011.

[76] Boqing Gong, Yuan Shi, Fei Sha, and Kristen Grauman. Geodesic flow kernel for unsupervised domain adaptation. In *CVPR*, 2012.

[77] Boqing Gong, Kristen Grauman, and Fei Sha. Reshaping visual datasets for domain adaptation. In *NIPS*, 2013.

[78] Fatemeh Mirrashed and Mohammad Rastegari. Domain adaptive classification. In *ICCV*, 2013.

[79] Yaroslav Ganin and Victor Lempitsky. Unsupervised domain adaptation by backpropagation. In *ICML*, 2015.

[80] Meina Kan, Shiguang Shan, and Xilin Chen. Bi-shifting auto-encoder for unsupervised domain adaptation. In *ICCV*, 2015.

[81] Fabio Roli and Gian Luca Marcialis. Semi-supervised PCA-based face recognition using self-training. *Structural, Syntactic, and Statistical Pattern Recognition*, 2006.

[82] Alex Teichman and Sebastian Thrun. Tracking-based semi-supervised learning. *The International Journal of Robotics Research*, 2012.

[83] Omar Javed, Saad Ali, and Mubarak Shah. Online detection and classification of moving objects using progressively improving detectors. In *CVPR*, 2005.

[84] Robert E Schapire and Yoram Singer. Improved boosting algorithms using confidence-rated predictions. *Machine learning*, 1999.

[85] Avrim Blum and Tom Mitchell. Combining labeled and unlabeled data with co-training. In *Proceedings of the eleventh annual conference on computational learning theory*, 1998.

[86] Bo Wu and Ram Nevatia. Improving part based object detection by unsupervised, online boosting. In *CVPR*, 2007.

[87] Aniruddha Kembhavi, Behjat Siddiquie, Roland Miezianko, Scott McCloskey, and Larry S Davis. Incremental multiple kernel learning for object recognition. In *ICCV*, 2009.

[88] Xiaoyu Wang, Gang Hua, and Tony X Han. Detection by detections: Non-parametric detector adaptation for a video. In *CVPR*, 2012.

[89] Guang Shu, Afshin Dehghan, and Mubarak Shah. Improving an object detector and extracting regions using superpixels. In *CVPR*, 2013.

[90] Khaleda Ali, David Hasler, and Francois Fleuret. Flowboost: Appearance learning from sparsely annotated video. In *CVPR*, 2011.

[91] Pramod Sharma and Ram Nevatia. Efficient detector adaptation for object detection in a video. In *CVPR*, 2013.

[92] Kyaw Kyaw Htike and David C Hogg. Efficient non-iterative domain adaptation of pedestrian detectors to video scenes. In *International Conference on Pattern Recognition*, 2014.

[93] Jeff Donahue, Judy Hoffman, Erik Rodner, Kate Saenko, and Trevor Darrell. Semi-supervised domain adaptation with instance constraints. In *CVPR*, 2013.

[94] Alina Kuznetsova, Sung Ju Hwang, Bodo Rosenhahn, and Leonid Sigal. Expanding object detector's horizon: Incremental learning framework for object detection in videos. In *CVPR*, 2015.

[95] Rajat Raina, Alexis Battle, Honglak Lee, Benjamin Packer, and Andrew Y Ng. Self-taught learning: Transfer learning from unlabeled data. In *ICML*, 2007.

[96] Saurabh Singh, Abhinav Gupta, and Alexei A. Efros. Unsupervised discovery of mid-level discriminative patches. In *ECCV*, 2012.

[97] Naiyan Wang and Dit-Yan Yeung. Learning a deep compact image representation for visual tracking. In *NIPS*, 2013.

[98] Xiaolong Wang and Abhinav Gupta. Unsupervised learning of visual representations using videos. In *ICCV*, 2015.

[99] Carl Doersch, Abhinav Gupta, and Alexei A. Efros. Unsupervised visual representation learning by context prediction. In *ICCV*, 2015.

[100] Ishan Misra, C. Lawrence Zitnick, and Hebert Martial. Unsupervised learning using sequential verification for action recognition. *arXiv preprint arXiv:1603.08561*, 2016.

[101] Vinod Nair and James J Clark. An unsupervised, online learning framework for moving object detection. In *CVPR*, 2004.

[102] Ehsan Adeli Mosabbeb, Ricardo Cabral, Fernando De la Torre, and Mahmood Fathy. Multi-label discriminative weakly-supervised human activity recognition and localization. In *ACCV*, 2014.

[103] Piotr Bojanowski, Rémi Lajugie, Francis Bach, Ivan Laptev, Jean Ponce, Cordelia Schmid, and Josef Sivic. Weakly supervised action labeling in videos under ordering constraints. In *ECCV*, 2014.

[104] Shoou-I Yu, Lu Jiang, and Alexander Hauptmann. Instructional videos for unsupervised harvesting and learning of action examples. In *ACM Multimedia*, 2014.

[105] Jonathan Malmaud, Jonathan Huang, Vivek Rathod, Nick Johnston, Andrew Rabinovich, and Kevin Murphy. What's cookin'? interpreting cooking videos using text, speech and vision. In *North American Chapter of the Association for Computational Linguistics: Human Language Technologies*, 2015.

[106] Ozan Sener, Amir R Zamir, Silvio Savarese, and Ashutosh Saxena. Unsupervised semantic parsing of video collections. In *ICCV*, 2015.

[107] Sudeep Sarkar, P Jonathon Phillips, Zongyi Liu, Isidro Robledo Vega, Patrick Grother, and Kevin W Bowyer. The HumanID gait challenge problem: Data sets, performance, and analysis. *IEEE Transactions on Pattern Analysis and Machine Intelligence*, 2005.

[108] Chikahito Nakajima, Massimiliano Pontil, Bernd Heisele, and Tomaso Poggio. Full-body person recognition system. *Pattern recognition*, 2003.

[109] Kenji Okuma, Ali Taleghani, Nando De Freitas, O De Freitas, James J. Little, and David G. Lowe. A boosted particle filter: Multitarget detection and tracking. In *ECCV*, 2004.

[110] J. K. Rowling. *Harry Potter and the Prisoner of Azkaban*. London: Bloomsbury, 1999.

[111] F. Fleuret, J. Berclaz, R. Lengagne, and P. Fua. Multicamera people tracking with a probabilistic occupancy map. *IEEE Transactions on Pattern Analysis and Machine Intelligence*, 2008.

[112] J. Berclaz, F. Fleuret, E. Turetken, and P. Fua. Multiple object tracking using k-shortest paths optimization. *IEEE Transactions on Pattern Analysis and Machine Intelligence*, 2011.

[113] Horesh Ben Shitrit, Jerome Berclaz, Francois Fleuret, and Pascal Fua. Multi-commodity network flow for tracking multiple people. *IEEE Transactions on Pattern Analysis and Machine Intelligence*, 2014.

[114] Xinchao Wang, Engin Türetken, Fran**c**cois Fleuret, and Pascal Fua. Tracking interacting objects optimally using integer programming. In *ECCV*, 2014.

[115] Amir Roshan Zamir, Afshin Dehghan, and Mubarak Shah. GMCP-Tracker: Global multi-object tracking using generalized minimum clique graphs. In *ECCV*, 2012.

[116] Hamed Pirsiavash, Deva Ramanan, and Charless C Fowlkes. Globally-optimal greedy algorithms for tracking a variable number of objects. In *CVPR*, 2011.

[117] Li Zhang, Yuan Li, and Ramakant Nevatia. Global data association for multi-object tracking using network flows. In *CVPR*, 2008.

[118] Anton Andriyenko and Konrad Schindler. Multi-target tracking by continuous energy minimization. In *CVPR*, 2011.

[119] Anton Andriyenko, Konrad Schindler, and Stefan Roth. Discrete-continuous optimization for multi-target tracking. In *CVPR*, 2012.

[120] Anton Milan, Konrad Schindler, and Stefan Roth. Detection-and trajectory-level exclusion in multiple object tracking. In *CVPR*, 2013.

[121] Robert T Collins. Multitarget data association with higher-order motion models. In *CVPR*, 2012.

[122] A Butt and R Collins. Multi-target tracking by Lagrangian relaxation to min-cost network flow. In *CVPR*, 2013.

[123] Chang Huang, Bo Wu, and Ramakant Nevatia. Robust object tracking by hierarchical association of detection responses. In *ECCV*, 2008.

[124] Cheng-Hao Kuo, Chang Huang, and Ram Nevatia. Multi-target tracking by on-line learned discriminative appearance models. In *CVPR*, 2010.

[125] Cheng-Hao Kuo and Ram Nevatia. How does person identity recognition help multi-person tracking? In *CVPR*, 2011.

[126] Bo Yang and Ram Nevatia. An online learned CRF model for multi-target tracking. In *CVPR*, 2012.

[127] Yuan Li, Chang Huang, and Ram Nevatia. Learning to associate: Hybridboosted multi-target tracker for crowded scene. In *CVPR*, 2009.

[128] Bo Yang and Ram Nevatia. Multi-target tracking by online learning of non-linear motion patterns and robust appearance models. In *CVPR*, 2012.

[129] Hao Jiang, Sidney Fels, and James J. Little. A linear programming approach for multiple object tracking. In *CVPR*, 2007.

[130] Bastian Leibe, Konrad Schindler, and Luc Van Gool. Coupled detection and trajectory estimation for multi-object tracking. In *CVPR*, 2007.

[131] Anton Andriyenko and Konrad Schindler. Globally optimal multi-target tracking on a hexagonal lattice. In *ECCV*, 2010.

[132] Navneet Dalal and Bill Triggs. Histograms of oriented gradients for human detection. In *CVPR*, 2005.

[133] Seung-Hwan Bae and Kuk-Jin Yoon. Robust online multi-object tracking based on tracklet confidence and online discriminative appearance learning. In *CVPR*, 2014.

[134] Bing Wang, Gang Wang, Kap Luk Chan, and Li Wang. Tracklet association with online target-specific metric learning. In *CVPR*, 2014.

[135] Xiaoqin Zhang, Weiming Hu, Steve Maybank, and Xi Li. Graph based discriminative learning for robust and efficient object tracking. In *CVPR*, 2007.

[136] Weiming Hu, Xi Li, Wenhan Luo, Xiaoqin Zhang, Stephen Maybank, and Zhongfei Zhang. Single and multiple object tracking using log-Euclidean Riemannian subspace and block-division appearance model. *IEEE Transactions on Pattern Analysis and Machine Intelligence*, 2012.

[137] Zia Khan, Tucker Balch, and Frank Dellaert. MCMC-based particle filtering for tracking a variable number of interacting targets. *IEEE Transactions on Pattern Analysis and Machine Intelligence*, 2005.

[138] Rob Hess and Alan Fern. Discriminatively trained particle filters for complex multi-object tracking. In *CVPR*, 2009.

[139] C. Dicle, M. Sznaier, and O. Camps. The way they move: Tracking targets with similar appearance. In *ICCV*, 2013.

[140] Asad A Butt and Robert T Collins. Multiple target tracking using frame triplets. In *ACCV*, 2013.

[141] Victorio Ferrari, Tinne Tuytelaars, and Luc Van Gool. Real-time affine region tracking and coplanar grouping. In *CVPR*, 2001.

[142] Manuel Jesús Marín-Jiménez, Andrew Zisserman, Marcin Eichner, and Vittorio Ferrari. Detecting people looking at each other in videos. *International Journal of Computer Vision*, 2014.

[143] Steven Gold, Anand Rangarajan, et al. Softmax to softassign: Neural network algorithms for combinatorial optimization. *Journal of Artificial Neural Networks*, 1996.

[144] Visesh Chari, Simon Lacoste-Julien, Ivan Laptev, and Josef Sivic. On pairwise costs for network flow multi-object tracking. In *CVPR*, 2015.

[145] M. Zervos, H. BenShitrit, F. Fleuret, and P. Fua. Facial descriptors for identity-preserving multiple people tracking. Technical report EPFL-ARTICLE-187534, EPFL, 2013.

[146] Afshin Dehghan, Yicong Tian, Philip HS Torr, and Mubarak Shah. Target identity-aware network flow for online multiple target tracking. In *CVPR*, 2015.

[147] Mark Everingham, Josef Sivic, and Andrew Zisserman. Taking the bite out of automated naming of characters in TV video. *Image and Vision Computing*, 2009.

[148] Josef Sivic, Mark Everingham, and Andrew Zisserman. "Who are you?" - Learning person specific classifiers from video. In *CVPR*, 2009.

[149] Andrew Y Ng, Michael I Jordan, Yair Weiss, et al. On spectral clustering: Analysis and an algorithm. In *NIPS*, 2002.

[150] Chaochao Lu and Xiaoou Tang. Surpassing human-level face verification performance on LFW with GaussianFace. *arXiv preprint arXiv:1404.3840*, 2014.

[151] Yi Yang, Heng Tao Shen, Feiping Nie, Rongrong Ji, and Xiaofang Zhou. Nonnegative spectral clustering with discriminative regularization. In *AAAI*, 2011.

[152] Zhirong Yang and Erkki Oja. Linear and nonlinear projective nonnegative matrix factorization. *IEEE Neural Networks*, 2010.

[153] Chris Ding, Tao Li, and Michael I Jordan. Nonnegative matrix factorization for combinatorial optimization: Spectral clustering, graph matching, and clique finding. In *Internation Conference on Data Mining*, 2008.

[154] Jiho Yoo and Seungjin Choi. Nonnegative matrix factorization with orthogonality constraints. *Journal of computing science and engineering*, 2010.

[155] Filippo Pompili, Nicolas Gillis, P-A Absil, and Francois Glineur. Two algorithms for orthogonal nonnegative matrix factorization with application to clustering. *Neurocomputing*, 2014.

[156] Stephen J Wright and Jorge Nocedal. *Numerical optimization*, volume 2. Springer New York, 1999.

[157] Chih-Jen Lin. Projected gradient methods for nonnegative matrix factorization. *Neural computation*, 2007.

[158] Daniel D. Lee and H. Sebastian Seung. Algorithms for non-negative matrix factorization. In *NIPS*, 2000.

[159] Yi Yang, Feiping Nie, Dong Xu, Jiebo Luo, Yueting Zhuang, and Yunhe Pan. A multimedia retrieval framework based on semi-supervised ranking and relevance feedback. *IEEE Transactions on Pattern Analysis and Machine Intelligence*, 2012.

[160] Bradley Efron, Trevor Hastie, Iain Johnstone, Robert Tibshirani, et al. Least angle regression. *The Annals of statistics*, 2004.

[161] Ryan Joseph Tibshirani. *The solution path of the generalized lasso.* Stanford University, 2011.

[162] Stephen Boyd and Lieven Vandenberghe. *Convex optimization.* Cambridge university press, 2009.

[163] Burr Settles. Active learning literature survey. Computer Sciences Technical Report 1648, University of Wisconsin–Madison, 2009.

[164] A. Ellis, A. Shahrokni, and J.M. Ferryman. PETS 2009 and winter-PETS 2009 results: A combined evaluation. In *Performance Evaluation of Tracking and Surveillance (PETS-Winter)*, 2009.

[165] Sangmin Oh, Anthony Hoogs, Amitha Perera, Naresh Cuntoor, Chia-Chih Chen, Jong Taek Lee, Saurajit Mukherjee, JK Aggarwal, Hyungtae Lee, Larry Davis, et al. A large-scale benchmark dataset for event recognition in surveillance video. In *CVPR*, 2011.

[166] National institute of standards and technology: TRECVID 2012 evaluation for surveillance event detection. http://www.nist.gov/speech/tests/trecvid/2012/. 2012.

[167] Ben Benfold and Ian Reid. Stable multi-target tracking in real-time surveillance video. In *CVPR*, 2011.

[168] Shoou-I Yu, Yi Yang, Xuanchong Li, and Alexander Hauptmann. Long-term identity-aware multi-person tracking for surveillance video summarization. *arXiv:1604.07468*, 2016.

[169] Gurobi. Gurobi optimizer reference manual, 2012.

[170] Mikhail Belkin and Partha Niyogi. Laplacian eigenmaps for dimensionality reduction and data representation. *Neural computation*, 2003.

[171] R. B. Girshick, P. F. Felzenszwalb, and D. McAllester. Discriminatively trained deformable part models, release 5. http://people.cs.uchicago.edu/ rbg/latent-release5/.

[172] Patrick Pérez, Carine Hue, Jaco Vermaak, and Michel Gangnet. Color-based probabilistic tracking. In *ECCV*, 2002.

[173] S. Lazebnik, C. Schmid, and J. Ponce. Beyond bags of features: Spatial pyramid matching for recognizing natural scene categories. In *CVPR*, 2006.

[174] Chris Stauffer and W Eric L Grimson. Adaptive background mixture models for real-time tracking. In *CVPR*, 1999.

[175] Keni Bernardin and Rainer Stiefelhagen. Evaluating multiple object tracking performance: The CLEAR MOT metrics. *Journal on Image and Video Processing*, 2008.

[176] Rangachar Kasturi, Dmitry Goldgof, Padmanabhan Soundararajan, Vasant Manohar, John Garofolo, Rachel Bowers, Matthew Boonstra, Valentina Korzhova, and Jing Zhang. Framework for performance evaluation of face, text, and vehicle detection and tracking in video: Data, metrics, and protocol. *IEEE Transactions on Pattern Analysis and Machine Intelligence*, 2009.

[177] Seung-Hwan Bae Bae and Kuk-Jin Yoon. Robust online multi-object tracking based on tracklet confidence and online discriminative appearance learning. In *CVPR*, 2014.

[178] Horesh Ben Shitrit, Jérôme Berclaz, Fran**c**cois Fleuret, and Pascal Fua. Multi-commodity network flow for tracking multiple people. *IEEE Transactions on Pattern Analysis and Machine Intelligence*, 2013.

[179] Claude Shannon. A mathematical theory of communication. *Bell Systems Technical Journal*, 1948.

[180] Carl Vondrick and Deva Ramanan. Video annotation and tracking with active learning. In *NIPS*, 2011.

[181] Arridhana Ciptadi and James M Rehg. Minimizing human effort in interactive tracking by incremental learning of model parameters. In *ICCV*, 2015.

[182] Alexander Toshev and Christian Szegedy. Deeppose: Human pose estimation via deep neural networks. In *CVPR*, 2014.

[183] Dong Yi, Zhen Lei, Shengcai Liao, and Stan Z Li. Deep metric learning for person re-identification. In *ICPR*, 2014.

[184] Wei Li, Rui Zhao, Tong Xiao, and Xiaogang Wang. Deepreid: Deep filter pairing neural network for person re-identification. In *CVPR*, 2014.

[185] Ejaz Ahmed, Michael Jones, and Tim K Marks. An improved deep learning architecture for person re-identification. In *CVPR*, 2015.

[186] Raia Hadsell, Sumit Chopra, and Yann LeCun. Dimensionality reduction by learning an invariant mapping. In *CVPR*, 2006.

[187] Yangqing Jia, Evan Shelhamer, Jeff Donahue, Sergey Karayev, Jonathan Long, Ross Girshick, Sergio Guadarrama, and Trevor Darrell. Caffe: Convolutional architecture for fast feature embedding. *arXiv preprint arXiv:1408.5093*, 2014.

[188] Chang Huang, Bo Wu, and Ramakant Nevatia. Robust object tracking by hierarchical association of detection responses. In *ECCV*, 2008.

[189] Shaoqing Ren, Kaiming He, Ross Girshick, and Jian Sun. Faster R-CNN: Towards real-time object detection with region proposal networks. In *NIPS*, 2015.

[190] Yi Yang and Deva Ramanan. Articulated pose estimation with flexible mixtures-of-parts. In *CVPR*, 2011.

[191] Benjamin Sapp and Ben Taskar. MODEC: Multimodal decomposable models for human pose estimation. In *CVPR*, 2013.

[192] Varun Ramakrishna, Daniel Munoz, Martial Hebert, James Andrew Bagnell, and Yaser Sheikh. Pose machines: Articulated pose estimation via inference machines. In *ECCV*, 2014.

[193] Vittorio Ferrari, Manuel Marín-Jiménez, and Andrew Zisserman. 2D human pose estimation in TV shows. *Statistical and Geometrical Approaches to Visual Motion Analysis*, 2009.

[194] Katerina Fragkiadaki, Han Hu, and Jianbo Shi. Pose from flow and flow from pose. In *CVPR*, 2013.

[195] Anoop Cherian, Julien Mairal, Karteek Alahari, and Cordelia Schmid. Mixing body-part sequences for human pose estimation. In *CVPR*, 2014.

[196] Deva Ramanan, David A Forsyth, and Andrew Zisserman. Strike a pose: Tracking people by finding stylized poses. In *CVPR*, 2005.

[197] Leonid Sigal and Michael J Black. Measure locally, reason globally: Occlusion-sensitive articulated pose estimation. In *CVPR*, 2006.

[198] Yang Wang and Greg Mori. Multiple tree models for occlusion and spatial constraints in human pose estimation. In *ECCV*, 2008.

[199] Joao Carreira, Pulkit Agrawal, Katerina Fragkiadaki, and Jitendra Malik. Human pose estimation with iterative error feedback. *arXiv preprint arXiv:1507.06550*, 2015.

[200] Jonathan J Tompson, Arjun Jain, Yann LeCun, and Christoph Bregler. Joint training of a convolutional network and a graphical model for human pose estimation. In *NIPS*, 2014.

[201] Deva Ramanan. Learning to parse images of articulated bodies. In *NIPS*, 2006.

[202] Marcin Eichner, Manuel Marin-Jimenez, Andrew Zisserman, and Vittorio Ferrari. 2D articulated human pose estimation and retrieval in (almost) unconstrained still images. *International Journal of Computer Vision*, 2012.

[203] Sam Johnson and Mark Everingham. Learning effective human pose estimation from inaccurate annotation. In *CVPR*, 2011.

[204] Mykhaylo Andriluka, Leonid Pishchulin, Peter Gehler, and Bernt Schiele. 2D human pose estimation: New benchmark and state of the art analysis. In *CVPR*, 2014.

[205] Heng Wang, Alexander Klaser, Cordelia Schmid, and Cheng-Lin Liu. Action recognition by dense trajectories. In *CVPR*, 2011.

[206] Bruce D Lucas, Takeo Kanade, et al. An iterative image registration technique with an application to stereo vision. In *IJCAI*, 1981.

[207] Sam Johnson and Mark Everingham. Clustered pose and nonlinear appearance models for human pose estimation. In *BMVC*, 2010.

[208] Nuria M Oliver, Barbara Rosario, and Alex P Pentland. A Bayesian computer vision system for modeling human interactions. *IEEE Transactions on Pattern Analysis and Machine Intelligence*, 2000.

[209] Clark McPhail and Ronald T Wohlstein. Using film to analyze pedestrian behavior. *Sociological Methods & Research*, 1982.

[210] Heng Wang, Cordelia Schmid, et al. Action recognition with improved trajectories. In *ICCV*, 2013.

[211] K. Chatfield, V. Lempitsky, A. Vedaldi, and A. Zisserman. The devil is in the details: an evaluation of recent feature encoding methods. In *BMVC*, 2011.

[212] S. Bahmani and B. Raj. A unifying analysis of projected gradient descent for lp-constrained least squares. *ArXiv:1107.4623v5*, 2012.